

DISSERTATION

PROPAGATION AND FREQUENCY CONVERSION OF
ULTRASHORT PULSES IN THE PRESENCE OF
COHERENT NUCLEAR MOTION

Submitted by

Klaus Karl Hartinger

Electrical and Computer Engineering

In partial fulfillment of the requirements

For the Degree of Doctor of Philosophy

Colorado State University

Fort Collins, Colorado

Fall 2008

UMI Number: 3346458

INFORMATION TO USERS

The quality of this reproduction is dependent upon the quality of the copy submitted. Broken or indistinct print, colored or poor quality illustrations and photographs, print bleed-through, substandard margins, and improper alignment can adversely affect reproduction.

In the unlikely event that the author did not send a complete manuscript and there are missing pages, these will be noted. Also, if unauthorized copyright material had to be removed, a note will indicate the deletion.

UMI[®]

UMI Microform 3346458

Copyright 2009 by ProQuest LLC.

All rights reserved. This microform edition is protected against unauthorized copying under Title 17, United States Code.

ProQuest LLC
789 E. Eisenhower Parkway
PO Box 1346
Ann Arbor, MI 48106-1346

COLORADO STATE UNIVERSITY

October 30, 2008

WE HEREBY RECOMMEND THAT THE DISSERTATION PREPARED UNDER OUR SUPERVISION BY KLAUS KARL HARTINGER ENTITLED PROPAGATION AND FREQUENCY CONVERSION OF ULTRASHORT PULSES IN THE PRESENCE OF COHERENT NUCLEAR MOTION BE ACCEPTED AS FULFILLING IN PART REQUIREMENTS FOR THE DEGREE OF DOCTOR OF PHILOSOPHY.

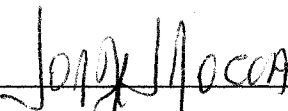
Committee on Graduate Work



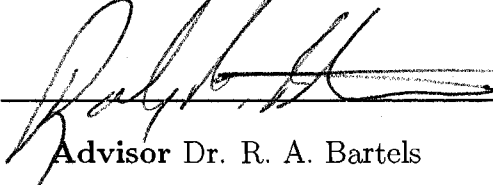
Dr. S.-A. Lee



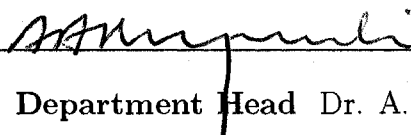
Dr. C. S. Menoni



Dr. J. J. Rocca



Advisor Dr. R. A. Bartels



Department Head Dr. A. A. Maciejewski

ABSTRACT OF DISSERTATION
PROPAGATION AND FREQUENCY CONVERSION OF ULTRASHORT
PULSES IN THE PRESENCE OF COHERENT NUCLEAR MOTION

We have investigated linear as well as nonlinear propagation effects on a relatively weak ultrashort pulse arising from coherent nuclear motion. To this end, we have developed analytical and numerical models used to calculate the molecular response to a strong, ultrashort pump pulse, and propagate a weak probe pulse in the presence of the nuclear wave packet. The molecular response is described in terms of an "effective" susceptibility, which can be split into linear and nonlinear contributions. While a lot of what is discussed in terms of propagation effects is applicable to both rotational and vibrational wave packets, molecular alignment, i.e., coherent rotational motion of linear molecules, is where the focus lies. We have applied spectral interferometry to detect molecular alignment, both in scanning and single-shot configurations, to observe propagation effects due to the effective linear susceptibility, as well as carried out calculations and measurements showing the dependence of the effective third-order susceptibility on coherent nuclear motion. Lastly, a strong enhancement in the conversion efficiency to the third harmonic of a relatively weak probe pulse is observed in a variety of molecular and atomic gases.

Klaus Karl Hartinger
Electrical and Computer Engineering
Colorado State University
Fort Collins, CO 80523
Fall 2008

Acknowledgments

Contents

1	Introduction	1
I	Theory	6
2	The propagation of an ultrafast pulse	7
2.1	The Propagation Equation	9
2.1.1	Derivation of the Wave Equation	10
2.1.2	Slowly Varying Envelope in the Spectral Domain	12
2.2	The current density due to a laser induced plasma	15
2.3	The non-linear induced polarization	17
2.4	Numeric implementation	21
3	Nonlinear polarization for gaseous media	23
3.1	Coherent nuclear motion	25
3.1.1	The Born-Oppenheimer Approximation	29
3.1.1.1	Relevant terms for first, third, and fifth order	31
3.2	Coherent rotational nuclear motion	36
3.2.1	Solution to Schrödinger Equation for an impulsively excited rotational wave packet	38
3.2.1.1	Setting up the model	38
3.2.1.2	Results for the orientational probability distribution	50

3.2.1.3	Accuracy of impulsive approximation	53
3.3	Effective susceptibilities due to coherent nuclear motion	59
3.3.1	Effective linear susceptibility tensor for rotations using the an- alytic model	60
3.3.2	The transient non linear susceptibility for rotations using the analytic model	64
3.4	Laser Pulse Propagation in the presence of coherent nuclear motion .	68
3.4.1	Propagation effects due to $\bar{\chi}^{(1)}(t)$	72
3.4.2	Propagation effects due to $\bar{\chi}^{(3)}(t)$	75
3.4.2.1	Modulation of THG due to CNM	77
4	Dynamically structured nonlinearity for Quasi Phase Matching	79
4.1	Dynamically Structured Nonlinearities with CNM	82
4.2	Proposed experimental setup	86
4.3	Estimation of achievable enhancement	91
II	Experimental Observations	96
5	Propagation effects due to "linear" susceptibility modulation	99
5.1	Spectral Interferometry as a way to detect molecular alignment . . .	99
5.2	Single Shot Measurement of Temporal Phase Modulation	101
5.2.1	Phase accumulation and birefringence due to a rotational wave packet	102
5.2.2	Chirped Spectral Interferometry	103
5.2.3	$\chi_{\text{eff}}^{(1)}(t)$ in the presence of a rotational wave packet	104
5.2.4	Experimental setup	105
5.2.5	Analysis of experimental results	107
5.2.6	Summary	110

5.3	Modification of Group Velocity due to molecular alignment	110
5.3.1	Experimental investigations	111
5.3.1.1	Experimental Results	112
5.3.2	Modelling Group Velocity Modification due to $\chi^{(1)}(\tau)$	115
5.4	Transient Birefringence in a gas - A Transient Waveplate	117
5.4.1	Experimental Setup	118
5.4.2	Theory	119
5.4.3	Weak phase modulation	123
5.4.4	Moderate phase accumulation	124
5.4.5	Strong Phase Modulation	126
5.4.6	Summary	127
6	Non-linear optical frequency conversion	128
6.1	Third Harmonic Generation in the presence of a rotational wave packet	129
6.1.1	Theory of Third Harmonic Generation in the presence of a rotational wave packet	130
6.1.2	Experimental Setup	133
6.1.3	Results for the modulation of THG due to molecular alignment	134
6.1.4	Modeling of the experiment	137
6.1.5	Modulation of THG due to coherent vibrational motion	139
6.1.5.1	Modulation of THG in SF ₆	140
6.1.6	Concurrent detection of effective linear and nonlinear susceptibility contribution	141
6.1.7	Summary	143
6.2	Enhanced efficiency for Third Harmonic Generation in the gas phase	144
6.2.1	Experimental setup	145
6.2.2	Observations of enhanced THG	146
6.2.3	Summary	150

List of Tables

I	Type I and Type II processes allowed for third order interaction between a linearly polarized field with polarization direction in the $\hat{x}\hat{z}$ -plane	131
II	Gases used in the experiment with their respective ionization potential in eV. The enhancement quoted is the peak enhancement found in the pressure scans with a 30 cm and 50 cm focal length mirror and 140 mW probe power.	151

List of Figures

- 3.1 b_L^0 -coefficients for L=2 (blue), L=4 (red), and L=6 (black) for circularly (a), elliptically (b), and linearly (c) polarized pump pulses with a peak intensity of $3 \cdot 10^{14}$ W/cm², a pulse duration of 20 fs, and a gas temperature of 50 K. The pump pulse propagates along \hat{z} . The orientational probability distribution corresponding to the respective pump pulse polarization is shown to the right of each panel at the peak of the quarter revival at $\tau = 10.6$ ps. 51
- 3.2 (a) Alignment of CH₃I at T=10 K for a linearly polarized pulse resulting in $P_{\text{lin}} = 10.26$. (b) Effect due to centrifugal distortion on the full revival of the rotational wave packet comparing the first (dashed, red) to the 30th (blue, solid) full revival. 53

3.3	<p>(a) Comparison of relative error in $\langle\langle\cos^2\theta(\tau)\rangle\rangle$ for three different combinations of pulse intensity and duration, each resulting in a kick strength of $P_{\text{lin}} = 5.13$: $I_o = 2.5 \cdot 10^{13}\text{W/cm}^2$ and $\tau = 80$ fs (blue), $I_o = 5 \cdot 10^{13}\text{W/cm}^2$ and $\tau = 40$ fs (red), $I_o = 2 \cdot 10^{14}\text{W/cm}^2$ and $\tau = 10$ fs (green). Clearly, the relative error increases with pulse duration for a fixed kick strength. (b) The relative error for $P_{\text{lin}} = 2.56$ ($I_o = 2 \cdot 10^{14}\text{W/cm}^2$, $\tau = 5$ fs, blue) compared to $P_{\text{lin}} = 5.13$. Case I: $I_o = 4 \cdot 10^{14}\text{W/cm}^2$, $\tau = 5$ fs (black); Case II: $I_o = 2 \cdot 10^{14}\text{W/cm}^2$, $\tau = 10$ fs (red). The loss in accuracy is higher for longer pulse durations, rather than higher pulse intensities.</p>	58
4.1	<p>Typical molecular alignment vs. time induced in a linear molecule (shown here is the time-scale for CO_2). The figure shows that the alignment of the molecular ensemble is significantly modified only near revival events. The labels τ_I, τ_{II}, and τ_{III} refer to times of molecular alignment, anti-alignment, and non-alignment during the transient molecular alignment.</p>	86
4.2	<p>In the dynamic QPM concept, a spatio-temporally controlled ultrafast alignment pulse propagating in the x-direction creates a spatially modulated molecular alignment that evolves in time. A properly shaped alignment pulse creates a grating in the macroscopic nonlinear optical susceptibility of the molecular gas that is stationary in the group frame of the fundamental pulse. Setting the periodicity of the nonlinear grating to a periodicity of twice the coherence length for third harmonic generation leads to efficient conversion from the fundamental to the third harmonic.</p>	87

4.3	The spatio-temporal evolution of the molecular alignment in the group frame of the fundamental pulse is shown here. For an alignment pulse with no pulse-front tilt (a), the transient alignment begins at each y location simultaneously. With propagation, the delay between the alignment and fundamental pulses, $\tau_{a-f}(y)$, increases at the rate of the fundamental pulse group velocity (b). The variation in $\tau_{a-f}(y)$ results in an evolution of the molecular alignment experienced by the fundamental pulse with propagation (c). By matching the group-delay of the fundamental pulse and pulse-front tilt of the alignment pulse [i.e. TWE criterion] (d), a stationary alignment-fundamental pulse delay [i.e., $\tau_{a-f}(y) = \text{const}$] (e) and thereby a constant alignment with propagation [i.e., $\langle\langle \cos^2 \theta(y) \rangle\rangle = \text{const}$] (f) can be selected.	88
4.4	A nonlinear susceptibility grating in the frame of the propagating fundamental pulse can be formed by (a) spatially modulating the alignment pulse intensity and meeting the TWE criterion or by (b) modulating the pulse front delay of the alignment pulse to modulate the alignment strength experienced by the fundamental pulse.	90
4.5	Conversion efficiency for a 50-fs fundamental pulse propagating in a $60 \mu\text{m}$ (dashed) and $21.7 \mu\text{m}$ [GVM-compensated] (solid) diameter hollow-core fiber filled with C_2H_2 . The insets show the third harmonic pulse shapes after 2(a), 4(b), and 6(c) cm of propagation.	94
4.6	Normalized spectra of fundamental (dotted line) and third harmonic pulses (solid line) after 6-cm of propagation in a nonlinear grating formed through molecular alignment for $60 \mu\text{m}$ (a) and $21.7 \mu\text{m}$ [GVM-compensated] (b) diameter hollow-core fibers.	95

5.1	(a) Measured interferogram at a gas pressure of 810 Torr. (b) Relative phase between probe and reference pulses. The noise is extremely low since we were using a birefringent crystal to split the probe pulse into a probe-reference pulse pair.	100
5.2	Algorithm for the phase retrieval of a single-shot measurement	104
5.3	Single-shot experimental setup	106
5.4	Relative timing of pump, reference, and probe pulses with respect to the transient index of refraction for scanning (a) and chirped single-shot measurements. (c) Comparison between the phase extracted from scanning (solid line) and single-shot (dashed line) interferograms. . .	108
5.5	Measured single-shot phase accumulated by the probe pulse along \hat{x} (dashed, blue), \hat{z} (dotted, red) and 45° relative to \hat{z} (solid, green) for a wave packet excited by a circularly polarized pump pulse.	109
5.6	Measured phase modulation of the probe pulse along \hat{x} (dotted) and along \hat{z} (dashed) due to a wave packet excited by an elliptically polarized pump pulse.	109
5.7	(a) Schematic of experimental setup used for detecting the group velocity modification of a weak probe pulse due to the transient molecular alignment. (b) Centroid of the sideband as a function of pump-probe delay at a gas pressure of 3 Torr. (c) Relative phase accumulated by the probe pulse during the half revival at a gas pressure of 3 Torr. . .	112
5.8	(a) The measured interferogram between the probe and reference pulses after propagation through the fiber which was filled with CO ₂ at 80 Torr. (b) shows the sideband found by inverse-Fourier transforming the interferogram. (c) and (d) show the phase extracted from the sideband and its centroid, respectively.	114

5.9	(a) shows the spectra, (b) the sideband, (c) the extracted phase, and (d) the centroid of the sideband.	115
5.10	(a) shows the calculated interferogram, (b) the extracted sideband, (c) the phase extracted from the sideband, and finally (d) shows the centroid of the sideband	117
5.11	Pump - probe setup for observation of polarization splitting.	119
5.12	(a) Weak phase modulation, (b) moderate phase modulation (c) strong phase modulation	122
5.13	(a) Measured temporal phase modulation along \hat{y} (solid) and \hat{z} (dashed) of the TWP for a propagation direction of $-\hat{x}$ at the quarter revival of the wave packet at a pressure of 57 Torr. (b) Probe spectra recorded after a crossed analyzer. (c) Probe energy transmitted through the analyzer.	124
5.14	Probe spectra measured after an analyzing polarizer near the quarter revival at 570 Torr. The spectral shear along the eigenpolarization directions is shown in (a) for \hat{z} and in (b) for \hat{y} , respectively. (c) shows the modulation of the overlap spectra due to the birefringence for $\eta = 45^\circ$.	125
5.15	Measurement of pulse polarization splitting. (a) The reference spectrum is the probe spectrum incident on the TWP. The \hat{z} -pulse (b) and \hat{y} -pulse (c) output spectra are measured with an analyzer parallel and perpendicular to the pump polarization direction, respectively.	126
6.1	(a) Third harmonic spectra recorded for $\eta = 0^\circ$ with the polarizer oriented along the probe pulse polarization at the quarter revival of CO ₂ at 600 Torr. (b) Modulation in energy vs. pump-probe delay for both $\eta = 0^\circ$ (blue) as well as $\eta = 90^\circ$ (green).	133

6.2	Third harmonic spectra recorded for $\eta = 45^\circ$ with the polarizer oriented along the probe pulse polarization at the quarter revival of CO ₂ (a), the half revival of CO ₂ (c), and the half revival of N ₂ (d), all at 600 Torr. (b), (d), and (f) Modulation in energy vs. pump-probe delay for the polarizer oriented along (blue, solid) and orthogonally (red, dashed) to the probe pulse polarization for each case, respectively.	135
6.3	(a) Third harmonic spectra recorded for $\eta = 45^\circ$ with the polarizer oriented along the probe pulse polarization at the half revival of N ₂ O at 300 Torr and (c) TH spectra at the half revival of CO ₂ at 600 Torr. (b) and (d) Modulation in energy vs. pump-probe delay for the polarizer oriented along (blue, solid) and orthogonally (red, dashed) to the probe pulse polarization for each case, respectively.	137
6.4	(color online) (a) Third harmonic spectra calculated for $\eta = 45^\circ$ at the quarter revival of CO ₂ at 600 Torr with a polarizer oriented along the probe pulse polarization. (b) Modulation of the energy vs. pump-probe delay for a polarizer oriented along (blue, solid) and orthogonally (red, dashed) to the probe pulse polarization.	139
6.5	SF ₆ at 600 Torr, pump power 780 mW, probe power 180 mW	141
6.6	(a) Interferogram between strong probe and weak adjacent pulse. (b) Third harmonic spectra due to strong probe pulse, centered around the quarter revival. (c) Extracted relative phase between strong probe pulse and following weak pulse. (d) Modulation of third harmonic energy during the quarter revival.	142
6.7	Recorded third harmonic spectra across the pump-probe time zero in (a) Argon and (b) CO ₂ , both at 600 Torr.	146

6.8	Photodiode signal measuring relative THG average power in Ar (red), SF ₆ (black), CO ₂ (blue, dot-dash), and N ₂ O (red, dashed) with a focal length of 30 cm and and probe and pump pulse energy of 140 and 790 μJ, respectively. The relative THG over a range of pressure is shown both without (a) and with (b) the pump pulse.	148
6.9	(a) THG conversion enhancement for Ne (blue), Ar (red), SF ₆ (black), CO ₂ (blue, dot-dash), and N ₂ O (red, dashed) with 30 cm focal mirror and probe and pump pulse energy of 140 and 790 μJ, respectively. (b) Maximum enhancement observed for Argon with a focal length of 50 cm and the pulse energies given for (a).	150

Chapter 1

Introduction

The topic of molecules subject to intense laser fields has a rich history. In the cw and quasi-cw regime, an electric field produces an angular trap that tends to align molecules along the direction of the trap[1]. The interaction between an off-resonant cw or quasi-cw field and anisotropic molecules is adiabatic, i.e. the molecules' state follows the field and after the field is turned off returns to the initial state. In the pulsed regime, the molecular response may be quite different. Heritage and coworkers demonstrated that a picosecond laser pulse far detuned from excited state absorption in CS₂ produced what they originally referred to as "susceptibility echoes"[2], and later identified as transient birefringence due to quantum beating between rotational states[3]. The quantum beating was observed by Heritage et al. because the duration of the laser pulse interacting with the molecule was much shorter than the rotational period of CS₂. The interaction was therefore impulsive and energy was transferred between the pulse and the molecule via impulsive stimulated Raman scattering.

Renewed interest in the field-free alignment first observed by Heritage et al has been driven by an interest in understanding the rotational wave packets formed by a short alignment laser pulse and by numerous applications. Two excellent reviews on the underlying theory, directions of the field, and applications are [4] and [5]. The

rotational wave packet formed by a short laser pulse is due to a coherent superposition of rotational states. The initial wave packet rapidly dephases and periodically rephases producing fractional and full revivals of the initial rotational wave packet. Initially, the focus lay on linear molecules since the alignment dynamic was easier to interpret than molecules of more complicated symmetry. A modern take on field free molecular alignment can be found in [6]. Different excitation schemes were proposed in order to manipulate the recurring alignment, e.g., controlling the alignment by shaping the excitation pulse[7] or using an elliptically polarized pulse[8]. When using asymmetric-top molecules it is possible to align the molecules in three dimensions using an elliptically polarized laser pulse[9, 10], where Viftrup et al. extended this control in a later experiment by combining a long nano-second pulse with a delayed femtosecond pulse[11]. Applications of rotational wave packets exhibiting field-free alignment include molecular spectroscopy [12], manipulation of ultrafast laser pulses molecular phase modulation[13], control of high harmonic generation[14], phase matching for perturbative nonlinear optics[15], and many others – see [4] for additional application areas. A very recent accomplishment using rotational wave packets is the selective alignment of molecular isotopes as well as spin isomers[16]. By carefully timing the interaction of the molecules with two linearly polarized pulses different isotopes or spin isomers can be detected in a gas mixture, with the goal of ultimately using molecular alignment to separate the mixture into its components.

Much has been explored regarding rotational wave packets already. The focus of this work lies on an aspect which has hitherto been mostly neglected - that of propagation effects in the presence of coherent nuclear motion. While there is a focus on coherent rotational motion of molecules, much of what is explored here specifically for the case of rotational wave packets is true for coherent vibrational motion as well. For that reason, we will often refer to Coherent Nuclear Motion (CNM) to emphasize the applicability of what is being said to both. In Part I of the document we discuss

the theoretical background necessary to understand the propagation of short laser pulses in homogeneous, dilute, non-time stationary media. We specifically discuss the derivation of the nonlinear Schrödinger equation in Chap. 2. The derivation is slightly modified in order to accommodate experimental conditions which are not considered in the standard derivation. Since we discuss propagation effects on ultrashort laser pulses due to CNM, it is necessary to model the rotational and/or vibrational wave packets resulting from the interaction with a strong pump pulse and their effect on the polarization density induced by the weak probe pulse. This is discussed in Chap. 3, where we first review the Born-Oppenheimer approximation in Sec. 3.1. As a result of that derivation it is found that the presence of CNM can be viewed as an "effective" time-dependent susceptibility contribution to the induced polarization density. Many groups have developed numerical simulations specifically for rotational wave packet excitation[6]. To model our experiments, we need to calculate the effective susceptibility resulting from rotational wave packets excited by arbitrarily polarized pump pulses for gases at room temperature. To that end, we have developed an analytic model in the limit of a purely impulsive excitation[17]. The model is presented in Sec. 3.2, and the resulting effective susceptibilities in Sec. 3.3. The contribution of the effective susceptibility to the induced polarization density can be separated into an effective linear, and an effective nonlinear part. The propagation effects observed experimentally are outlined in Sec. 3.4 for both linear and nonlinear contributions. One potential application originating from the time dependence of the effective third order susceptibility is a novel way of quasi-phase matching nonlinear optical frequency conversion[18] which is outlined in Chap. 4.

Part II of the dissertation details the experimental observations regarding propagation effects due to CNM. In Chap. 5 we discuss the effects due to the effective linear susceptibility. We have observed the phase modulation due to molecular alignment in various regimes, from weak to strong phase modulation. In Sec. 5.1 we show that

the transient molecular alignment can be detected using spectral interferometry. This measurement takes advantage of the fact that the index of refraction is modulated during a wave packet revival. In Sec. 5.2 we show how spectral interferometry can be utilized in a slightly modified manner to detect molecular alignment for arbitrarily polarized pump pulses[19]. Then, we discuss briefly a modification of the probe pulse's group velocity due to molecular alignment. This behavior is expected based on theoretical considerations, and has been observed experimentally. However, there is no qualitative agreement between theory and experiment. This discrepancy has as of yet not been resolved. In Sec. 5.4 we show that, as opposed to "standard" birefringent media, the transient birefringence present during molecular alignment leads to the splitting of a linearly polarized probe pulse in the strong phase modulation regime. As mentioned above, the contribution to the induced polarization density due to CNM may be split into linear and nonlinear parts. The nonlinear contribution, particularly the effective third-order susceptibility, is the subject of Chap. 6. It is expected that the conversion efficiency to the third harmonic depends on the pump-probe delay if CNM is present. This has been observed in CO_2 and N_2O for rotational wave packets and SF_6 for vibrational coherent motion. The results for both cases are shown in Sec. 6.1 together with a way of detecting the change in the index of refraction concurrently with the modulation in conversion efficiency to the third harmonic. Improving the efficiency of nonlinear frequency conversion is a very important and active field of research. Moreover, the efficient conversion of a broad bandwidth is a highly sought after goal. The last section of the dissertation, therefore, describes a novel enhancement effect observed for a relatively weak probe pulse. The enhancement is attributed to the presence of a laser-induced plasma at the focal spot. While the exact physics of the enhancement at this point are unknown, experimental results clearly showing the effect in a variety of molecular as well as atomic gases are presented.

Part I

Theory

Chapter 2

The propagation of an ultrafast pulse

The electromagnetic field in space and time is completely described by Maxwell's equations. Solving these equations without adequate approximations, though, requires a substantial amount of computing power. From Maxwell's equations one can derive the wave equation for the electric or magnetic field, which is classified as a hyperbolic second order partial differential equation (PDE). Solving the full wave equation for a particular experimental setup of interest is equally computationally expensive as directly solving Maxwell's equations for the field. In addition to that, solving the wave equation reliably, particularly when a non-linear driving term is present, can be very difficult. Therefore, suitable approximations which significantly reduce the computational effort are often made. The most notable approximation made frequently is the Slowly Varying Envelope Approximation (SVEA), which implies that the backward propagating field is negligible[20]. The approximations may also include the separation of the field into a fast oscillating phase in space and time and a slowly varying envelope, the paraxial approximation, and/or expanding the wave vector in a Taylor series and neglecting dispersion terms above a certain or-

der. A combination of these approximations and the SVEA will reduce the wave equation to unidirectional equations which are typically much easier to handle computationally. The most common example for such an equation which has been used extensively for simulating the non-linear propagation of an ultrashort pulse is the Non-linear Schrödinger equation (NLSE) in various forms[21]. The NLSE can be solved using very robust algorithms and is applicable to a variety of contexts. Given the conditions present in the experiments carried out in this work, the NLSE is sufficient to describe the pulse propagation, given some minor modifications to the traditional NLSE. With ever more intense and shorter pulses, the approximations made in the derivation of the NLSE make its accuracy questionable for highly non-linear and dispersive propagation. More accurate equations have been derived. For few-cycle pulses particularly the Non-linear Envelope Equation (NEE), derived by Brabec et al. [22], has been used quite extensively, since its validity is broader than that of the NLSE particularly in the time domain, i.e., it allows for the simulation of the propagation of very short pulses under non-linear conditions. In order to simulate pulse propagation in the presence of free charges and induced currents, as is the case in filamentation, Kolesik et al. have derived another propagation equation, called the Unidirectional Pulse Propagation Equation (UPPE) by expressing the field in terms of a superposition of electromagnetic modal fields[23, 24]. The UPPE, like the NLSE as well as the NEE, makes the assumption that the backward propagating field is negligible. Two examples for which this assumption breaks down are in the self-focussing regime[25], and for the non-linear propagation of few-cycle pulses in multicomponent media[26]. The primary problem in making the SVEA is of course that it may not be immediately obvious whether or not it applies for a given situation. Apart from this, the UPPE as derived by Kolesik et al. is formally exact for pulse propagation in homogeneous, non-magnetic media and more general than other unidirectional equations since free charges and the corresponding induced current densities are included in the descrip-

tion. The UPPE is particularly useful when highly non-linear propagation effects, e.g., those present under tight focussing conditions, need to be considered, since the paraxial approximation is not being made, nor is the field assumed to be scalar. In the next section we will derive the NLSE with some modifications: We will include the presence of free charges, and hence the resulting current density, and dispersion will be taken into consideration more accurately than merely including second and third order. While the resulting equation thus differs somewhat from the traditional NLSE, its range of validity may be considered largely similar to that of the NLSE. The derivation of the UPPE by Kolesik et al. has been used as a guideline and inspiration for the derivation presented here [27], particularly due to their inclusion of free charges. The reasoning behind not using the UPPE directly is that the generality provided by the UPPE is not necessary for the given experimental conditions.

2.1 The Propagation Equation

In this chapter, the goal will be to derive a propagation equation for the slowly varying envelope of an electric field. The final result will be a unidirectional propagation equation similar to the NLSE. There are three major assumptions which have to be made in order to simplify the wave equation, and which in turn of course limit the range of validity of the resulting propagation equation. The first assumption is to assume a homogeneous medium of non-interacting particles. Secondly, it will be assumed that the pulse will not be too tightly focussed, i.e., the spot size of the beam is always much larger than the wave length (paraxial approximation). Finally, it will be assumed that the contribution of the backward propagating field is negligible, i.e., $P(E) \approx P(E_f)$ and $E \approx E_f$, where E_f denotes the full field[27], which is to say, the slowly varying envelope approximation will be made.

2.1.1 Derivation of the Wave Equation

First, the standard wave equation is derived from Maxwell's equations in the usual manner. Starting with Maxwell's Equations [24]:

$$\nabla \cdot \vec{\mathbf{D}}(\vec{\mathbf{r}}, t) = \rho \quad (2.1)$$

$$\nabla \cdot \vec{\mathbf{B}}(\vec{\mathbf{r}}, t) = 0 \quad (2.2)$$

$$\nabla \times \vec{\mathbf{E}}(\vec{\mathbf{r}}, t) = -\frac{\partial \vec{\mathbf{B}}(\vec{\mathbf{r}}, t)}{\partial t} \quad (2.3)$$

$$\nabla \times \vec{\mathbf{H}}(\vec{\mathbf{r}}, t) = \vec{\mathbf{J}}(\vec{\mathbf{r}}, t) + \frac{\partial \vec{\mathbf{D}}(\vec{\mathbf{r}}, t)}{\partial t}, \quad (2.4)$$

where $\vec{\mathbf{D}}(\vec{\mathbf{r}}, t)$ is the displacement field, ρ is the charge density, $\vec{\mathbf{B}}(\vec{\mathbf{r}}, t)$ is the magnetic induction, $\vec{\mathbf{E}}(\vec{\mathbf{r}}, t)$ is the electric field, $\vec{\mathbf{H}}(\vec{\mathbf{r}}, t)$ is the magnetic field, and $\vec{\mathbf{J}}(\vec{\mathbf{r}}, t)$ is the induced current density. By taking the curl of Faraday's law (Eq. 2.3),

$$\nabla \times \nabla \times \vec{\mathbf{E}}(\vec{\mathbf{r}}, t) = -\nabla \times \frac{\partial \vec{\mathbf{B}}(\vec{\mathbf{r}}, t)}{\partial t}$$

and with $\vec{\mathbf{B}}(\vec{\mathbf{r}}, t) = \mu_o \vec{\mathbf{H}}(\vec{\mathbf{r}}, t)$ in a non-magnetic medium, using Ampere's Law (Eq. 2.4), the wave equation is found to be

$$\nabla \times \nabla \times \vec{\mathbf{E}}(\vec{\mathbf{r}}, t) = -\mu_o \frac{\partial \vec{\mathbf{J}}(\vec{\mathbf{r}}, t)}{\partial t} - \mu_o \frac{\partial^2 \vec{\mathbf{D}}(\vec{\mathbf{r}}, t)}{\partial t^2},$$

Next, substituting for $\vec{\mathbf{D}}(\vec{\mathbf{r}}, t) = \epsilon_o \vec{\mathbf{E}}(\vec{\mathbf{r}}, t) + \vec{\mathbf{P}}(\vec{\mathbf{r}}, t)$, where $\epsilon_o \equiv 1/c^2 \mu_o$ is the permittivity of free space and $\vec{\mathbf{P}}(\vec{\mathbf{r}}, t)$ is the induced polarization,

$$\nabla \times \nabla \times \vec{\mathbf{E}}(\vec{\mathbf{r}}, t) + \frac{1}{c^2} \frac{\partial^2 \vec{\mathbf{E}}(\vec{\mathbf{r}}, t)}{\partial t^2} = -\mu_o \frac{\partial \vec{\mathbf{J}}(\vec{\mathbf{r}}, t)}{\partial t} - \mu_o \frac{\partial^2 \vec{\mathbf{P}}(\vec{\mathbf{r}}, t)}{\partial t^2},$$

According to Helmholtz's theorem[28], any vector field which is zero at infinity, which is true for the electric and magnetic fields, can be written as the sum of a component

that has zero divergence and another that has zero curl, so that

$$\vec{\mathbf{E}}(\vec{\mathbf{r}}, t) = \vec{\mathbf{E}}^\perp(\vec{\mathbf{r}}, t) + \vec{\mathbf{E}}^\parallel(\vec{\mathbf{r}}, t).$$

where $\nabla \cdot \vec{\mathbf{E}}^\perp(\vec{\mathbf{r}}, t) = 0$ is the transverse part of the field and $\nabla \times \vec{\mathbf{E}}^\parallel(\vec{\mathbf{r}}, t) = 0$ is the longitudinal part of the field. With this, $\nabla \times \nabla \times \vec{\mathbf{E}}(\vec{\mathbf{r}}, t)$ can be expressed in terms of the transverse part of the field only:

$$\nabla \times \nabla \times \vec{\mathbf{E}}(\vec{\mathbf{r}}, t) = \nabla \times \nabla \times \left(\vec{\mathbf{E}}^\perp(\vec{\mathbf{r}}, t) + \vec{\mathbf{E}}^\parallel(\vec{\mathbf{r}}, t) \right) = \nabla \times \nabla \times \left(\vec{\mathbf{E}}^\perp(\vec{\mathbf{r}}, t) \right)$$

And since $\nabla \cdot \vec{\mathbf{E}}^\perp(\vec{\mathbf{r}}, t) = 0$,

$$\nabla \times \nabla \times \vec{\mathbf{E}}^\perp(\vec{\mathbf{r}}, t) = \nabla(\nabla \cdot \vec{\mathbf{E}}^\perp(\vec{\mathbf{r}}, t)) - \nabla^2 \vec{\mathbf{E}}^\perp(\vec{\mathbf{r}}, t) = -\nabla^2 \vec{\mathbf{E}}^\perp(\vec{\mathbf{r}}, t)$$

So the wave equation can be rewritten as

$$-\nabla^2 \vec{\mathbf{E}}^\perp(\vec{\mathbf{r}}, t) + \frac{1}{c^2} \frac{\partial^2 \vec{\mathbf{E}}(\vec{\mathbf{r}}, t)}{\partial t^2} = -\mu_o \frac{\partial \vec{\mathbf{J}}(\vec{\mathbf{r}}, t)}{\partial t} - \mu_o \frac{\partial^2 \vec{\mathbf{P}}(\vec{\mathbf{r}}, t)}{\partial t^2}, \quad (2.5)$$

which corresponds to an exact solution for the field. Eq. 2.5 will still result in an accurate description of the field if the current density $\vec{\mathbf{J}}(\vec{\mathbf{r}}, t)$ as well as the polarization $\vec{\mathbf{P}}(\vec{\mathbf{r}}, t)$ are found from the complete field. For that purpose, the complete field can be reconstructed from its transverse components, if necessary[24]. It has been shown that for very intense pulses with strong non-linear interaction, e.g., extreme self-focussing, this is indeed necessary, and the longitudinal contribution to the field may not be neglected[23]. If the focussing of the beam is not extremely tight, it can be assumed that $\vec{\mathbf{E}}^\perp \approx \vec{\mathbf{E}}(\vec{\mathbf{r}}, t)$, which, for the experimental situations at hand, is likely valid. With that in mind, the field is assumed to be a transverse field throughout and the wave equation for a weakly focussed pulse propagating in a homogeneous medium is

given by

$$-\nabla^2 \vec{\mathbf{E}}(\vec{\mathbf{r}}, t) + \frac{1}{c^2} \frac{\partial^2 \vec{\mathbf{E}}(\vec{\mathbf{r}}, t)}{\partial t^2} = -\mu_o \frac{\partial \vec{\mathbf{J}}(\vec{\mathbf{r}}, t)}{\partial t} - \mu_o \frac{\partial^2 \vec{\mathbf{P}}(\vec{\mathbf{r}}, t)}{\partial t^2}, \quad (2.6)$$

i.e., from here on out $\vec{\mathbf{E}}^\perp = \vec{\mathbf{E}}(\vec{\mathbf{r}}, t)$ and $\vec{\mathbf{E}}^\parallel = 0$ will be assumed. Since this assumption restricts the validity of what follows to beams whose focus is not tight, i.e., the smallest spot size is much larger than the central wavelength, the paraxial propagation regime is implied from here on out.

2.1.2 Slowly Varying Envelope in the Spectral Domain

Keeping in mind that the objective is to find an equation which describes the evolution of the field *envelope* under propagation. For this purpose, one has to choose a central frequency and central wave vector, which is most meaningful if the spectrum of the field is not too broadband. Hence, the fast oscillating phase from the field may be separated from a slowly varying, complex envelope so that

$$\vec{\mathbf{E}}(\vec{\mathbf{r}}, t) = \frac{1}{2} \left(\vec{\mathbf{A}}(\vec{\mathbf{r}}, t) e^{i(k_o z - \omega_o t)} + c.c. \right),$$

where ω_o and k_o are the chosen central frequency and wave vector, respectively, and c.c. is the complex conjugate. The spectrum of the field is then given by

$$\vec{\mathbf{E}}(\vec{\mathbf{r}}, \omega) = \frac{1}{2} \left(\int dt \vec{\mathbf{A}}(\vec{\mathbf{r}}, t) e^{-i\omega_o t + ik_o z} e^{i\omega t} + c.c. \right) = \frac{1}{2} \left(\vec{\mathbf{A}}(\vec{\mathbf{r}}, \omega - \omega_o) e^{ik_o z} + c.c. \right).$$

And transforming the transverse directions \hat{x} and \hat{y} into k-space, the field in the spectral domain is given by

$$\begin{aligned} \vec{\mathbf{E}}(k_x, k_y, z, \omega) &= \frac{1}{2} \left(\int dx \int dy \vec{\mathbf{A}}(\vec{\mathbf{r}}, \omega - \omega_o) e^{ik_o z} e^{-ik_x x - ik_y y} + c.c. \right) \\ &= \frac{1}{2} \left(\vec{\mathbf{A}}(k_x, k_y, z, \omega - \omega_o) e^{ik_o z} + c.c. \right). \end{aligned}$$

The induced polarization, $\vec{\mathbf{P}}(\vec{\mathbf{r}}, t)$, can be separated into a linear and non-linear contribution, so that

$$\vec{\mathbf{P}}(\vec{\mathbf{r}}, t) = \vec{\mathbf{P}}_L(\vec{\mathbf{r}}, t) + \vec{\mathbf{P}}_{NL}(\vec{\mathbf{r}}, t).$$

The linear material response $\vec{\mathbf{P}}_L(\vec{\mathbf{r}}, t)$ is given by

$$\vec{\mathbf{P}}_L(\vec{\mathbf{r}}, t) = \epsilon_o \int d\tau S^{(1)}(\tau) : \vec{\mathbf{E}}(\vec{\mathbf{r}}, t - \tau),$$

where $S^{(1)}(\tau)$, which is a tensor quantity, is the linear temporal response function[29].

In the frequency domain,

$$\vec{\mathbf{P}}_L(k_x, k_y, z, \omega) = \epsilon_o \bar{\chi}^{(1)}(\omega) : \vec{\mathbf{E}}(k_x, k_y, z, \omega),$$

where $\bar{\chi}^{(1)}(\omega)$ is the linear susceptibility, given by the Fourier transform of the linear response function, $S^{(1)}(\tau)$. The current density as well as the non-linear induced polarization may also be transformed to the frequency domain, and the wave equation in the spectral domain then reads

$$\begin{aligned} (-k_x^2 - k_y^2 + \frac{\partial^2}{\partial z^2}) \vec{\mathbf{E}}(k_x, k_y, z, \omega) + \frac{\omega^2}{c^2} \bar{\epsilon}_r(\omega) : \vec{\mathbf{E}}(k_x, k_y, z, \omega) = \\ - \frac{i\omega}{c^2 \epsilon_o} \vec{\mathbf{J}}(k_x, k_y, z, \omega) - \frac{\omega^2}{c^2 \epsilon_o} \vec{\mathbf{P}}_{NL}(k_x, k_y, z, \omega), \end{aligned} \quad (2.7)$$

where the differential operators have been formally replaced with their counterparts in the spectral domain, i.e., $\frac{\partial}{\partial t} \rightarrow -i\omega$, $\frac{\partial^2}{\partial t^2} \rightarrow -\omega^2$, $\frac{\partial^2}{\partial x^2} \rightarrow -k_x^2$, and $\frac{\partial^2}{\partial y^2} \rightarrow -k_y^2$, and

$$\bar{\epsilon}_r(\omega) = 1 + \bar{\chi}^{(1)}(\omega).$$

Eq. 2.8 describes the propagation of an electric field in the spectral domain, bearing in mind the stated assumptions which limit its range of validity. Inserting the definition

of the field into Eq. 2.8 results in

$$\begin{aligned} (-k_x^2 - k_y^2 + \frac{\partial^2}{\partial z^2}) \vec{\mathbf{A}}(k_x, k_y, z, \omega - \omega_o) e^{ik_o z} + \frac{\omega^2}{c^2} \bar{\epsilon}_r(\omega) : \vec{\mathbf{A}}(k_x, k_y, z, \omega - \omega_o) e^{ik_o z} = \\ - \frac{i\omega}{c^2 \epsilon_o} \vec{\mathbf{J}}(k_x, k_y, z, \omega - \omega_o) - \frac{\omega^2}{c^2 \epsilon_o} \vec{\mathbf{P}}_{NL}(k_x, k_y, z, \omega - \omega_o) \end{aligned} \quad (2.8)$$

where $\vec{\mathbf{P}}_{NL}(k_x, k_y, z, \omega - \omega_o)$ denotes the contribution to the non-linear induced polarization at the chosen center frequency ω_o . The complex conjugate part of the field results in an identical equation, which for brevity is neglected here. It is kept in mind that of the resulting field the real part is to be taken. Making a last assumption, the slowly varying envelope assumption (SVEA), Eq. 2.8 can finally be written as a unidirectional propagation equation. The implications of this assumption are detailed in [23] and references therein. The final propagation equation which will be employed for calculations is then found to be

$$\begin{aligned} (-k_x^2 - k_y^2 - k_o^2 + i2k_o \frac{\partial}{\partial z}) \vec{\mathbf{A}}(k_x, k_y, z, \omega - \omega_o) e^{ik_o z} + \frac{\omega^2}{c^2} \bar{\epsilon}_r(\omega) : \vec{\mathbf{A}}(k_x, k_y, z, \omega - \omega_o) e^{ik_o z} = \\ - \frac{i\omega}{c^2 \epsilon_o} \vec{\mathbf{J}}(k_x, k_y, z, \omega - \omega_o) - \frac{\omega^2}{c^2 \epsilon_o} \vec{\mathbf{P}}_{NL}(k_x, k_y, z, \omega - \omega_o) \end{aligned}$$

And rearranging terms,

$$\begin{aligned} \frac{\partial \vec{\mathbf{A}}(k_x, k_y, z, \omega - \omega_o)}{\partial z} = \frac{i}{2k_o} \left(\frac{\omega^2}{c^2} \bar{\epsilon}_r(\omega) - k_o^2 - k_x^2 - k_y^2 \right) \vec{\mathbf{A}}(k_x, k_y, z, \omega - \omega_o) \quad (2.9) \\ - \frac{\omega}{c^2 \epsilon_o 2k_o} \vec{\mathbf{J}}(k_x, k_y, z, \omega - \omega_o) + \frac{i\omega^2}{c^2 \epsilon_o 2k_o} \vec{\mathbf{P}}_{NL}(k_x, k_y, z, \omega - \omega_o) e^{-ik_o z} \end{aligned}$$

In order to solve Eq. 2.10 a split-step approach will be taken[30]. Eq. 2.10 can be solved by taking dispersion and diffraction into account in the frequency domain, and the induced current and polarization densities in the time domain. This approach is valid if for a small enough step size it can be assumed that dispersion and diffraction act independently of the non-linear terms. Eq. 2.10 will therefore be split into two equations which will be considered independent of one another over a small enough

step size:

$$\frac{\partial \vec{A}(k_x, k_y, z, \omega - \omega_o)}{\partial z} = \frac{i}{2k_o} \left(\frac{\omega^2}{c^2} \bar{\epsilon}_r(\omega) - k_o^2 - k_x^2 - k_y^2 \right) \vec{A}(k_x, k_y, z, \omega - \omega_o)$$

$$\frac{\partial \vec{A}(x, y, z, t)}{\partial z} = -\frac{i}{c^2 \epsilon_o 2k_o} \frac{\partial \vec{J}(x, y, z, t)}{\partial t} - \frac{i}{c^2 \epsilon_o 2k_o} \frac{\partial^2 \vec{P}_{NL}(x, y, z, t)}{\partial t^2} e^{-ik_o z} \quad (2.10)$$

Written in this form, dispersion and diffraction amount to a simple spectral phase function accumulated in the frequency domain. The time-domain equation may be solved using a technique appropriate for the desired application and accuracy. Often used is a Runge-Kutta-Fehlberg type algorithm when the desired accuracy is not extremely high. A number of simple approaches are discussed in [21]. The split-step approach has been widely used as a method to describe non-linear pulse propagation and may be considered valid so long as the pulses under consideration are only moderately intense and much longer than a single cycle. For intense pulse propagation the linear and non-linear interactions may no longer be considered independently and Eq. 2.10 has to be solved directly either in the frequency or time domain.

2.2 The current density due to a laser induced plasma

For certain experiments we will consider a plasma present in the focal region of a beam, hence, the charge density will not be zero, and neither will the current density. It is for this reason that free charges have not been neglected in this derivation. The current density induced by the field will be limited to convection current. For moderate field strengths a linear, non-relativistic relationship between the field and the current density is appropriate. The current density is then given by[24]

$$\vec{J}(\vec{r}, t) = \rho(\vec{r}, t) \vec{v}(\vec{r}, t),$$

where $\rho(\vec{\mathbf{r}}, t)$ is the charge density and $\vec{\mathbf{v}}(\vec{\mathbf{r}}, t)$ is the velocity of the charges as a function of space and time and is given by the solution to

$$\frac{\partial \vec{\mathbf{v}}(\vec{\mathbf{r}}, t)}{\partial t} = \frac{e}{m_e} \vec{\mathbf{E}}(\vec{\mathbf{r}}, t).$$

The rate of change of the current for a general charge density, which may vary in time and space, for example, due to multi-photon ionization and/or tunneling ionization ([31] and references therein) present as a consequence of the high field intensity is therefore given by

$$\frac{\partial \vec{\mathbf{J}}(\vec{\mathbf{r}}, t)}{\partial t} = \frac{e}{m_e} \rho(\vec{\mathbf{r}}, t) \vec{\mathbf{E}}(\vec{\mathbf{r}}, t) + \vec{\mathbf{v}} \frac{\partial \rho(\vec{\mathbf{r}}, t)}{\partial t}. \quad (2.11)$$

With regards to $\rho(\vec{\mathbf{r}}, t)$, its dependence on space and time may result from various ionization mechanisms, due to the electric field present, or due to a previous, strong pump pulse having ionized the medium and created a charge density in the focal region. If the pulses are strong enough, both tunnel as well as multi-photon ionization may contribute to $\rho(\vec{\mathbf{r}}, t)$ [31]. The first model for obtaining an ionization rate for atoms in an external electromagnetic field where the ionization occurs due to tunneling of an electron through the Coulomb potential barrier was the ADK model[32]. More recently more accurate models incorporating more complex processes like double and multi-photon ionization of not only atoms but also molecules have become necessary due to higher field intensities of modern laser sources. One example of these newer models is the S-matrix formalism (see for example [27],[31] and references therein). If it is so desired, the charge density may be calculated accurately utilizing a sophisticated model for the interaction between a strong field and an atom or molecule. If that is not deemed necessary, a phenomenological description of the resulting charge density may be employed. Then, the rate of change of the charge

density may be parametrized in the following intuitive manner[31]:

$$\frac{\partial \rho(\vec{r}, t)}{\partial t} = aI(\vec{r}, t)\rho(\vec{r}, t) + b(I(\vec{r}, t)) - c\rho(\vec{r}, t) \quad (2.12)$$

The first term describes avalanche free electron generation, the second term multi-photon ionization where b depends on the field in a highly non-linear manner, and lastly, the third term described plasma recombination. In order to find the current density using this description, Eq.'s 2.11 and 2.12 have to be solved as a system of coupled equations.

2.3 The non-linear induced polarization

So far, no limitations have been imposed on the non-linear response of the medium, $\vec{P}_{NL}(\vec{r}, t)$. A wide variety of non-linear interaction can be considered. For molecules, in addition to the purely electronic non-linear response often the Raman response, instantaneous as well as delayed, has to be taken into account. In general, non-linear response functions are complicated to calculate. The procedure for a wide variety of experimental situations and the corresponding non-linear response function is outlined in detail in [29]. For the purpose of this work, it will be assumed that the electronic response of the medium is instantaneous and all non-linear terms higher than third order in $\vec{P}_{NL}(\vec{r}, t)$ will be neglected.

To illustrate the above model for the non-linear response of the medium, we will show here explicitly how it applies to the instantaneous third order response of an isotropic medium, where the interaction is considered off-resonance and only the electronic contribution will be considered, i.e., what follows would apply for example to the interaction of an infrared laser pulse with an atomic gas. Including third order non-linear interaction implies that when starting with a field centered around ω_o , with propagation there will be spectral components generated around $\omega_3 = 3\omega_o$ due

to third harmonic generation. Other self-phase matched interactions occur, such as self phase modulation (SPM) or cross phase modulation (XPM). For the purpose of this example, $\vec{\mathbf{J}}(\vec{\mathbf{r}}, t) = 0$. Hence, the field under these circumstances should be described as

$$\vec{\mathbf{E}}(k_x, k_y, z, \omega) = \frac{1}{2} \left(\vec{\mathbf{A}}_o(k_x, k_y, z, \omega - \omega_o) e^{ik_o z} + \vec{\mathbf{A}}_3(k_x, k_y, z, \omega - \omega_3) e^{ik_3 z} + c.c. \right),$$

where $\vec{\mathbf{A}}_o(k_x, k_y, z, \omega - \omega_o)$ and $\vec{\mathbf{A}}_3(k_x, k_y, z, \omega - \omega_3)$ are the slowly varying envelopes centered at ω_o and ω_3 , respectively. Eq. 2.8 can then be split into two coupled equations, describing the evolution of the fundamental and third harmonic fields interacting via $\vec{\mathbf{P}}_{NL}(k_x, k_y, z, \omega)$. This result can be applied quite generally to a wide variety of situations. The limitations, given by the assumptions made in the process of the derivation, are most importantly that the non-linear contribution to $\vec{\mathbf{P}}(\vec{\mathbf{r}}, t)$ is small compared to the linear contribution, as well as that the medium be homogeneous and consist of non-interacting particles.

The initial field is taken to be linearly polarized with a Gaussian distribution in the transverse directions as well as time, i.e., the field in space and time is given by

$$E(x, y, z, t) = A_o(x, y, z, t) e^{ik_o z - i\omega_o t} = E_o e^{-x^2/w_o^2 - y^2/w_o^2} e^{i\phi(x, y, z)} e^{-2 \log 2 t^2 / \tau_o^2} e^{ik_o z - i\omega_o t},$$

where τ_o it the initial pulse duration at FWHM, and w_o is the initial beam waist with an arbitrary spatial phase $\phi(x, y, z)$ which is useful, for example, if the interaction of a focussing beam with the medium is supposed to be found by propagating said field with Eq. 2.8.

The third order contribution to the non-linear polarization can have a very large number of terms centered around a variety of distinct temporal as well as spatial frequencies. The conversion efficiency from the fundamental to the third harmonic is very low, however, so any non-linear processes due to the third harmonic field

can be neglected. Direct higher harmonic generation is increasingly non-efficient due to the increased phase mismatch as well as reabsorption by the medium, and is therefore neglected as well. Therefore, all contributions oscillating at frequencies other than ω_o and ω_3 will be neglected. Since the frequency dependence of the non-linear susceptibility tensor is often not known, it is assumed as constant with respect to frequency. This implies that the interaction of the field with the medium takes place instantaneously, and as a consequence, $P_{NL}(\vec{r}, t)$ can be written as

$$P_{NL}(\vec{r}, t) = \epsilon_o \chi^{(3)} E(x, y, z, t) E(x, y, z, t) E(x, y, z, t)$$

With the field defined in terms of the slowly varying envelopes, the non-linear induced polarization can be rewritten in terms of a fast oscillating phase and a slowly varying envelope accordingly:

$$\begin{aligned} P_{NL}(x, y, z, t) = & \epsilon_o \frac{\chi^{(3)}}{8} (3A_o(x, y, z, t)A_o^*(x, y, z, t)A_o(x, y, z, t)e^{ik_o z - i\omega_o t} \\ & + 6A_3(x, y, z, t)A_3^*(x, y, z, t)A_o(x, y, z, t)e^{ik_o z - i\omega_o t} \\ & + 3A_o^*(x, y, z, t)A_o^*(x, y, z, t)A_3(x, y, z, t)e^{i(-2k_o + k_3)z - i\omega_o t} \\ & + 3A_3(x, y, z, t)A_3^*(x, y, z, t)A_3(x, y, z, t)e^{ik_3 z - i\omega_3 t} \\ & + 6A_o(x, y, z, t)A_o^*(x, y, z, t)A_3(x, y, z, t)e^{ik_3 z - i\omega_3 t} \\ & + A_o(x, y, z, t)A_o(x, y, z, t)A_o(x, y, z, t)e^{i3k_o z - i\omega_3 t}, \end{aligned}$$

where SPM, XPM, THG and back conversion are taken into consideration. Each contribution to $P_{NL}(x, y, z, t)$ can be Fourier transformed separately, so that in the frequency domain

$$\begin{aligned}
P_{NL}(k_x, k_y, z, \omega) &= \epsilon_o \frac{\chi^{(3)}}{8} (p_{o,SPM}(k_x, k_y, z, \omega - \omega_o) e^{ik_o z} \\
&+ p_{o,XPM}(k_x, k_y, z, \omega - \omega_o) e^{ik_o z} \\
&+ p_{o,BC}(k_x, k_y, z, \omega - \omega_o) e^{i(-2k_o+k_3)z} \\
&+ p_{3,SPM}(k_x, k_y, z, \omega - \omega_3) e^{ik_3 z} \\
&+ p_{3,XPM}(k_x, k_y, z, \omega - \omega_3) e^{ik_3 z} \\
&+ p_{3,THG}(k_x, k_y, z, \omega - \omega_3) e^{i3k_o z}.
\end{aligned}$$

$p_{i,j}$ are the corresponding slowly varying envelopes obtained by Fourier transforming the corresponding triple product of the slowly varying envelopes in the time domain. Finally, the two coupled equations for the slowly varying envelopes in the spectral domain can be found by inserting the above into Eq. 2.8:

$$\begin{aligned}
\frac{\partial A_o(k_x, k_y, z, \omega - \omega_o)}{\partial z} &= \frac{i}{2k_o} \left(\frac{\omega^2}{c^2} \epsilon_r(\omega) - k_o^2 - k_x^2 - k_y^2 \right) A_o(k_x, k_y, z, \omega - \omega_o) \\
&+ \frac{i\omega^2}{c^2 \epsilon_o 2k_o} P_{NL}(k_x, k_y, z, \omega - \omega_o) e^{-ik_o z} \quad (2.13)
\end{aligned}$$

$$\begin{aligned}
\frac{\partial A_3(k_x, k_y, z, \omega - \omega_3)}{\partial z} &= \frac{i}{2k_3} \left(\frac{\omega^2}{c^2} \epsilon_r(\omega) - k_3^2 - k_x^2 - k_y^2 \right) A_3(k_x, k_y, z, \omega - \omega_3) \\
&+ \frac{i\omega^2}{c^2 \epsilon_o 2k_3} P_{NL}(k_x, k_y, z, \omega - \omega_3) e^{-ik_3 z} \quad (2.14)
\end{aligned}$$

where $P_{NL}(k_x, k_y, z, \omega - \omega_i)$ with $i \in \{o, 3\}$ denotes the contribution to the non-linear induced polarization centered around the fundamental and third harmonic frequencies respectively. The separation of the fundamental and third harmonic envelopes carried out above implies also that the spectra are well separated.

If the split-step approach is taken, four equations have to be solved simultaneously. Only taking into account SPM and back conversion for the fundamental and XPM

and THG for the third harmonic, these equations are given by

$$\begin{aligned}\frac{\partial A_o(k_x, k_y, z, \omega - \omega_o)}{\partial z} &= \frac{i}{2k_o} \left(\frac{\omega^2}{c^2} \epsilon_r(\omega) - k_o^2 - k_x^2 - k_y^2 \right) A_o(k_x, k_y, z, \omega - \omega_o) \\ \frac{\partial A_o(x, y, z, t)}{\partial z} &= \frac{i\omega_o^2 \chi^{(3)}}{8c^2 k_o} (3A_o(x, y, z, t)A_o^*(x, y, z, t)A_o(x, y, z, t) \\ &+ 3A_o^*(x, y, z, t)A_o^*(x, y, z, t)A_3(x, y, z, t)e^{-i\Delta kz}) \quad (2.15)\end{aligned}$$

$$\begin{aligned}\frac{\partial A_3(k_x, k_y, z, \omega - \omega_3)}{\partial z} &= \frac{i}{2k_3} \left(\frac{\omega^2}{c^2} \epsilon_r(\omega) - k_3^2 - k_x^2 - k_y^2 \right) A_3(k_x, k_y, z, \omega - \omega_3) \\ \frac{\partial A_3(x, y, z, t)}{\partial z} &= \frac{i\omega_3^2 \chi^{(3)}}{8c^2 k_3} (6A_o(x, y, z, t)A_o^*(x, y, z, t)A_3(x, y, z, t) \\ &+ A_o(x, y, z, t)A_o(x, y, z, t)A_o(x, y, z, t)e^{i\Delta kz}) \quad (2.16)\end{aligned}$$

If dispersion, diffraction, and non-linear phase accumulation are neglected, and in addition to that, if the conversion efficiency is low, the fundamental field doesn't change and the equations describing the evolution of the field simplify to

$$\begin{aligned}\frac{\partial A_o(x, y, z, t)}{\partial z} &= 0 \\ \frac{\partial A_3(x, y, z, t)}{\partial z} &= \frac{i\omega_3^2 \chi^{(3)}}{8c^2 k_3} A_o(x, y, z, t)A_o(x, y, z, t)A_o(x, y, z, t)e^{i\Delta kz}.\end{aligned}$$

The solution to these equations can be found analytically and is given as a standard description of optical frequency conversion in any non-linear optics textbook[33].

2.4 Numeric implementation

The Eq.'s 2.10 are unidirectional z-propagation equations which can be integrated directly in order to find the field envelope from the known initial conditions. The frequency domain equation taking into account dispersion and diffraction has a simple analytic solution, namely, the field at any point z is given by the initial field multiplied by a phase factor. In order to take into account any non-linear contributions in the time domain, Eq. 2.10(b) can be solved using a standard ordinary differential

equation (ODE) solver, for example the Runge-Kutta-Fehlberg algorithm, which has been employed here. This split step algorithm has been employed for a wide variety of pulse propagation problems[21]. Particular attention has to be paid to the step size since the assumption that the linear and nonlinear contributions to the induced polarization act independently certainly breaks down for large step sizes. As a consequence, this approximation will then introduce a significant error. A slight modification of the split step algorithm is to apply dispersion and diffraction from z_0 to $z_0 + \Delta z/2$, propagate the non-linear contributions also over the same sub-intervall, and repeat the same procedure for the second half of Δz . With this, the actual correlation between linear and non-linear propagation is approximated. If the propagation effects are strong, the interval can be divided into as many sub-steps as need to ensure proper results.

The algorithms and libraries used in the implementation were John Burkardt's implementation of the Runge-Kutta-Fehlberg algorithm using adaptive step size and error management. It can be found at http://people.scs.fsu.edu/~burkardt/cpp_src/rkf45/rkf45.html. Also, the Fast Fourier Transform algorithm used was the FFTW version 3.1.2 obtainable from <http://www.fftw.org/>. For a variety of useful functions and algorithms the GNU Scientific Library (GSL) is a great resource and can be downloaded as well from <http://www.gnu.org/software/gsl/>. For the Graphic User Interface the Qt libraries have been used, obtainable for Linux, Mac OS X, and Windows from <http://www.trolltech.com>. All libraries employed are available for free. The time required to carry out a propagation, of course, strongly depends on the chosen parameters, but can be limited to 2 hours or less for a 1 m propagation on an AMD X2 3GHz computer running Gentoo Linux with 2GB of RAM. Minimum RAM required for the program to run efficiently is about 400 MB.

Chapter 3

Nonlinear polarization for gaseous media

The macroscopic polarization induced by a relatively weak probe pulse may be influenced by any coherent motion of the electrons, the nuclei, or a combination of both[29]. In the case of off-resonant interaction, which is the regime employed throughout this work, there is no coherent electronic motion since the electrons always remain in their ground state and the pulse duration is much longer than $\tau_e = 2\pi/\omega_e$, where $\omega_e = \Delta E_e/\hbar$, and ΔE_e is the energy gap between the electronic ground state and first excited state. However, the time scale of nuclear motion is much slower and stimulated Raman scattering can result[33]. The instantaneous, as well as the delayed Raman response of the nuclei will significantly affect the macroscopic electronic response of the medium and is often of interest since it allows the detection of coherent rotational and/or vibrational motion of the nuclei[34, 35]. This coherent state of superposition of vibrational or rotational states will persist long after the excitation pulse has passed if dephasing, for example due to collisions, is not significant. This is particularly true for molecules in a gaseous phase[4]. For liquid phase molecules, the de-coherence times are much shorter than in the gas phase, on the order of a

few pico-seconds at the most as compared to tens of even hundreds of pico-seconds in a gas. Therefore, a weak probe pulse which is delayed in time with respect to the pump pulse can probe the presence of the nuclear wave packets. The coherent nuclear motion will affect the induced electrical polarization of the probe pulse, which, as will be shown, may be expressed in terms of an "effective" time-varying susceptibility[29]. This principle applies to the linear as well as non-linear propagation of the pulse[18]. For example, the effective linear susceptibility results in a temporal phase modulation of the probe pulse, i.e., the spectrum of the pulse is reshaped due to the interaction of the probe pulse with the wave packet[13]. The detailed effect of the wave packet on the probe pulse depends on the relative time scales of the effective susceptibility and that of the pulse. Throughout it will be assumed that the probe pulse is weak and does not affect the wave packet. The 'effective susceptibility' approach to modeling the effect of a nuclear wave packet on the propagation of a delayed weak probe pulse is applicable to coherent rotational, vibrational, or ro-vibrational motion of the nuclei.

In Sec. 3.1 the Born-Oppenheimer Approximation (BOA)[36] is applied to the non-linear response of the molecules in order to find an expression for the response functions for the coherent motion of the nuclei excited by the strong pump pulse. This approach is applicable to rotational as well as vibrational motion so long as the pump pulse is not too intense since the approach taken in Sec. 3.1 is limited to a perturbative interaction. The motivation for investigating rotational wave packets is outlined in Sec. 3.2 and an analytic model based on an effective Hamiltonian valid for off-resonance interaction is derived which allows for the calculation of the effective susceptibilities, both linear and non-linear, in the presence of a rotational wave packet. The model is compared to an exact numeric solution of the Schrödinger equation and the resulting effective linear and third order susceptibilities are presented. This model is not perturbative, and is therefore valid for arbitrarily strong pump pulses, so long as the molecules are not dissociated. While it is possible to nu-

merically solve the Schrödinger equation for vibrational motion and obtain the wave function for a non-perturbative interaction for vibrations as well, the interaction in the experiments is rather weak, and therefore the results from a perturbative model should be an accurate description. Explicit expressions for the effective susceptibilities due to coherent rotational and vibrational motion are derived for various orders of non-linearity. While it is possible to observe even orders of non-linear interaction in the gas phase in general, for example, second harmonic generation with chiral molecules[37], these do not contribute on a macroscopic level for randomly oriented, non-chiral molecules in gas phase, which will be the only case considered experimentally. Explicit expressions for the effective linear and non-linear susceptibilities will be found in Sec. 3.3, and finally, the resulting effects on a probe pulse during propagation in the presence of nuclear wave packets will be outlined in Sec. 3.4.

3.1 Coherent nuclear motion

General expressions for the third order, non-linear induced polarization have been derived from quantum mechanical principles [29, 38]. However, for the purpose of this work, all interactions between the field and the molecules may be considered off-resonance which significantly simplifies the theoretical considerations. The Born-Oppenheimer Approximation (BOA)[36] is almost universally present in molecular quantum mechanics. There have been cases identified for which the BOA might not be valid, e.g., in photo ionization studies[39], or in situations where energy is transferred between electrons and phonons[40]. It does, however, represent a major simplification in solving the Schrödinger equation for complicated systems. Since the electronic movement is much faster than the motion of the nuclei it can be assumed that the nuclei are "clamped down" as far as the electron motion is concerned. As a consequence, the effect of the electrons on the motion of the nuclei can be described to

zeroth order in the Born-Oppenheimer approximation by an effective potential due to the instantaneous position of the electrons. Since the interaction is off-resonance only the ground state potential surface of the electrons has to be considered. Hellwarth has carried out an extensive analysis of the non-linear response functions given the BOA [38]. In the following, this analysis will be reviewed and the results adapted for the situation at hand, i.e., results specifically for the resulting non-linear contributions to the induced polarization in the presence of rotational and vibrational wave packets excited via stimulated Raman scattering, as well as direct third order contributions will be shown in detail.

In general, the macroscopical induced polarization is given by the expectation value of the induced dipole moment as[41]

$$\vec{P}(\vec{r}, t) = N\langle\mu\rangle,$$

where $\langle \rangle$ indicates the expectation value of an operator and N is the number density.

It is defined as

$$\langle O \rangle \equiv \text{Tr} \{O\rho\}$$

where ρ is the density matrix operator and $\text{Tr}\{\}$ denotes the trace of the operator. The density matrix operator describes the state of a thermal ensemble in general. The fact that the interaction we are interested in is off-resonance considerably simplifies the treatment and will be taken advantage of in what is to come. For a general treatment on the calculation of $\vec{P}(\vec{r}, t)$ for non-linear spectroscopy see Mukamel[29].

It is difficult to find the induced dipole moment for the most general case. Off-resonant interaction is a special case for which it is possible to do just that, however. Utilizing an effective Hamiltonian approach[4] in combination with a purely impulsive interaction allows for an analytic solution of the temporal evolution of the density matrix operator which is not limited to the perturbative regime[17]. However, an

expansion in terms of the electric field is often employed. This expansion is valid as long as the field strengths are less than that of the atomic field, which is on the order of 10^{10}V/m [41]. The density matrix can then be written as

$$\rho(\vec{r}, t) = \rho^{(0)}(\vec{r}, t) + \rho^{(1)}(\vec{r}, t) + \rho^{(2)}(\vec{r}, t) + \rho^{(3)}(\vec{r}, t) + \dots$$

which in turn results in an expansion for the induced polarization in terms of the electric field, so that

$$\vec{P}(\vec{r}, t) = \vec{P}^{(0)}(\vec{r}, t) + \vec{P}^{(1)}(\vec{r}, t) + \vec{P}^{(2)}(\vec{r}, t) + \dots$$

For centro-symmetric media, including isotropically distributed, achiral molecules, there are no even order nonlinear contributions to the macroscopic induced polarization. And for molecules with no permanent dipole, $\vec{P}(\vec{r}, t)$ is given by

$$\vec{P}(\vec{r}, t) = \vec{P}^{(1)}(\vec{r}, t) + \vec{P}^{(3)}(\vec{r}, t) + \vec{P}^{(5)}(\vec{r}, t).$$

In calculating the response of the molecules in gas phase it will be assumed that it is that of non-interacting particles, which will simplify the formalism that follows and is a reasonable assumption for molecules in the gas phase. The spatial dependence of the field will be implicitly assumed without always explicitly showing the argument in order to simplify the notation. This assumption implies a local response of the gas. The i^{th} component of the dipole moment operator is given as

$$\mu_i = \sum_{\alpha=1}^N e_{\alpha} x_{i,\alpha}.$$

The macroscopic polarization is then given by the expectation value of the dipole

moment operator

$$P_i(t) = NTr\{\rho_o[U^{-1}(t, t_o)\mu_i U(t, t_o)]\},$$

where $U(t, t_o)$ is the propagator and given by the solution to

$$\frac{\partial U(t, t_o)}{\partial t} = -\frac{i}{\hbar} [H_o + H_I(t)] U(t, t_o), \quad (3.1)$$

which can be found formally through an iterative procedure of plugging the equation into itself. H_o is the full, unperturbed Hamiltonian of the matter, and $H_I(t) = \mu_i E_i(t)$ is the interaction Hamiltonian in the dipole approximation. The formal solution for the induced dipole moment using Eq. 3.1 is then given by

$$\begin{aligned} U^{-1}(t, t_o)\mu_i U(t, t_o) &= \tilde{\mu}_i(t) + \frac{i}{\hbar} \int_{-\infty}^{\infty} ds [\tilde{\mu}_i(t), \tilde{\mu}_j(s)] E_j(s) + \\ &\quad \left(\frac{i}{\hbar}\right)^2 \int_{-\infty}^{\infty} ds \int_{-\infty}^{\infty} du [[\tilde{\mu}_i(t), \tilde{\mu}_j(s)], \tilde{\mu}_k(u)] E_j(s) E_k(u) + \\ &\quad \left(\frac{i}{\hbar}\right)^3 \int_{-\infty}^{\infty} ds \int_{-\infty}^{\infty} du \int_{-\infty}^{\infty} dv [[[\tilde{\mu}_i(t), \tilde{\mu}_j(s)], \tilde{\mu}_k(u)], \tilde{\mu}_l(v)] \\ &\quad \times E_j(s) E_k(u) E_l(v) + \dots \end{aligned}$$

The tilde over an operator indicates the operator is to be transformed to the interaction picture, so

$$\tilde{\mu}(t) = U_o^{-1}(t)\mu U_o(t),$$

and

$$U_o(t) = e^{-iH_o t/\hbar}.$$

The procedure outlined above, and discussed in detail by Hellwarth[38], allows for the calculation of the induced polarization whose applicability is limited by the fact that a perturbative expansion is utilized, and that the dipole approximation has been made

for the interaction potential. In the following the BOA will be reviewed and it will be shown that the resulting expressions for the induced polarization in the presence of coherent nuclear motion are much simplified. For a more complete discussion, see [38].

3.1.1 The Born-Oppenheimer Approximation

The most important assumption which applies to all experimental situations for the work described in this thesis is that of an off-resonant interaction. The electric field used for the interaction with the atoms and molecules in the experiments is centered around 780 nm, in the infrared. All electronic transitions for the molecules and atoms in question are found in the UV. Hence, the interaction may be considered off-resonance and single-photon absorption can be neglected completely. Hence, if multi-photon excitation is negligible there will not be significant population transfer from the ground electronic state to any upper state. This allows for the introduction of the Born-Oppenheimer Approximation (BOA) to zeroth order, i.e., the motion of electrons and nuclei are considered completely uncoupled. In this limit, the comparatively very slow motion of the nuclei is governed by the potential and kinetic energy of the nuclei, in the presence of a potential energy surface due to the electrons in their ground state. In yet other words, the electrons follow the field adiabatically, while the nuclei don't.

One starts out by finding the ground state energy of the electrons in the presence of the electric field, W_o , given by the Hamiltonian of the system $H = H_o + H_I(t)$ for a given time t . Assuming the nuclei and electrons are decoupled from each other, the interaction Hamiltonian can be separated as

$$H_I(t) = H_{In}(t) + H_{Ie}(t),$$

In order to take into account the perturbation of the field on the electronic ground state energy, a perturbation expansion of the ground state energy W_o in terms of the electric field yields

$$W_o = W_{oo} - (\mu_i E_i(t) + \alpha_{ij} E_i(t) E_j(t) + \beta_{ijk} E_i(t) E_j(t) E_k(t) + \gamma_{ijkl} E_i(t) E_j(t) E_k(t) E_l(t) + \dots) \quad (3.2)$$

W_{oo} is the ground state electronic energy given by H_o in the absence of the electric field. The perturbative correction terms depend on the coordinates of the nuclei. The electronic dipole moment μ^{el} is given by

$$\mu^{el} = -\frac{\partial W_o}{\partial E_i}$$

and in the BOA, the total polarization is then given by the sum of μ^{el} and the polarization of the nuclei,

$$p_i = \sum_{\alpha} e_{\alpha} r_{i\alpha} - \frac{\partial W_o}{\partial E_i},$$

which can be rewritten as

$$p_i = m_i + \alpha_{ij} E_j + \beta_{ijk} E_j E_k + \gamma_{ijkl} E_j E_k E_l + \dots$$

where $m_i = \mu_i + \sum_{\alpha} e_{\alpha} r_{i\alpha}$. The macroscopic induced polarization is then found by

$$P_i(\mathbf{r}, t) = N \text{Tr} \{ \rho_o [U^{-1}(t) p_i(t) U(t)] \},$$

where $U(t)$ is now the solution to

$$\frac{\partial U(t)}{\partial t} = -\frac{i}{\hbar} H_{BO}(t) U(t)$$

and the effective BO Hamiltonian H_{BO} is given by

$$H_{BO} = H_{oN} - (m_i E_i + \alpha_{ij} E_i E_j + \dots)$$

The induced polarization due to the interaction with the electric field is then given by

$$\begin{aligned} U^{-1}(t)p_i(t)U(t) &= \tilde{p}_i(t) + \frac{1}{i\hbar} \int_{-\infty}^{\infty} ds [\tilde{p}_i(t), \tilde{v}(s)] + \\ &\quad \left(\frac{1}{i\hbar}\right)^2 \int_{-\infty}^{\infty} ds \int_{-\infty}^{\infty} du [[\tilde{p}_i(t), \tilde{v}(s)], \tilde{v}(u)] + \\ &\quad \left(\frac{1}{i\hbar}\right)^3 \int_{-\infty}^{\infty} ds \int_{-\infty}^{\infty} du \int_{-\infty}^{\infty} dv [[[\tilde{p}_i(t), \tilde{v}(s)], \tilde{v}(u)], \tilde{v}(v)] + \dots \end{aligned}$$

All that's left to do now in order to find the macroscopic induced polarization operator for any order is to evaluate the trace of the n^{th} term. In the following, it is assumed that the frequencies of the applied electric field are far removed from direct nuclear dipole resonances, i.e., terms with m_i contribute negligibly. For a complete list of terms resulting from the expansion see Steffen et al. [42].

3.1.1.1 Relevant terms for first, third, and fifth order

The induced polarization of first order is given by

$$P_i^{(1)}(t) = N \langle \alpha_{ij} \rangle E_j(t)$$

in the BOA. However, since the index of refraction is often known for the medium in question, the linear response may be taken into account accurately, i.e., the expression for the linear polarization obtained from the above expansion may not have to be utilized.

The next higher order terms are of third order since second order terms of the

expansion are zero for centro-symmetric media. In addition to assuming that the field is off-resonance from any electronic transitions, it will also be assumed that it is not resonant with any direct dipole transition either. This is certainly a valid assumption when fields in the near IR are considered as is the case here. Then, any terms involving the dipole moment m_i are negligibly small and can be neglected. With these assumptions in mind, there are two terms contributing to the third order polarizability:

$$P_i^{(3)}(t) = N\langle\gamma_{ijkl}\rangle E_j(t)E_k(t)E_l(t) + N\frac{i}{\hbar} \int_{-\infty}^{\infty} ds \langle[\tilde{\alpha}_{ij}(t)E_j(t), 1/2\tilde{\alpha}_{kl}(s)E_k(s)E_l(s)]\rangle H(t-s).$$

$\langle \rangle$ indicates the expectation value of the operator, and $H(t)$ is the Heavyside step function which is defined as

$$H(t) = \begin{cases} 0 & \text{if } t < 0 \\ 1 & \text{if } t \geq 0 \end{cases}$$

Rewriting the above expression,

$$\begin{aligned} P_i^{(3)}(t) &= N\langle\gamma_{ijkl}\rangle E_j(t)E_k(t)E_l(t) + N\frac{i}{2\hbar} E_j(t) \int_{-\infty}^{\infty} ds \langle[\tilde{\alpha}_{ij}(t), \tilde{\alpha}_{kl}(s)]\rangle E_k(s)E_l(s)H(t-s) \\ &= N\langle\gamma_{ijkl}\rangle E_j(t)E_k(t)E_l(t) + N\frac{i}{2\hbar} E_j(t) \int_{-\infty}^{\infty} ds \langle(\tilde{\alpha}_{ij}(t)\tilde{\alpha}_{kl}(s) - \tilde{\alpha}_{kl}(s)\tilde{\alpha}_{ij}(t))\rangle \\ &\quad \times E_k(s)E_l(s)H(t-s) \end{aligned}$$

The product of $\tilde{\alpha}_{ij}(t)\tilde{\alpha}_{kl}(s)$ is explicitly given by

$$\begin{aligned} \tilde{\alpha}_{ij}(t)\tilde{\alpha}_{kl}(s) &= U^{-1}(t)\alpha_{ij}U(t)U^{-1}(s)\alpha_{kl}U(s) \\ &= e^{i/\hbar H_0 t}\alpha_{ij}e^{-i/\hbar H_0 t}e^{i/\hbar H_0 s}\alpha_{kl}e^{-i/\hbar H_0 s} \end{aligned}$$

Expressing the polarizability operator in an orthonormal, complete basis set (e.g., the normal vibrational coordinates of a molecule) $|q\rangle$, the trace of the second term of

$P^{(3)}(t)$ is given by

$$\begin{aligned}
\langle\langle \tilde{\alpha}_{ij}(t)\tilde{\alpha}_{kl}(s) - \tilde{\alpha}_{kl}(s)\tilde{\alpha}_{ij}(t) \rangle\rangle &= \sum_q P(q) \langle q | e^{i/\hbar H_0 t} \alpha_{ij} e^{-i/\hbar H_0 t} e^{i/\hbar H_0 s} \alpha_{kl} e^{-i/\hbar H_0 s} | q \rangle - c.c. \\
&= \sum_q P(q) \sum_{n,k} e^{i/\hbar E_q t} \langle q | \alpha_{ij} | n \rangle \langle n | e^{-i/\hbar H_0 t} e^{i/\hbar H_0 s} | k \rangle \langle k | \alpha_{kl} | q \rangle \\
&\quad \times e^{-i/\hbar E_q s} - c.c. \\
&= \sum_q P(q) \sum_{n,k} e^{i/\hbar E_q (t-s)} \langle q | \alpha_{ij} | n \rangle \langle n | e^{i/\hbar H_0 (s-t)} | k \rangle \langle k | \alpha_{kl} | q \rangle \\
&\quad - c.c. \\
&= \sum_q P(q) \sum_n e^{i/\hbar E_q (t-s)} e^{i/\hbar E_n (s-t)} \langle q | \alpha_{ij} | n \rangle \langle n | \alpha_{kl} | q \rangle - c.c. \\
&= \sum_q P(q) \sum_n e^{i\omega_{qn}(t-s)} \langle q | \alpha_{ij} | n \rangle \langle n | \alpha_{kl} | q \rangle - c.c.
\end{aligned}$$

$P(q)$ is the statistical weight of $|q\rangle$, usually given by the Boltzmann statistics plus the nuclear statistical weights determined by the spin statistics of the molecule, and $\omega_{qn} = (E_q - E_n)/\hbar$. With this result, $P^{(3)}(t)$ becomes

$$\begin{aligned}
P_i^{(3)}(t) &= N \langle \gamma_{ijkl} \rangle E_j(t) E_k(t) E_l(t) + N \frac{i}{2\hbar} E_j(t) \int_{-\infty}^{\infty} ds \left\{ \sum_q P(q) \sum_n e^{i\omega_{qn}(t-s)} \right. \\
&\quad \left. \times \langle q | \alpha_{ij} | n \rangle \langle n | \alpha_{kl} | q \rangle - c.c. \right\} E_k(s) E_l(s) H(t-s) \\
&= N \langle \gamma_{ijkl} \rangle E_j(t) E_k(t) E_l(t) + N \frac{i}{2\hbar} E_j(t) \sum_q P(q) \sum_n \langle q | \alpha_{ij} | n \rangle \langle n | \alpha_{kl} | q \rangle \\
&\quad \times \int_{-\infty}^{\infty} ds \left\{ e^{i\omega_{qn}(t-s)} - c.c. \right\} E_k(s) E_l(s) H(t-s)
\end{aligned}$$

Defining $\tau = t - s$, the integral becomes

$$\begin{aligned}
P_i^{(3)}(t) &= N \langle \gamma_{ijkl} \rangle E_j(t) E_k(t) E_l(t) + N \frac{i}{2\hbar} E_j(t) \sum_q P(q) \sum_n \langle q | \alpha_{ij} | n \rangle \langle n | \alpha_{kl} | q \rangle \\
&\quad \times \int_0^{\infty} d\tau (e^{i\omega_{qn}\tau} - c.c.) E_k(t-\tau) E_l(t-\tau)
\end{aligned}$$

And finally,

$$\begin{aligned}
P_i^{(3)}(t) &= N \langle \gamma_{ijkl} \rangle E_j(t) E_k(t) E_l(t) - N \frac{1}{\hbar} E_j(t) \sum_q P(q) \sum_n \langle q | \alpha_{ij} | n \rangle \langle n | \alpha_{kl} | q \rangle \\
&\quad \times \int_0^\infty d\tau \sin(\omega_{qn}\tau) E_k(t - \tau) E_l(t - \tau)
\end{aligned} \tag{3.3}$$

The coherent nuclear motion excited by the field can be described as an effective time varying susceptibility contributing in addition to the direct electronic response of the medium. From the above expression, the effective *linear* susceptibility is given by

$$\chi_{\text{eff}}(t) = -\frac{N}{\epsilon_0 \hbar} \sum_q P(q) \sum_n \langle q | \alpha_{ij} | n \rangle \langle n | \alpha_{kl} | q \rangle \int_0^\infty d\tau \sin(\omega_{qn}\tau) E_k(t - \tau) E_l(t - \tau)$$

This is equivalent to obtaining the density matrix operator resulting after the interaction to first order of perturbation and finding the macroscopic polarization.

There are many fifth order terms resulting from the expansion, but with the assumptions made regarding the off-resonance nature of the interaction, there are only three terms of interest contributing to the fifth order polarizability:

$$\begin{aligned}
P_i^{(5)}(t) &= N \langle \zeta_{ijklmn} \rangle E_j(t) E_k(t) E_l(t) E_m(t) E_n(t) \\
&\quad + N \frac{i}{\hbar} \int_{-\infty}^\infty ds \langle [\tilde{\alpha}_{ij}(t) E_j(t), 1/6 \tilde{\gamma}_{klmn}(s) E_k(s) E_l(s) E_m(s) E_n(s)] \rangle H(t - s) \\
&\quad + N \frac{i}{\hbar} \int_{-\infty}^\infty ds \langle [\tilde{\gamma}_{ijkl}(t) E_j(t) E_k(t) E_l(t), 1/2 \tilde{\alpha}_{mn}(s) E_m(s) E_n(s)] \rangle H(t - s).
\end{aligned}$$

An additional term which has been neglected here, although it has been the focus of intense research over the past decade, is the term proportional to the two-time correlation function

$$\langle [\tilde{\alpha}_{ij}(t), \tilde{\alpha}_{kl}(\tau_2)], \tilde{\alpha}_{mn}(\tau_4) \rangle.$$

This term has been of particular interest in trying to obtain information about the

intermolecular potential between molecules in a liquid. This term describes a fifth-order Raman process. Using novel experimental techniques, the two-dimensional fifth order Raman response of CS₂, for example, has been measured[43] with the ultimate goal of measuring the fifth-order response of water and characterizing its intermolecular potential[44].

In order to obtain a more explicit form for the fifth order terms of interest, we follow steps exactly analogous to the third order term, and find that

$$\begin{aligned}
P_i^{(5)}(t) &= N \langle \zeta_{ijklmn} \rangle E_j(t) E_k(t) E_l(t) E_m(t) E_n(t) \\
&- N \frac{1}{3\hbar} E_j(t) \sum_q P(q) \sum_n \langle q | \alpha_{ij} | n \rangle \langle n | \gamma_{klmn} | q \rangle \int_0^\infty d\tau \sin(\omega_{qn}\tau) \\
&\quad E_k(t - \tau) E_l(t - \tau) E_m(t - \tau) E_n(t - \tau) \\
&- N \frac{1}{\hbar} E_j(t) E_k(t) E_l(t) \sum_q P(q) \sum_n \langle q | \gamma_{ijkl} | n \rangle \langle n | \alpha_{mn} | q \rangle \int_0^\infty d\tau \sin(\omega_{qn}\tau) \\
&\quad E_m(t - \tau) E_n(t - \tau)
\end{aligned}$$

In addition to an effective linear susceptibility, it can be seen that the fifth order response of a medium can be described by an effective *third* order susceptibility given by

$$\chi_{\text{eff}}^{(3)} = -\frac{N}{\epsilon_0 \hbar} \sum_q P(q) \sum_n \langle q | \gamma_{ijkl} | n \rangle \langle n | \alpha_{mn} | q \rangle \int_0^\infty d\tau \sin(\omega_{qn}\tau) E_m(t - \tau) E_n(t - \tau).$$

The above expressions for the effective susceptibilities are valid for any coherent nuclear motion to first order in perturbation. This is somewhat of a limitation when a more accurate description of the interaction between a field and molecule is required. For this reason, the effective linear and third order susceptibilities will be derived again in the following chapter specifically for coherent rotational motion, where the Schrödinger equation will be solved using an effective Hamiltonian in a non-

perturbative regime. That description is valid even for relatively strong interactions, given, of course, that the molecule is not dissociated by the field.

3.2 Coherent rotational nuclear motion

In this Section, the focus will lie specifically on coherent rotational motion. For a variety of reasons, this has been the focus of intense research[4]. Rotational wave packets excited by ultrafast laser pulses in a molecular gas can be observed via an effective time-varying linear susceptibility, as has been mentioned briefly in Sec. 3.1, and may be probed by a time-delayed probe pulse [45, 13]. In early experiments, the rotational coherence was detected through the resulting transient birefringence with a linearly-polarized probe pulse, time-delayed and oriented at 45 degrees with respect to a linearly-polarized pump pulse [45]. More recently, the transient index variation has been used to spectrally broaden and temporally compress a probe pulse co-propagating with the pump pulse by an order of magnitude [13]. This approach has been adapted for UV pulse compression [46]. The spatial distribution of the transient index of refraction has also been exploited to measure the modulus of the induced transient index of refraction change in the gas [47]. Measurements of the transient index of refraction along the two eigen axes of the transient linear susceptibility tensor have also been characterized through scanning spectral interferometry [34] for linearly polarized pump pulses and for arbitrarily-polarized pump pulses with a single-shot chirped spectral interferometry technique [19]. The transient birefringence has also been proposed for phase matching Type II third harmonic generation [15].

Rotational wave packets in gas-phase molecules excited by short, moderately intense laser pulses play an important role in ultrafast optics and strong-field physics. Dynamics of rotational wave packets are important in the interpretation of high harmonic generation experiments [48, 49], strong-field ionization and dissociation [50, 51],

phase modulation of ultrafast pulses [13, 34], and spectroscopy [52, 53, 54, 55, 56]. In such experiments, it is often essential to understand the details of the rotational wave packet and requisite observables in order to interpret experimental results. While many groups have developed numerical simulations for rotational wave packet excitation by linearly and elliptically polarized short laser pulses, analytic models have been limited to linearly polarized excitation pulses and rigid linear molecules ([57, 4] and references therein). Recently, however, the focus of molecular alignment has shifted towards the interaction of more complex, polyatomic molecules with pulses of arbitrary polarization [53, 58, 59].

In order to characterize rotational wave packets created by elliptically-polarized pump pulses in symmetric-top molecules, it is necessary to determine the optical properties of the transiently aligned gas in the presence of the probe pulse. For the case of off-resonant Raman coherences considered here, the relevant properties can be expressed through an effective linear susceptibility of the gas prepared by the pump pulse [29]. Calculation of the effective transient linear susceptibility requires calculation of the density matrix of the molecular ensemble after the impulsive interaction with the pump pulse. For that purpose, we have developed an analytic model for arbitrarily polarized laser pulses interacting with non-rigid, symmetric-top molecules in the sudden-impulse limit. Using this model, we derive a closed form expression for the effective susceptibility due to a rotational wave packet excited by an arbitrarily polarized pump pulse in an ensemble of symmetric-top molecules. It is found that in the proper laboratory frame, with \hat{z} defining the direction of propagation and when \hat{x} and \hat{y} correspond to major and minor axes of the pump pulse polarization ellipse, the effective linear susceptibility is diagonal. For the general case of an elliptically-polarized pump pulse, the gas behaves as a transient bi-axial medium and reduces to a transient uniaxial medium for linear and circularly polarized pulses.

3.2.1 Solution to Schrödinger Equation for an impulsively excited rotational wave packet

The section is organized as follows: In Sec. 3.2.1.1, we present the derivation of the analytic model for rotational wave packet excitation in symmetric top molecules by elliptically-polarized laser pulses. In Sec. 3.2.1.2 calculations of rotational wave packets for various cases are presented, including the effect of centrifugal distortion on the revival structure of the wave packet due to the non-rigidity of the molecules. In order to estimate the validity of the impulsive approximation, the results from the analytic model are compared to a numerical solution of the Schrödinger equation in Sec. 3.2.1.3. And lastly, the model is used to provide an analytic expression for the effective time-dependent susceptibility tensor arising from a rotational coherence in Sec. 3.3.1.

3.2.1.1 Setting up the model

In order to develop an analytic model describing the interaction of an arbitrarily-polarized, ultrafast laser pulse with a symmetric-top molecule, we treat the molecules as non-rigid rotors. The molecules are assumed to remain in their electronic and vibrational ground state throughout, implying an off-resonant interaction. Moreover, alignment pulses with a temporal duration substantially shorter than the rotational period of the molecule are considered so that the interaction is impulsive. The state of a molecular ensemble is then described as a superposition of eigenstates of the non-rigid rotational Hamiltonian, i.e., as a rotational wave packet. The analytic solution found below for the rotational wave packet is for the limiting case of the laser pulse approximated by a delta-function. Vibration-rotation coupling in polyatomic molecules is non-negligible[60], while the rigid rotor approximation is sufficient in accuracy for small molecules such as O₂, N₂, or CO₂ under most circumstances.

The full Hamiltonian for this system is given by $H = H_{\text{mol}} + H_{\text{int}}$, where H_{mol}

denotes the molecular Hamiltonian given by $H_{\text{mol}} = H_o + H_{CD}$ [59] and H_{int} describes the interaction potential due to the alignment laser pulse. H_o is taken to be the standard rigid rotor Hamiltonian,

$$H_o = A_e J_a^2 + B_e J_b^2 + C_e J_c^2.$$

The J_i 's are the cartesian elements of the total angular momentum vector, and the body fixed coordinate system is chosen such that the cross terms in the moment of inertia tensor are eliminated, i.e., the body fixed coordinate system is the principal reference frame. A_e , B_e , and C_e are the rotational constants about the principal axes in the electronic ground state of the molecule, and by convention $A_e \geq B_e \geq C_e$. For prolate symmetric-top molecules it is conventional to choose the body fixed z-axis as the a-axis. Hence, $B_e = C_e$ and with

$$\mathbf{J}^2 = J_a^2 + J_b^2 + J_c^2$$

the rigid rotor Hamiltonian H_o is given by

$$H_o = B_e \mathbf{J}^2 + (A_e - B_e) J_z^2$$

with eigenvalues

$$E_o^{JK} = B_e J(J+1) + (A_e - B_e) K^2$$

For oblate symmetric tops, the z-axis is chosen along the c-axis, and consequently the rigid rotor Hamiltonian reads

$$H_o = B_e \mathbf{J}^2 + (C_e - B_e) J_z^2$$

with eigenvalues

$$E_o^{JK} = B_e J(J+1) + (C_e - B_e) K^2.$$

The additional term in H_{mol} ,

$$H_{CD} = -D_J \mathbf{J}^4 - D_{JK} J_z^2 \mathbf{J}^2 - D_K J_z^2,$$

accounts for the fact that the molecule is not a rigid body. H_{CD} is obtained via the contact transformation due to Van-Vleck [61]. It's eigenvalues are

$$E_{CD}^{JK} = -D_J ((J(J+1))^2 - D_{JK} J(J+1) K^2 - D_K K^4).$$

The normalized Wigner rotation matrices $\langle \phi, \theta, \chi | JKM \rangle \equiv \sqrt{\frac{2J+1}{8\pi^2}} D_{MK}^{J*}(\phi, \theta, \chi)$ are the eigenfunctions of H_{mol} , where the notation used is that in Zare [61].

To find the interaction Hamiltonian H_{int} , we consider an elliptically polarized alignment pulse propagating along \hat{z} of the laboratory frame, given as

$$\mathcal{E}(t) = \frac{1}{2} E(t) e^{i(\omega_o t - k_o z)} (a \hat{x} + ib \hat{y}) + \text{c.c.} \quad (3.4)$$

Here, $E(t)$ denotes the complex pulse amplitude, ω_o is the center optical frequency, and $k_o = n\omega_o/c$ is the wavenumber. The parameters a and b represent the half-axis of the ellipse along two mutually orthogonal directions and simultaneously orthogonal to the direction of propagation. To compare equivalent pulse energies, these parameters must be constrained by $a^2 + b^2 = 1$. It is convenient to define a single ellipticity parameter $A = a^2 - b^2$. Circular polarization, then, corresponds to $A = 0$ while $A = \pm 1$ corresponds to linear polarization. With the alignment pulse defined in Eq.

3.4 the interaction Hamiltonian for off-resonance interactions is given by

$$H_{\text{int}} = -\frac{1}{4} \sum_{\rho, \rho'} \mathcal{E}(t)_\rho^* \alpha_{\rho, \rho'} \mathcal{E}(t)_{\rho'},$$

where $\alpha_{\rho, \rho'}$ is a cartesian component of the polarizability tensor. Finally, the interaction Hamiltonian takes the form of [4]

$$H_{\text{int}} = -\frac{\Delta\alpha}{8} |E(t)|^2 \sin^2 \theta [1 + A \cos 2\phi], \quad (3.5)$$

where $\Delta\alpha = \alpha_{\parallel} - \alpha_{\perp}$ is the difference between the molecular polarizabilities parallel and perpendicular to the principal rotational axis of the molecule.

The solution of the Schrödinger equation for just the material Hamiltonian H_{mol} is given by

$$|\psi_{\text{mol}}(t)\rangle = \exp\left(-\frac{i}{\hbar} H_{\text{mol}} t\right) |\psi_{\text{mol}}(0)\rangle.$$

Defining the unitary operator $U_{\text{mol}}(t, t_o)$ as the solution to

$$\frac{\partial U_{\text{mol}}(t, t_o)}{\partial t} = -\frac{i}{\hbar} H_{\text{mol}} U_{\text{mol}}(t, t_o)$$

with the initial condition $U_{\text{mol}}(t_o, t_o) = 1$ for $t_o = 0$ it is given by

$$U_{\text{mol}}(t, 0) = \exp\left(-\frac{i}{\hbar} H_{\text{mol}} t\right).$$

Let $|\psi_{\text{mol}}(t)\rangle$ be the wave function of the system in the absence of the field, i.e., $H = H_{\text{mol}}$. It is then given by

$$|\psi_{\text{mol}}(t)\rangle = U_{\text{mol}}(t, 0) |\psi_{\text{mol}}(0)\rangle.$$

Defining the state

$$|\psi(t)\rangle \equiv U_{\text{mol}}(t, 0)|\psi_I(t)\rangle$$

and substituting into the Schroedinger Equation,

$$i\hbar \frac{\partial U_{\text{mol}}(t, 0)|\psi_I(t)\rangle}{\partial t} = H U_{\text{mol}}(t, 0)|\psi_I(t)\rangle$$

results in

$$i\hbar U_{\text{mol}}(t, 0) \frac{\partial |\psi_I(t)\rangle}{\partial t} = H_{\text{int}}(t) U_{\text{mol}}(t, 0) |\psi_I(t)\rangle.$$

Multiplying by $U_{\text{mol}}^\dagger(t, 0)$ and defining $V_I(t) \equiv U_{\text{mol}}^\dagger(t, 0) H_{\text{int}}(t) U_{\text{mol}}(t, 0)$,

$$i\hbar \frac{\partial |\psi_I(t)\rangle}{\partial t} = V_I(t) |\psi_I(t)\rangle.$$

Assuming that the interaction is purely impulsive, i.e., the pulse is assumed to be a delta function, $[V_I(t), V_I(t')] = 0 \forall t \neq t'$. Then, the solution for $|\psi_I(t)\rangle$ is simply given by

$$|\psi_I(t)\rangle = \exp\left(-\frac{i}{\hbar} \int_0^t V_I(\tau) d\tau\right) |\psi_I(0)\rangle.$$

Within the impulsive approximation, the laser-molecule interaction may be parametrized with a kick strength parameter, P , which is proportional to the pulse fluence[57] and is defined as

$$P = \frac{\Delta\alpha}{8\hbar} \int_{t_i}^{t_f} |E(t)|^2 dt. \quad (3.6)$$

Then with the impulsive approximation for the field,

$$V_I(\tau) = -P\hbar U_{\text{mol}}^\dagger(\tau, 0) \delta(\tau) \sin^2 \theta (1 + A \cos(2\phi)) U_{\text{mol}}(\tau, 0)$$

and

$$V_I(\tau) = -P\hbar \sin^2 \theta (1 + A \cos(2\phi)) U_{\text{mol}}^\dagger(\tau, 0) \delta(\tau) U_{\text{mol}}(\tau, 0).$$

The wave function is given by

$$|\psi_I(t)\rangle = \exp \left\{ iP \sin^2 \theta [1 + A \cos(2\phi)] \int_0^t U_{\text{mol}}^\dagger(\tau, 0) \delta(\tau) U_{\text{mol}}(\tau, 0) d\tau \right\} |\psi_I(0)\rangle.$$

Since $U_{\text{mol}}(\tau, 0)$ is unitary, the wave function in the interaction picture can be written as

$$|\psi_I\rangle_+ = \exp(iP \sin^2 \theta (1 + A \cos(2\phi))) |\psi_I\rangle_-,$$

where $|\psi_I\rangle_\pm$ are the wave functions immediately preceding ($-$) and following ($+$) the impulsive interaction. The initial state is assumed to be a pure rotational state, given by $|\psi_I\rangle_- = |J_0 K_0 M_0\rangle$. It follows from the effective interaction Hamiltonian given in Eq. 3.5 that only K is conserved. Specific temporal structure, pulse duration, and peak pulse intensity do not independently influence the resultant wave packet for a given laser fluence in this approximation. The resulting error is detailed in Sec. 3.2.1.3 for a variety of laser pulse parameters.

$|\psi_I\rangle_+$ may be expanded in terms of the eigenstates of the molecular Hamiltonian, where the expansion coefficients are given by

$$c_{J,M}^{J_0, K_0, M_0} = \langle J K_0 M | \exp \{ iP \sin^2 \theta [1 + A \cos(2\phi)] \} | J_0 K_0 M_0 \rangle. \quad (3.7)$$

Our objective is to derive an analytic formula for evaluating the expansion coefficients defined in Eq. 3.7. We begin with a Taylor series expansion of the exponential

$$c_{J,M}^{J_0, K_0, M_0} = \sum_{\nu=0}^{\infty} \frac{(iP)^\nu}{\nu!} \langle J K_0 M | \sin^{2\nu} \theta [1 + A \cos(2\phi)]^\nu | J_0 K_0 M_0 \rangle.$$

and expand $[1 + A \cos 2\phi]^\nu$ in terms of cosines of multiple angles. First, using a

binomial expansion,

$$(1 + A \cos(2\phi))^\nu = \sum_{k=0}^{\nu} \binom{\nu}{k} A^k \cos^k(2\phi)$$

where $\binom{\cdot}{\cdot}$ is a binomial coefficient. Subsequently, expanding $\cos^k(2\phi)$ in terms of cosines of multiple angles results in

$$\begin{aligned} \cos^k(2\phi) &= \sum_{n=0}^k b_n^k \cos(2n\phi) \\ \int_0^{2\pi} \cos(2n'\phi) \cos^k(2\phi) d\phi &= \sum_{n=0}^k b_n^k \int_0^{2\pi} \cos(2n'\phi) \cos(2n\phi) d\phi \end{aligned}$$

With the identities

$$\cos^k(2\phi) = \frac{1}{2^{k-1}} \sum_{k'=0}^{\frac{k}{2}-1} \binom{k}{k'} \cos[(k - 2k')2\phi] + \frac{1}{2^k} \binom{k}{\frac{k}{2}}$$

for even k, and

$$\cos^k(2\phi) = \frac{1}{2^{k-1}} \sum_{k'=0}^{\frac{k+1}{2}-1} \binom{k}{k'} \cos[(k - 2k')2\phi]$$

for odd k, the expansion of $\cos^k(2\phi)$ can then be written as

$$\begin{aligned} \int_0^{2\pi} \cos(2n'\phi) \frac{1}{2^{k-1}} \sum_{k'=0}^{\frac{k}{2}-1} \binom{k}{k'} \cos[(k - 2k')2\phi] d\phi + \frac{1}{2^k} \binom{k}{\frac{k}{2}} \int_0^{2\pi} \cos(2n'\phi) d\phi = \\ \sum_{n=0}^k b_n^k \int_0^{2\pi} \cos(2n'\phi) \cos(2n\phi) d\phi \end{aligned}$$

for even k's. Due to the orthogonality of the cosines, $k' = \frac{k-n'}{2}$. Since k is even and both k' and n' have to be integers, n' has to be even as well. So for $n \neq 0$, and k and

n both even,

$$b_n^k = \frac{1}{2^{k-1}} \binom{k}{\frac{k}{2} - \frac{n}{2}}.$$

For odd k's, the same procedure follows and the result for the b-coefficients is identical to the above for both k and n being odd integers, and n is bounded from above by k.

For $n = 0$,

$$b_0^k = \frac{1}{2^k} \binom{k}{\frac{k}{2} - \frac{n}{2}}.$$

Hence, for all k's and n's where again the parity of n and k has to be the same, and $n \leq k$,

$$b_n^k = \frac{1}{2^{k-1+\delta_{n,0}}} \binom{k}{\frac{k}{2} - \frac{n}{2}}.$$

With this, Eq. 3.7 becomes

$$c_{J,M}^{J_0,K_0,M_0} = \sum_{\nu=0}^{\infty} \frac{(iP)^\nu}{\nu!} \sum_{k=0}^{\nu} \binom{\nu}{k} A^k \sum_{n=0}^k b_n^k \langle J K_0 M | \sin^{2\nu}(\theta) \cos(2n\phi) | J_0 K_0 M_0 \rangle. \quad (3.8)$$

Expanding the remaining trigonometric terms in terms of spherical harmonics yields a fully analytic expression for the wave function coefficients. So,

$$\sin^{2\nu} \theta \cos(2n\phi) = \frac{1}{2} \sin^{2\nu} \theta (\exp(i2n\phi) + \exp(-i2n\phi))$$

and

$$\begin{aligned} \sin^{2\nu} \theta e^{i2n\phi} &= \sum_{\ell=2n}^{\infty} g_{\ell,n}^\nu Y_\ell^{2n}(\theta, \phi) \\ \sin^{2\nu} \theta e^{-i2n\phi} &= \sum_{\ell=2n}^{\infty} g_{\ell,n}^\nu \bar{Y}_\ell^{2n}(\theta, \phi) \end{aligned}$$

The expansion coefficients $g_{\ell,n}^\nu$ are the same for both cases and non-zero only for even

ℓ , since 2ν is always even. Using the first case,

$$\begin{aligned}\sin^{2\nu} \theta e^{i2n\phi} &= \sum_{\ell=2n}^{\infty} g_{\ell,n}^{\nu} Y_{\ell}^{2n}(\theta, \phi) \\ \int \bar{Y}_{\ell'}^{2n'}(\theta, \phi) \sin^{2\nu} \theta e^{i2n\phi} d\Omega &= \sum_{\ell=2n}^{\infty} g_{\ell,n}^{\nu} \int \bar{Y}_{\ell'}^{2n'}(\theta, \phi) Y_{\ell}^{2n}(\theta, \phi) d\Omega\end{aligned}$$

Carrying out the integral over ϕ ,

$$g_{\ell,n}^{\nu} = 2\pi \sqrt{\frac{2\ell+1}{4\pi} \frac{(\ell-2n)!}{(\ell+2n)!}} \int_0^{\pi} P_{\ell}^{2n}(\cos \theta) \sin^{2\nu} \theta \sin \theta d\theta$$

Rewriting the integral in terms of $x = \cos \theta$,

$$g_{\ell,n}^{\nu} = 2\pi \sqrt{\frac{2\ell+1}{4\pi} \frac{(\ell-2n)!}{(\ell+2n)!}} \int_{-1}^1 P_{\ell}^{2n}(x) (1-x^2)^{\nu} dx$$

it can be solved analytically [62]:

$$\begin{aligned}g_{\ell,n}^{\nu} &= 2\pi \sqrt{\frac{2\ell+1}{4\pi} \frac{(\ell-2n)!}{(\ell+2n)!}} \\ &\times \frac{\pi 2^{2n} \Gamma(\nu+1+n) \Gamma(\nu+1-n)}{\Gamma(\nu+1+1/2\ell+1/2) \Gamma(\nu+1-1/2\ell) \Gamma(-n+1/2\ell+1) \Gamma(-n-1/2\ell+1/2)}\end{aligned}$$

Then, $\sin^{2\nu} \theta \cos(2n\phi)$ can be written as

$$\sin^{2\nu} \theta \cos(2n\phi) = \frac{1}{2} \sum_{\ell=2n}^{\infty} g_{\ell,n}^{\nu} (Y_{\ell}^{2n}(\theta, \phi) + \bar{Y}_{\ell}^{2n}(\theta, \phi))$$

Since, $Y_J^M(\theta, \phi) = \sqrt{\frac{2J+1}{4\pi}} D_{MK=0}^{J*}(\theta, \phi, \chi)$,

$$c_{JM}^{J_0 K_0 M_0} = \sum_{\nu=0}^{\infty} \frac{(iP)^\nu}{\nu!} \sum_{k=0}^{\nu} \binom{\nu}{k} A^k \sum_{n=0}^k b_n^k \frac{1}{2} \sum_{\ell=2n}^{\infty} g_{\ell,n}^\nu \left(\sqrt{\frac{2\ell+1}{4\pi}} \langle JK_0 M | D_{2n0}^{\ell*}(\theta, \phi, \chi) | J_0 K_0 M_0 \rangle \right. \\ \left. + \sqrt{\frac{2\ell+1}{4\pi}} \langle JK_0 M | D_{-2n0}^{\ell*}(\theta, \phi, \chi) | J_0 K_0 M_0 \rangle \right)$$

The integral over three rotation matrices is given as

$$\int D_{M'_3 M_3}^{J_3}(\theta, \phi, \chi) D_{M'_2 M_2}^{J_2}(\theta, \phi, \chi) D_{M'_1 M_1}^{J_1}(\theta, \phi, \chi) = 8\pi^2 \begin{pmatrix} J_1 & J_2 & J_3 \\ M'_1 & M'_2 & M'_3 \end{pmatrix} \\ \times \begin{pmatrix} J_1 & J_2 & J_3 \\ M_1 & M_2 & M_3 \end{pmatrix},$$

where $\begin{pmatrix} \cdot & \cdot & \cdot \\ \cdot & \cdot & \cdot \end{pmatrix}$ are the Wigner-3j symbols. So,

$$\langle JK_0 M | D_{2n0}^{\ell*}(\theta, \phi, \chi) | J_0 K_0 M_0 \rangle = \sqrt{\frac{2J+1}{8\pi^2}} \sqrt{\frac{2J_0+1}{8\pi^2}} \\ \times \int D_{MK_0}^J(\theta, \phi, \chi) D_{2n0}^{\ell*}(\theta, \phi, \chi) D_{M_0 K_0}^{J_0*}(\theta, \phi, \chi) d\Omega$$

and with the expression for the integral,

$$= (-1)^{K_0+M_0} \sqrt{(2J+1)(2J_0+1)} \begin{pmatrix} J_0 & \ell & J \\ -K_0 & 0 & K_0 \end{pmatrix} \begin{pmatrix} J_0 & \ell & J \\ -M_0 & -2n & M \end{pmatrix}$$

For $\langle JK_0 M | D_{-2n0}^{\ell*}(\theta, \phi, \chi) | J_0 K_0 M_0 \rangle$ the same applies, and the integral evaluates to

$$= (-1)^{K_0+M_0} \sqrt{(2J+1)(2J_0+1)} \begin{pmatrix} J_0 & \ell & J \\ -K_0 & 0 & K_0 \end{pmatrix} \begin{pmatrix} J_0 & \ell & J \\ -M_0 & 2n & M \end{pmatrix}$$

With this, we have found a fully analytic solution for the expansion coefficients of the

wave packet, which are given by

$$\begin{aligned}
c_{J,M}^{J_0,K_0,M_0} &= \frac{(-1)^{K_0+M_0}}{2} (1 + \delta_{M,M_0}) \sqrt{(2J+1)(2J_0+1)} \sum_{\nu=|\Delta M/2|}^{\infty} \frac{(iP)^\nu}{\nu!} \sum_{k=|\Delta M/2|}^{\nu} \begin{pmatrix} \nu \\ k \end{pmatrix} \\
&\times A^k b_{|\Delta M/2|}^k \sum_{\ell=\text{Max}\{|\Delta M|, |J-J_0|\}}^{J+J_0} g_{\ell, \Delta M/2}^\nu \begin{pmatrix} J & \ell & J_0 \\ K_0 & 0 & -K_0 \end{pmatrix} \\
&\times \begin{pmatrix} J & \ell & J_0 \\ M & \Delta M & -M_0 \end{pmatrix}. \tag{3.9}
\end{aligned}$$

where $\Delta M = M_0 - M$ and [62]

$$\begin{aligned}
g_{\ell,n}^\nu &= (2\ell+1) \sqrt{\frac{(\ell-2n)!}{(\ell+2n)!}} \\
&\times \frac{\pi 2^{2n-1} \Gamma(\nu+1+n) \Gamma(\nu+1-n)}{\Gamma(\nu+1+1/2\ell+1/2) \Gamma(\nu+1-1/2\ell) \Gamma(-n+1/2\ell+1) \Gamma(-n-1/2\ell+1/2)}. \tag{3.10}
\end{aligned}$$

Examination of the rotational wave packet coefficients in Eq. 3.9 reveals the expected Raman selection rules for a symmetric-top molecule excited by an elliptically polarized pulse. The parity for M is always conserved, while the parity of J is conserved only for $K_0 = 0$. For the special case of a circularly polarized pump pulse where $A = 0$, both K and M are conserved. Finally, we note that the above model can be easily adapted for the special case of the interaction between an elliptically polarized pulse and a linear molecule by setting $K_0 = 0$.

While the above model is valid for any polarization state, for the special case of a linearly polarized pump pulse, it is computationally more efficient to choose the coordinate system such that the direction of polarization defines \hat{z} , since the resulting wave packet is azimuthally symmetric about that axis. For this laboratory frame, the interaction Hamiltonian is given by $H_{\text{int}} = -1/4\Delta\alpha|E(t)|^2 \cos^2 \theta$ [4]. The coefficients

for the wave packet can be obtained in the same manner as outlined above, giving

$$c_{JM_0}^{J_0K_0M_0} = (-1)^{K_0+M_0} \sqrt{(2J+1)(2J_0+1)} \sum_{\nu=0}^{\infty} \frac{(iP_{\text{lin}})^{\nu}}{\nu!} \sum_{\ell=\ell_{\text{min}}}^{\text{Min}(J+J_0, 2\nu)} (2\ell+1) \quad (3.11)$$

$$\frac{\sqrt{\pi} 2^{-2\nu-1} \Gamma(1+2\nu)}{\Gamma(1+\nu-1/2\ell)\Gamma(\nu+1/2\ell+3/2)} \begin{pmatrix} J & \ell & J_0 \\ K_0 & 0 & -K_0 \end{pmatrix} \begin{pmatrix} J & \ell & J_0 \\ M_0 & 0 & -M_0 \end{pmatrix},$$

where $P_{\text{lin}} = \frac{\Delta\alpha}{4\hbar} \int_{-\infty}^{\infty} |E(t)|^2 dt$ and ℓ is always even, with $\ell_{\text{min}} = |J - J_0|$ if J and J_0 have the same parity, and $\ell_{\text{min}} = |J - J_0| + 1$ otherwise.

The resulting wave packet for an initial state $|J_0K_0M_0\rangle$ at any later time t is then given as

$$|\psi(t)\rangle = \sum_{J,M} c_{J,M}^{J_0,K_0,M_0} e^{-iE_{JK_0}t/\hbar} |JK_0M\rangle. \quad (3.12)$$

The vibration-rotation coupling arising from Coriolis and centrifugal forces prevents the wave packet from exactly reforming at its revival times. However, rotational recurrences can nevertheless be observed over long time scales (see [59] for a more detailed discussion).

Assuming an initially Boltzmann distributed ensemble, the resulting orientational probability distribution is found by averaging over all initially populated states, including the appropriate nuclear statistical weights, giving

$$G(\theta, \phi, t) = \sum_{J_0=0}^{\infty} \sum_{K_0=-J_0}^{J_0} W(J_0, K_0) \sum_{M_0=-J_0}^{J_0} |\langle \phi, \theta, \chi | \psi(t) \rangle|^2, \quad (3.13)$$

where $W(J_0, K_0)$ is a normalized weighting function. One may separate the spatial and temporal dependence of the rotational wave packet with an expansion in terms of spherical harmonics

$$G(\theta, \phi, t) = \sum_{L=0}^{\infty} \sum_{m=-L}^L b_L^m(t) Y_L^m(\theta, \phi). \quad (3.14)$$

The resultant $b_L^m(t)$ -coefficients are ensemble averages of expectation values of the spherical harmonics. As such, these coefficients measure expectation values of combinations of trigonometric operators. For example, the most commonly used measure for molecular alignment with respect to \hat{z} , $\langle\langle \cos^2 \theta(t) \rangle\rangle$, is given by $\langle\langle \cos^2 \theta(t) \rangle\rangle = 4/3\sqrt{\pi/5} b_2^0(t) + 1/3$.

3.2.1.2 Results for the orientational probability distribution

Rotational wave packets for symmetric top and linear molecules were computed by evaluating the wave packet coefficients for each initial rotational eigenstate given by Eq. 3.9 and the $b_L^m(t)$ -coefficients defined by Eq. 3.14. The case of linear CO₂ molecules at a temperature of 50 K is given in Fig. 3.1. Pump pulses with circular [$A = 0$, Fig. 3.1(a)], elliptic [$A = 0.5$, Fig. 3.1(b)], and linear [$A = 1$, Fig. 3.1(c)] polarization, a 20-fs pulse duration, and a peak intensity of $3 \cdot 10^{14}$ W/cm² with a corresponding kick strength of $P = 6.7$ are considered. To the right of each panel, the orientational probability density constructed from the computed b-coefficients is shown at $\tau = 10.6$ ps, indicated by a circle for each case. The contribution of H_{CD} , i.e. vibration-rotation coupling, is about six orders of magnitude lower than H_o [63]. Hence, for the parameters chosen in this calculation, it is negligible. Note that the usual quarter, half, three-quarter, and full revivals are observed in $b_2^0(t)$ (blue curve) while $b_4^0(t)$ (red) and $b_6^0(t)$ (black) exhibit higher-order fractional revivals.

The orientational probability densities in Fig. 3.1 clearly show that in the chosen laboratory frame where \hat{z} is coincident with the direction of propagation, the wave packet is only azimuthally symmetric for a circularly polarized pump pulse, indicating the expected alignment along the direction of propagation for circular polarization[4]. For any other polarization state, azimuthal symmetry is lost, i.e. the M-quantum number is no longer conserved. However, as noted above, for a linearly polarized laser pulse, an appropriate choice of coordinate frame for the interaction will eliminate M-

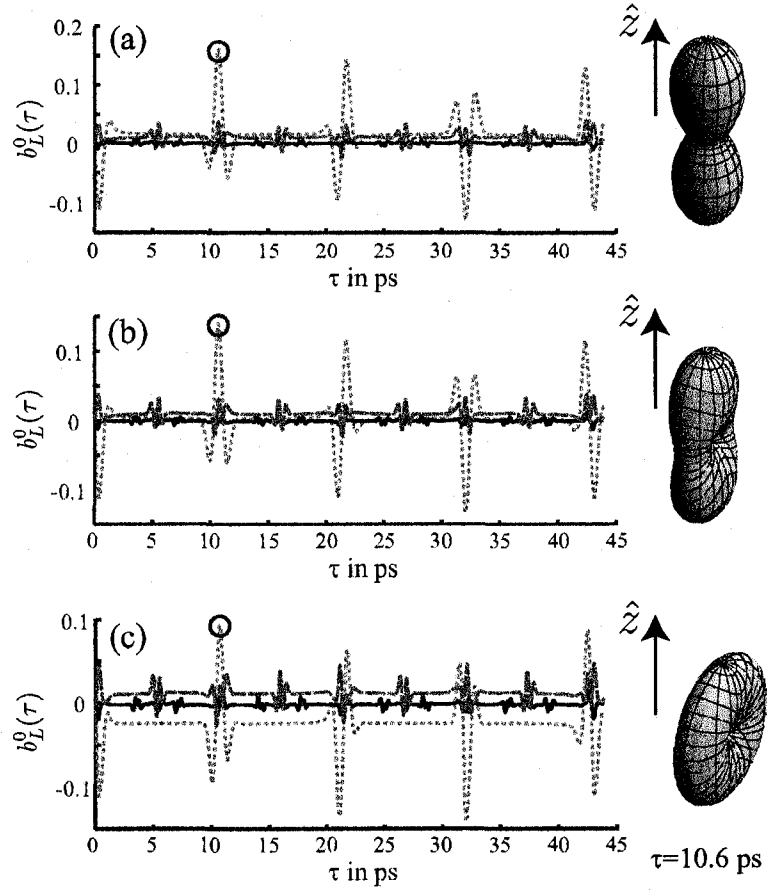


Figure 3.1: b_L^0 -coefficients for $L=2$ (blue), $L=4$ (red), and $L=6$ (black) for circularly (a), elliptically (b), and linearly (c) polarized pump pulses with a peak intensity of $3 \cdot 10^{14}$ W/cm², a pulse duration of 20 fs, and a gas temperature of 50 K. The pump pulse propagates along \hat{z} . The orientational probability distribution corresponding to the respective pump pulse polarization is shown to the right of each panel at the peak of the quarter revival at $\tau = 10.6$ ps.

level couplings since the rotational wave packet is azimuthally symmetric about the direction of the pulse polarization. The strength of the coupling between different M-levels is directly proportional to the ellipticity A of the pump pulse, as can be seen from Eq. 3.9.

More recently, the attention for aligning and orienting molecules has shifted towards more complicated symmetric as well as asymmetric top molecules. Rotational Coherence Spectroscopy (RCS) as well as techniques derived from RCS have been used for the purpose of gaining information regarding the structure of the molecules, and even molecular clusters [53, 12]. We chose methyl iodide (CH_3I) to perform a calculation of rotational wave packet excitation in a symmetric-top molecule since field-free rotational revivals of CH_3I have recently been measured experimentally [59]. For our calculation, the polarizability anisotropy is taken to be 13.4 (a.u.) [64] and the rotational constants are $A_o = 5.1734\text{cm}^{-1}$ and $B_o = 0.2502156\text{cm}^{-1}$ [65]. The centrifugal distortion constants are $D_J = 6.307543\text{kHz}$, $D_{JK} = 98.7688\text{kHz}$, and $D_K = 2689.14\text{kHz}$ [66]. The nuclear statistical weights have been taken from Wilson et al. [67].

The results of a calculation of the rotational wave packet induced in CH_3I held at 10 K by a linearly polarized pump pulse with a kick strength of $P_{\text{in}} = 10.26$ (peak intensity of $2 \cdot 10^{14}\text{ W/cm}^2$ and a pulse duration of 20 fs) are shown in Fig. 3.2 (a). The frame is chosen such that the polarization direction defines \hat{z} . Due to the spin statistics of the molecule, the quarter revival, which is the first prominent rotational revival feature in a rotational wave packet in CO_2 , is absent in CH_3I . The effect of centrifugal distortion due to the non-rigidity of CH_3I molecules is illustrated in Fig. 3.2 (b) with a comparison between the first (dashed, red) and the 30th (solid, blue) full revival. Our calculation is consistent with previous observations [59].

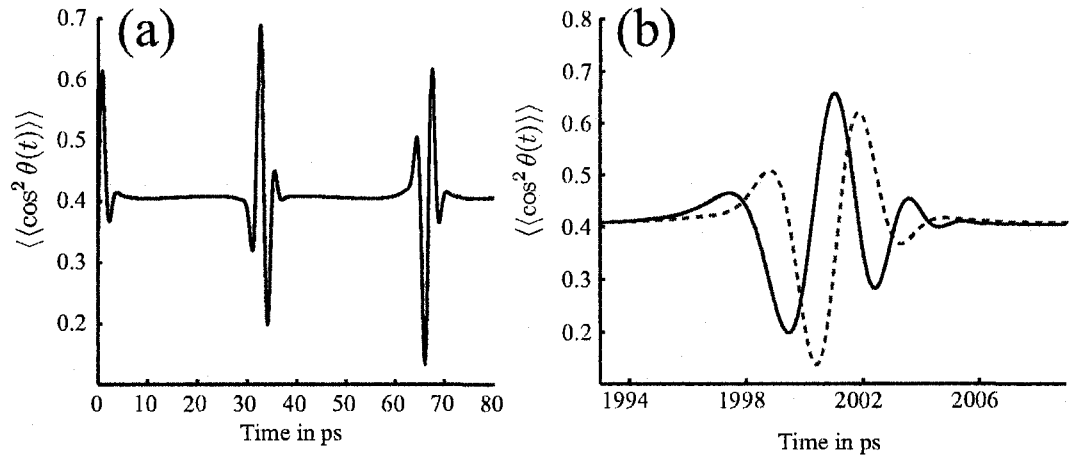


Figure 3.2: (a) Alignment of CH_3I at $T=10$ K for a linearly polarized pulse resulting in $P_{\text{lin}} = 10.26$. (b) Effect due to centrifugal distortion on the full revival of the rotational wave packet comparing the first (dashed, red) to the 30th (blue, solid) full revival.

3.2.1.3 Accuracy of impulsive approximation

Of central importance with any theoretical model is the range of parameters over which the model produces a reliable result. Since this model assumes excitation of the wave packet due to a field approximated by a delta-function, describing the resulting wave packet for any finite pulse duration will necessarily result in an error. In order to determine the range of parameters over which the model we present is valid, we have developed a detailed comparison of the analytic model with a numeric solution of the Schrödinger equation. We restrict our discussion to the case of a linearly polarized Gaussian alignment pulse with the \hat{z} direction in the laboratory frame coinciding with the polarization direction.

Numeric solution of Schrödinger Equation Starting with the Schrödinger equation:

$$i\hbar \frac{\partial |\psi(t)\rangle}{\partial t} = H |\psi(t)\rangle$$

with $H = H_o + H_{\text{int}}$, where centrifugal distortion has been neglected since it is expected to contribute negligibly to the error for short time intervals after $t = 0$. Again,

defining $|\psi(t)\rangle \equiv U_o|\psi_I(t)\rangle$, where U_o is the time evolution operator for the system in the absence of an electromagnetic field and substituting this into the Schrödinger equation,

$$i\hbar \frac{\partial U_o|\psi_I(t)\rangle}{\partial t} = (H_o + H_{\text{int}})U_o|\psi_I(t)\rangle \quad (3.15)$$

Carrying out the derivative on the left hand side,

$$\begin{aligned} i\hbar \left(-\frac{i}{\hbar}\right) H_o U_o|\psi_I(t)\rangle + i\hbar U_o \frac{\partial |\psi_I(t)\rangle}{\partial t} &= (H_o + H_{\text{int}})U_o|\psi_I(t)\rangle \\ i\hbar U_o \frac{\partial |\psi_I(t)\rangle}{\partial t} &= H_{\text{int}}U_o|\psi_I(t)\rangle \end{aligned}$$

and using $U^\dagger U = 1$ results in

$$i\hbar \frac{\partial |\psi_I(t)\rangle}{\partial t} = U_o^\dagger H_{\text{int}} U_o |\psi_I(t)\rangle. \quad (3.16)$$

Next, we express $|\psi_I(t)\rangle$ as a superposition of the normalized, symmetric top eigenstates of the Hamiltonian, $|JKM\rangle$,

$$|\psi_I(t)\rangle = \sum_{JKM} c_{JKM}^{J_o K_o M_o}(t) |JKM\rangle,$$

and insert this into Eq.3.16, which results in

$$i\hbar \sum_{JKM} \frac{\partial c_{JKM}^{J_o K_o M_o}(t)}{\partial t} |JKM\rangle = \sum_{JKM} c_{JKM}^{J_o K_o M_o} U_o^\dagger H_{\text{int}} U_o |JKM\rangle. \quad (3.17)$$

Using the orthonormality of the $|JKM\rangle$'s,

$$i\hbar \frac{\partial c_{J'K'M'}^{J_o K_o M_o}}{\partial t} = \sum_{JKM} c_{JKM}^{J_o K_o M_o}(t) \langle J'K'M' | e^{\frac{i}{\hbar} H_o t} H_{\text{int}} e^{-\frac{i}{\hbar} H_o t} |JKM\rangle \quad (3.18)$$

and rewriting the right hand side results in

$$i\hbar \frac{\partial c_{J'K'M'}^{J_o K_o M_o}}{\partial t} = \sum_{JKM} c_{JKM}^{J_o K_o M_o}(t) e^{\frac{i}{\hbar} E_{J'K'} t} e^{-\frac{i}{\hbar} E_{JK} t} \langle J'K'M' | H_{\text{int}} | JK M \rangle$$

For a field which is linearly polarized along \hat{z} , H_{int} is given by

$$H_{\text{int}} = -\frac{1}{4} \Delta\alpha |E(t)|^2 \cos^2 \theta,$$

where $\Delta\alpha$ is the polarizability anisotropy of the molecule and $E(t)$ is the complex, slowly varying envelope of the pulse. Then,

$$\frac{\partial c_{J'K'M'}^{J_o K_o M_o}}{\partial t} = \frac{i\Delta\alpha}{4\hbar} |E(t)|^2 \sum_{JKM} c_{JKM}^{J_o K_o M_o}(t) e^{\frac{i}{\hbar} (E_{J'K'} - E_{JK}) t} \langle J'K'M' | \cos^2 \theta | JK M \rangle.$$

With

$$\cos^2 \theta = \frac{2}{3} D_{0,0}^2(\phi, \theta, \chi) + \frac{1}{3}$$

the equation for the wave packet coefficients can be expressed as

$$\begin{aligned} \frac{\partial c_{J'K'M'}^{J_o K_o M_o}}{\partial t} &= \frac{i\Delta\alpha}{4\hbar} |E(t)|^2 \sum_{JKM} c_{JKM}^{J_o K_o M_o}(t) e^{\frac{i}{\hbar} (E_{J'K'} - E_{JK}) t} \langle J'K'M' | \frac{2}{3} D_{0,0}^2(\phi, \theta, \chi) + \frac{1}{3} | JK M \rangle \\ \frac{\partial c_{J'K'M'}^{J_o K_o M_o}}{\partial t} &= \frac{i\Delta\alpha}{4\hbar} |E(t)|^2 \sum_{JKM} c_{JKM}^{J_o K_o M_o}(t) e^{\frac{i}{\hbar} (E_{J'K'} - E_{JK}) t} \left(\frac{2}{3} \langle J'K'M' | D_{0,0}^2(\phi, \theta, \chi) | JK M \rangle \right. \\ &\quad \left. + \frac{1}{3} \langle J'K'M' | JK M \rangle \right). \end{aligned}$$

The normalized symmetric top eigenfunctions are given by

$$\langle \phi, \theta, \chi | JK M \rangle = \sqrt{\frac{2J+1}{8\pi^2}} D_{KM}^{J*}(\phi, \theta, \chi).$$

The integral over the three Wigner rotation matrices is non-zero only for $J = J' \pm 1$ and $J = J' \pm 2$. K and M are both conserved. With the result for the integral given

in terms of Wigner-3j symbols,

$$\begin{aligned}
\frac{\partial c_{J'K'M'}^{J_0K_0M_0}}{\partial t} &= \frac{i\Delta\alpha}{4\hbar} |E(t)|^2 \left[c_{J'K'M'}^{J_0K_0M_0}(t) \left(\frac{1}{3} + \frac{2}{3}(2J+1)(-1)^{K'+M'} \right) \right. \\
&\times \begin{pmatrix} J' & 2 & J' \\ K' & 0 & -K' \end{pmatrix} \begin{pmatrix} J' & 2 & J' \\ M' & 0 & -M' \end{pmatrix} \\
&+ \frac{2}{3} c_{J'\pm 1K'M'}^{J_0K_0M_0} e^{i/\hbar(E_{J'K'} - E_{J'\pm 1K'})t} \sqrt{(2J'+1)(2(J'\pm 1)+1)} (-1)^{K'+M'} \\
&\begin{pmatrix} J' & 2 & J'\pm 1 \\ K' & 0 & -K' \end{pmatrix} \begin{pmatrix} J' & 2 & J'\pm 1 \\ M' & 0 & -M' \end{pmatrix} \\
&+ \frac{2}{3} c_{J'\pm 2K'M'}^{J_0K_0M_0} e^{i/\hbar(E_{J'K'} - E_{J'\pm 2K'})t} \sqrt{(2J'+1)(2(J'\pm 2)+1)} (-1)^{K'+M'} \\
&\left. \begin{pmatrix} J' & 2 & J'\pm 2 \\ K' & 0 & -K' \end{pmatrix} \begin{pmatrix} J' & 2 & J'\pm 2 \\ M' & 0 & -M' \end{pmatrix} \right]
\end{aligned}$$

Defining

$$\begin{aligned}
A &= \frac{1}{3} + \frac{2}{3}(2J+1)(-1)^{K'+M'} \begin{pmatrix} J' & 2 & J' \\ K' & 0 & -K' \end{pmatrix} \begin{pmatrix} J' & 2 & J' \\ M' & 0 & -M' \end{pmatrix} \\
B^\pm &= \frac{2}{3} e^{i/\hbar(E_{J'K'} - E_{J'\pm 1K'})t} \sqrt{(2J'+1)(2(J'\pm 1)+1)} (-1)^{K'+M'} \\
&\begin{pmatrix} J' & 2 & J'\pm 1 \\ K' & 0 & -K' \end{pmatrix} \begin{pmatrix} J' & 2 & J'\pm 1 \\ M' & 0 & -M' \end{pmatrix} \\
C^\pm &= \frac{2}{3} e^{i/\hbar(E_{J'K'} - E_{J'\pm 2K'})t} \sqrt{(2J'+1)(2(J'\pm 2)+1)} (-1)^{K'+M'} \\
&\begin{pmatrix} J' & 2 & J'\pm 2 \\ K' & 0 & -K' \end{pmatrix} \begin{pmatrix} J' & 2 & J'\pm 2 \\ M' & 0 & -M' \end{pmatrix}
\end{aligned}$$

we have for the expansion coefficients of the wave function

$$\frac{\partial c_{J'K'M'}^{J_0K_0M_0}}{\partial t} = \frac{i\Delta\alpha}{4\hbar} |E(t)|^2 \left[c_{J'K'M'}^{J_0K_0M_0}(t)A + c_{J'\pm 1K'M'}^{J_0K_0M_0}(t)B^\pm + c_{J'\pm 2K'M'}^{J_0K_0M_0}(t)C^\pm \right]$$

This set of coupled equations is solved numerically using the Runge-Kutta-Fehlberg algorithm of fourth order with error estimation implemented in MATLAB (ode45).

Comparison of analytic to numeric solution For purposes of comparison, we consider $\langle\langle\cos^2\theta(\tau)\rangle\rangle$, the most commonly measured observable in field-free rotational wave packet experiments. The relative error between the cosine squared expectation value computed with the numerical, $\langle\langle\cos^2\theta(\tau)\rangle\rangle_n$, and analytic, $\langle\langle\cos^2\theta(\tau)\rangle\rangle_a$, models defined as $\epsilon_{\langle\langle\cos^2\theta(\tau)\rangle\rangle} \equiv \{ \langle\langle\cos^2\theta(\tau)\rangle\rangle_n - \langle\langle\cos^2\theta(\tau)\rangle\rangle_a \} / \langle\langle\cos^2\theta(\tau)\rangle\rangle_a$ is computed in order to assess the accuracy of the analytic model.

Examination of the higher order terms neglected in making the impulsive approximation shows that the error in the wave packet coefficients given in Eq. 3.9 and its contribution to $\epsilon_{\langle\langle\cos^2\theta(\tau)\rangle\rangle}$ depends on the initial state $|J_0K_0M_0\rangle$, as well as the peak intensity of the pulse and the pulse duration[29]. We have found that for a fixed kick strength, the error in $\langle\langle\cos^2\theta(\tau)\rangle\rangle$ increases with pulse duration — approximately doubling the error when the pulse duration is doubled and peak pulse intensity is correspondingly halved to keep the kick strength constant. This behavior is shown in Fig. 3.3(a) where we examine the relative error for a fixed kick strength of $P = 5.13$. Here a linearly polarized alignment pulse with pulse durations ranging from 10 fs to 80 fs and corresponding peak intensities of $4 \cdot 10^{14} \text{W/cm}^2$ to $2.5 \cdot 10^{13} \text{W/cm}^2$ for CH_3I at a rotational temperature of 5 K is considered. Each Case shown corresponds to a kick strength of $P_{\text{lin}} = 5.13$. The maximum relative error occurs for a pulse duration of about 80 fs, and is below 0.5%.

Fig. 3.3(b) compares how the error in $\langle\langle\cos^2\theta(\tau)\rangle\rangle$ increases when the kick strength is doubled either by doubling the pulse intensity, while leaving the pulse duration constant (Case I), and vice versa (Case II). The relative error in $\langle\langle\cos^2\theta(\tau)\rangle\rangle$ for $P_{\text{lin}} = 2.56$, with $I_o = 2 \cdot 10^{14} \text{W/cm}^2$ and $\tau = 5$ fs (blue), is compared to that for $P_{\text{lin}} = 5.13$. The pulse parameters for Case I are $I_o = 4 \cdot 10^{14} \text{W/cm}^2$, $\tau = 5$ fs (black),

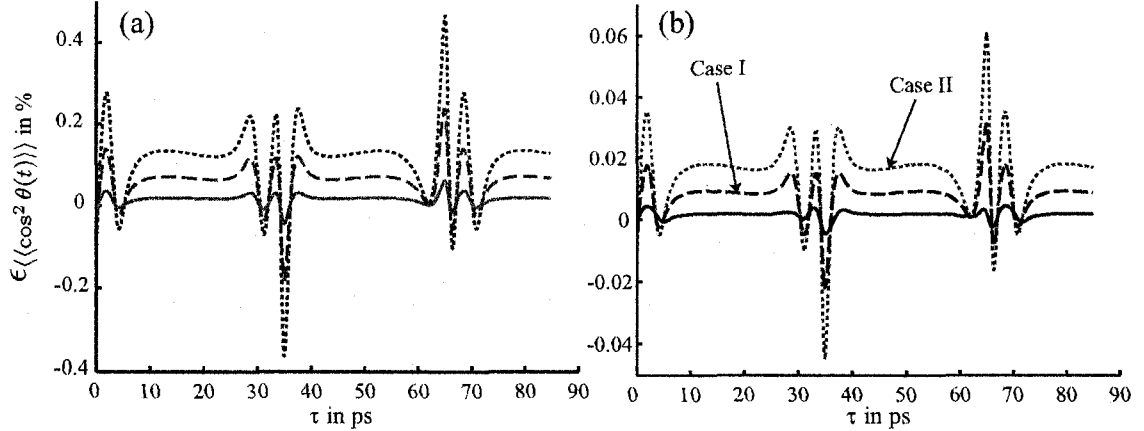


Figure 3.3: (a) Comparison of relative error in $\langle\langle\cos^2\theta(\tau)\rangle\rangle$ for three different combinations of pulse intensity and duration, each resulting in a kick strength of $P_{\text{lin}} = 5.13$: $I_o = 2.5 \cdot 10^{13}\text{W/cm}^2$ and $\tau = 80$ fs (blue), $I_o = 5 \cdot 10^{13}\text{W/cm}^2$ and $\tau = 40$ fs (red), $I_o = 2 \cdot 10^{14}\text{W/cm}^2$ and $\tau = 10$ fs (green). Clearly, the relative error increases with pulse duration for a fixed kick strength. (b) The relative error for $P_{\text{lin}} = 2.56$ ($I_o = 2 \cdot 10^{14}\text{W/cm}^2$, $\tau = 5$ fs, blue) compared to $P_{\text{lin}} = 5.13$. Case I: $I_o = 4 \cdot 10^{14}\text{W/cm}^2$, $\tau = 5$ fs (black); Case II: $I_o = 2 \cdot 10^{14}\text{W/cm}^2$, $\tau = 10$ fs (red). The loss in accuracy is higher for longer pulse durations, rather than higher pulse intensities.

and $I_o = 2 \cdot 10^{14}\text{W/cm}^2$, $\tau = 10$ fs (red) for Case II. While the error increases in both cases, the increase for Case II is larger by a factor of two as compared to the increase for Case I. The model is, therefore, more error prone for longer pulses, rather than more intense ones. However, both higher intensity and pulse duration will result in loss of accuracy.

In calculating $\epsilon_{\langle\langle\cos^2\theta(\tau)\rangle\rangle}$ for a kickstrength of $P = 24$, which corresponds to a peak intensity of $I_o = 3.1 \cdot 10^{14}\text{W/cm}^2$ and a pump pulse duration of $\tau = 30$ fs, we found that the maximum deviation from the numeric solution is about 6%. While this error might still be tolerable, pulses of this strength will tend to ionize and possibly dissociate many molecules. The model does not take these effects into account. In experimental investigations of rotational wave packets the pulse exciting the wave packet is typically limited in energy as to leave the molecules under investigation largely intact[4].

3.3 Effective susceptibilities due to coherent nuclear motion

For pulse propagation in the presence of a nuclear wave packet, may that be coherent rotational, vibrational, or ro-vibrational motion, Eq. 2.10 can be used to find the resulting field after propagation. The effects of the wave packet on the pulse propagation may be taken into account via additional terms in the non-linear contribution to the induced dipole moment density, $\vec{P}_{NL}(\vec{r}, t)$. The nature of that wave packet contribution is that of a delayed Raman response of the medium. The nuclear motion due to a rotational wave packet has been calculated in Sec. 3.2 and expressions for the resulting effective linear and third order susceptibilities are derived in Sec. 3.3.1. The additional term for $\vec{P}(\vec{r}, t)$ is given by

$$\vec{P}_{DR}(\vec{r}, t) = \epsilon_o \chi_{\text{eff}}^{(1)}(t) \vec{E}(\vec{r}, t) + \epsilon_o \chi_{\text{eff}}^{(3)}(t) : \vec{E}(\vec{r}, t) \vec{E}(\vec{r}, t) \vec{E}(\vec{r}, t)$$

Of note here is the fact that the non-linear Raman response $\chi_{\text{eff}}^{(3)}(\tau)$ may be interpreted as off-resonant non-linear Raman scattering, or hyper Raman scattering. More precisely, in this case the scattering cross section is proportional to the second hyper-polarizabilities of the gas, and hence, that term is referred to as second hyper-Raman scattering. There is no term proportional to the hyper-polarizability of the gas for two reasons: The excitation of the rotational wave packet is due to impulsive stimulated Raman scattering, hence, proportional to the polarizability. Due to the selection rules governing the Raman and non-linear Raman modes, any Raman active mode will be second hyper-Raman active. However, there is no coupling between Raman and hyper-Raman modes, which is the reason for the nil contribution to the non-linear optical response in centro-symmetric media. The effect of second-hyper Raman scattering is a modulation of the conversion efficiency to the third harmonic. This is true for rotational as well as vibrational wave packets which has

been shown experimentally. Expressions for the effective susceptibilities have already been derived in the weak pump approximation within the framework of the BOA. The model presented for the analytic solution of the Schrödinger equation allows us to find analytic expressions for the effective susceptibilities in the presence of a rotational wave packet for strong pump pulses with the limitation of little to no dissociation of the molecules, of course. This will be shown in the next section.

3.3.1 Effective linear susceptibility tensor for rotations using the analytic model

The polarizability tensor of a symmetric-top molecule in its principle frame can be written as

$$\bar{\alpha} = \begin{pmatrix} \alpha_{\perp} & 0 & 0 \\ 0 & \alpha_{\perp} & 0 \\ 0 & 0 & \alpha_{\parallel} \end{pmatrix}.$$

The polarizability tensor in the lab frame is found via an Euler transformation

$$\chi_{ij}^{(1)} \equiv \langle \chi_{IJ}^{(1),avg} \rangle_{ij} = \frac{N}{\epsilon_o} \int \int_{4\pi} \alpha_{ij} G(\phi, \theta, t) d\Omega, \quad (3.19)$$

where $\alpha(\phi, \theta, \psi)_{ij}$ is the molecular polarizability tensor component along the ij direction with the molecular frame coordinates given as IJ and the lab coordinate given as ij .

The direction cosines can be obtained directly from the matrix that transforms the molecule from the laboratory frame to an arbitrary orientation specified in coordinates ϕ, θ, ψ . To illustrate, normally, the Euler matrix is constructed as a transformation from a laboratory coordinate system x, y, z to a specific orientation labelled by primed coordinates x''', y''', z''' . The ordering of the transformations matters. Usually, the first

rotation is about the z axis in the lab frame by a positive angle ϕ with a rotation matrix defined by

$$R_\phi = \begin{pmatrix} \cos(\phi) & \sin(\phi) & 0 \\ -\sin(\phi) & \cos(\phi) & 0 \\ 0 & 0 & 1 \end{pmatrix}, \quad (3.20)$$

and arrive at the primed coordinates. Next, we rotate about the x' -axis through the polar angle θ with the transformation

$$R_\theta = \begin{pmatrix} 1 & 0 & 0 \\ 0 & \cos(\theta) & \sin(\theta) \\ 0 & -\sin(\theta) & \cos(\theta) \end{pmatrix}, \quad (3.21)$$

and arrive at the double primed coordinates. Finally, we rotate about z'' axis through the angle ψ with the transformation

$$R_\psi = \begin{pmatrix} \cos(\psi) & \sin(\psi) & 0 \\ -\sin(\psi) & \cos(\psi) & 0 \\ 0 & 0 & 1 \end{pmatrix}, \quad (3.22)$$

arriving at the arbitrarily oriented molecular frame. The overall matrix that projects a molecular from the lab frame onto the molecular frame is given by $R = R_\psi R_\theta R_\phi$.

The matrix for transformation from the lab to the molecular frame is given by

$$R = \begin{pmatrix} \cos(\psi) \cos(\phi) - \sin(\phi) \sin(\psi) \cos(\theta) & \cos(\psi) \sin(\phi) + \sin(\psi) \cos(\phi) \cos(\theta) & \sin(\psi) \sin(\theta) \\ -\cos(\phi) \sin(\psi) - \sin(\phi) \cos(\psi) \cos(\theta) & -\sin(\phi) \sin(\psi) + \cos(\phi) \cos(\psi) \cos(\theta) & \cos(\psi) \sin(\theta) \\ \sin(\phi) \sin(\theta) & -\cos(\phi) \sin(\theta) & \cos(\theta) \end{pmatrix}, \quad (3.23)$$

whereas the matrix for transformation from the molecule to the lab frame is given by

$$R^{-1} = \begin{pmatrix} \cos(\psi) \cos(\phi) - \sin(\phi) \sin(\psi) \cos(\theta) & -\cos(\phi) \sin(\psi) - \sin(\phi) \cos(\psi) \cos(\theta) & \sin(\phi) \sin(\theta) \\ \cos(\psi) \sin(\phi) + \sin(\psi) \cos(\phi) \cos(\theta) & -\sin(\phi) \sin(\psi) + \cos(\phi) \cos(\psi) \cos(\theta) & -\cos(\phi) \sin(\theta) \\ \sin(\psi) \sin(\theta) & \cos(\psi) \sin(\theta) & \cos(\theta) \end{pmatrix}. \quad (3.24)$$

The projection of the polarizability tensor from the molecular frame to the the lab frame is thus given by

$$\bar{\alpha}_{\text{lab}} = R^{-1}\bar{\alpha}R$$

or equivalently

$$\alpha_{ij}(\phi, \theta, \psi) = \sum_{IJ} r_{iI}r_{jJ}\alpha_{IJ},$$

where $r_{\alpha\beta}$ are the direction cosines obtained from the matrix R (e.g., for z, z we have r_{33} , or for x, Y , we have r_{12} , etc.), i, j are the lab coordinates and I, J are the molecular frame coordinates.

As a first step we will determine the transformation matrix for a single linear molecule, then perform the orientational averaging based on the orientational probability distribution. First, we note that for linear molecules, the angle ψ is irrelevant. We can look at all of the products of direction cosines involved in the orientational averaging that forms the averaged linear tensor by specifically evaluating the matrix product $R^{-1}\bar{\alpha}R$, which is given by

$$\bar{\alpha} = \begin{pmatrix} \alpha_{\perp} + [1 - \cos^2(\theta)] \Delta\alpha - \cos^2(\phi) [1 - \cos^2(\theta)] \Delta\alpha & \frac{1}{2} \sin(2\phi) \sin^2(\theta) \Delta\alpha & \frac{1}{2} \sin(\phi) \sin(2\theta) \Delta\alpha \\ \frac{1}{2} \sin(2\phi) \sin^2(\theta) \Delta\alpha & \alpha_{\perp} + \cos^2(\phi) [1 - \cos^2(\theta)] \Delta\alpha & \frac{1}{2} \cos(\phi) \sin(2\theta) \Delta\alpha \\ \frac{1}{2} \sin(\phi) \sin(2\theta) \Delta\alpha & \frac{1}{2} \cos(\phi) \sin(2\theta) \Delta\alpha & \alpha_{\perp} + \Delta\alpha \cos^2(\theta) \end{pmatrix}. \quad (3.25)$$

The polarization density induced by a weak, off-resonant time-delayed probe pulse $E_{\text{pr}}(t)$ may be written as $P(t) = E_{\text{pr}}(t)N\text{Tr}[\alpha\rho(t)]$ [29], where α is an element of the polarizability tensor. Here $\rho(t)$ is the density matrix operator of the molecular ensemble after the impulsive interaction with the pump pulse which can be found using the analytic model and N is the number of molecules in the gas. The Cartesian indices have been suppressed for clarity. From this definition, one readily obtains the effective linear, time-dependent susceptibility as $\chi_{\text{eff}}(t) = \frac{N}{\epsilon_0}\text{Tr}[\alpha\rho(t)]$.

Using the analytical model for the rotational wave packet, the effective linear

susceptibility can be rewritten as

$$\chi_{\text{eff}}(t) = \frac{N}{\epsilon_o} \iint \alpha(\phi, \theta) \sum_{J_0 K_0} W(J_0, K_0) \sum_{M_0} \psi_{K_0 M_0}^{J_0*}(\phi, \theta, \chi, t) \psi_{K_0 M_0}^{J_0}(\phi, \theta, \chi, t) d\Omega \quad (3.26)$$

where $\alpha(\phi, \theta)$ represents the molecular polarizability at an arbitrary Euler angle in the laboratory frame. Noting the orientational probability distribution given in Eq. 3.13 appears in the integral and applying the expansion given in Eq. 3.14, we obtain the expression

$$\chi_{\text{eff}}(t) = \frac{N}{\epsilon_o} \sum_{L=0}^{\infty} \sum_{m=-L}^L b_L^m(t) \iint \alpha(\phi, \theta) Y_L^m(\theta, \phi) d\Omega. \quad (3.27)$$

Clearly, the effective linear susceptibility is interpreted as an orientational average weighted by the rotational wave packet prepared by the pump pulse.

The expansion of the orientational probability distribution in terms of spherical harmonics permits an evaluation of the transient susceptibility tensor structure independently of any specific rotational wave packet. Evaluating the spatial integral in Eq. 3.27, the various tensor elements of the effective susceptibility given an elliptically polarized pump pulse exciting a purely rotational coherence is readily obtained. Due to the selection rules of the Raman interaction of the pump pulse and the molecules, and the fact that the density operator is hermitian, all off-diagonal elements of the polarizability tensor are zero in the laboratory frame defined by the pulse in Eq. 3.4. The diagonal tensor elements are given as

$$\chi_{xx}(t) = \frac{N}{\epsilon_o} \left\{ \bar{\alpha} - \frac{2}{3} \sqrt{\frac{\pi}{5}} \Delta\alpha \left[b_2^0(t) - \sqrt{6} b_2^2(t) \right] \right\},$$

$$\chi_{yy}(t) = \frac{N}{\epsilon_o} \left\{ \bar{\alpha} - \frac{2}{3} \sqrt{\frac{\pi}{5}} \Delta\alpha \left[b_2^0(t) + \sqrt{6} b_2^2(t) \right] \right\},$$

and

$$\chi_{zz}(t) = \frac{N}{\epsilon_o} \left\{ \bar{\alpha} + \frac{4}{3} \sqrt{\frac{\pi}{5}} \Delta\alpha b_2^0(t) \right\},$$

where $\bar{\alpha} = \frac{1}{3}\alpha_{\parallel} + \frac{2}{3}\alpha_{\perp}$ is the isotropic average of the molecular polarizability tensor. An analytic expression for the b-coefficients, and hence, for the effective susceptibility, can be readily found using Eq. 3.9 in combination with Eq. 3.13 and Eq. 3.14.

When no pump pulse is present, all b-coefficients are identically zero and effective linear susceptibility tensor reduces to the expected isotropic value $\chi = N/\epsilon_o\bar{\alpha}$. The result above demonstrates that the transient susceptibility tensor is bi-axial for an elliptically-polarized pump pulse and uniaxial for a circularly or linearly polarized pump pulse. Furthermore, the sign of the b-coefficients dictates whether the susceptibility tensor behaves as positive or negative uniaxial for linear and circularly polarized pump pulses. As can be seen in Fig. 3.1, the tensor switches between positive and negative uniaxial during each rotational revival. This explains why two types of Type II phase matching are possible for third harmonic generation in symmetric top (and therefore also linear) molecules aligned by linearly polarized laser pulses[15].

3.3.2 The transient non linear susceptibility for rotations using the analytic model

Excitation of a rotational wave packet in a gas of anisotropic molecules by means of an ultrashort laser pulse not only results in a time dependent effective linear optical response, but also a time dependent non-linear response of the gas. In the following, the third order non-linear response, i.e., the second-hyper polarizability tensor, is analyzed in detail. For higher order non-linearities the result follows analogously. The hyper polarizability tensor of a symmetric-top molecule like CH_3I , or that of a linear molecule like CO_2 has 21 non-zero elements, where only three elements are independent: $\gamma_{XXXX}, \gamma_{XZZZ}, \gamma_{ZZZZ}$. The tensor in the lab frame is again obtained

from the principal molecular frame via an Euler transformation, analogous to the polarizability tensor, and is given by

$$\begin{aligned}\langle\langle\gamma_{ijkl}\rangle\rangle &= \gamma_{IJKL} \int r_{iI}r_{jJ}r_{kK}r_{lL}G(\theta, \phi, t)d\Omega \\ \langle\langle\gamma_{ijkl}\rangle\rangle &= \int \langle\gamma_{ijkl}\rangle G(\theta, \phi, t)d\Omega\end{aligned}$$

where $G(\theta, \phi, t)$ is the orientational probability distribution of the molecules, time dependent due to the excitation of the rotational wave packet. The elements of the hyper polarizability tensor, in the lab frame, are given by:

$$\begin{aligned}\gamma_{xxxx} &= \frac{1}{8} [3(\gamma_{XXXX} - 6\gamma_{XXZZ} + \gamma_{ZZZZ}) \cos^4(\theta) \\ &\quad + 2(\gamma_{XXXX} + 6\gamma_{XXZZ} - 3\gamma_{ZZZZ}) \cos^2(\theta) + 3(\gamma_{XXXX} + 2\gamma_{XXZZ} + \gamma_{ZZZZ})] \\ \gamma_{zzzz} &= (\gamma_{XXXX} - 6\gamma_{XXZZ} + \gamma_{ZZZZ}) \cos^4(\theta) - 2(\gamma_{XXXX} - 3\gamma_{XXZZ}) \cos^2(\theta) + \gamma_{XXXX} \\ \gamma_{xxzz} &= \frac{1}{2}(-\gamma_{XXXX} + 6\gamma_{XXZZ} - \gamma_{ZZZZ}) \cos^4(\theta) \\ &\quad + \frac{1}{6}(2\gamma_{XXXX} + 3(\gamma_{ZZZZ} - 5\gamma_{XXZZ})) \cos^2(\theta) + \frac{1}{6}(\gamma_{XXXX} + 3\gamma_{XXZZ})\end{aligned}$$

The third order susceptibility tensor for a dilute gas, i.e., the molecules are assumed non-interacting, is then given as

$$\chi_{ijkl}^{(3)} = \frac{N}{\epsilon_0} \langle\langle\gamma_{ijkl}\rangle\rangle,$$

where the double brackets indicate thermal averaging assuming an initial population according to the Boltzmann distribution. With

$$G(\theta, \phi, t) = \sum_{L,m} b_L^m(t) Y(\theta, \phi),$$

the third order susceptibility tensor elements can be written as

$$\begin{aligned}
\chi_{ijkl}^{(3)} &= \frac{N}{\epsilon_o} \int \langle \gamma_{ijkl} \rangle G(\theta, \phi, t) d\Omega \\
&= \frac{N}{\epsilon_o} \sum_{L,m} b_L^m(t) \int \langle \gamma_{ijkl} \rangle Y_L^m(\theta, \phi) d\Omega \\
&= \frac{N}{\epsilon_o} \sum_{L,m} b_L^m(t) \int (\delta_{ijkl}^{(0)} + \delta_{ijkl}^{(1)} \cos^2 \theta + \delta_{ijkl}^{(2)} \cos^4 \theta) Y_L^m(\theta, \phi) d\Omega \\
&= \frac{N}{\epsilon_o} \sum_{L,m} b_L^m(t) \left(\delta_{ijkl}^{(0)} \int Y_L^m(\theta, \phi) d\Omega + \delta_{ijkl}^{(1)} \int \cos^2 \theta Y_L^m(\theta, \phi) d\Omega + \delta_{ijkl}^{(2)} \int \cos^4 \theta Y_L^m(\theta, \phi) d\Omega \right)
\end{aligned}$$

The integrals have analytic solutions:

$$\begin{aligned}
\chi_{ijkl}^{(3)} &= \frac{N}{\epsilon_o} \sum_{L,m} b_L^m(t) \left\{ \delta_{ijkl}^{(0)} \delta_{L,0} \delta_{m,0} \sqrt{4\pi} + \delta_{ijkl}^{(1)} \left(\delta_{L,0} \delta_{m,0} \frac{\sqrt{4\pi}}{3} + \delta_{L,2} \delta_{m,0} \frac{4}{3} \sqrt{\frac{\pi}{5}} \right) \right. \\
&\quad \left. + \delta_{ijkl}^{(2)} \left(\delta_{L,0} \delta_{m,0} \frac{2\sqrt{\pi}}{5} + \delta_{L,2} \delta_{m,0} \frac{8}{7} \sqrt{\frac{\pi}{5}} + \delta_{L,4} \delta_{m,0} \frac{16}{105} \sqrt{\pi} \right) \right\} \\
&= \frac{N}{\epsilon_o} \left(\delta_{ijkl}^{(0)} b_0^0(t) \sqrt{4\pi} + \delta_{ijkl}^{(1)} \left(b_0^0(t) \frac{\sqrt{4\pi}}{3} + b_2^0(t) \frac{4}{3} \sqrt{\frac{\pi}{5}} \right) \right. \\
&\quad \left. + \delta_{ijkl}^{(2)} \left(b_0^0(t) \frac{2\sqrt{\pi}}{5} + b_2^0(t) \frac{8}{7} \sqrt{\frac{\pi}{5}} + b_4^0(t) \frac{16}{105} \sqrt{\pi} \right) \right)
\end{aligned}$$

With $b_0^0(t) = 1/\sqrt{4\pi}$,

$$\begin{aligned}
\chi_{ijkl}^{(3)} &= \frac{N}{\epsilon_o} \left\{ \delta_{ijkl}^{(0)} + \delta_{ijkl}^{(1)} \left(\frac{1}{3} + b_2^0(t) \frac{4}{3} \sqrt{\frac{\pi}{5}} \right) + \delta_{ijkl}^{(2)} \left(\frac{1}{5} + b_2^0(t) \frac{8}{7} \sqrt{\frac{\pi}{5}} + b_4^0(t) \frac{16}{105} \sqrt{\pi} \right) \right\} \\
&= \frac{N}{\epsilon_o} \left(\delta_{ijkl}^{(0)} + \frac{\delta_{ijkl}^{(1)}}{3} + \frac{\delta_{ijkl}^{(2)}}{5} + \delta_{ijkl}^{(1)} b_2^0(t) \frac{4}{3} \sqrt{\frac{\pi}{5}} + \delta_{ijkl}^{(2)} b_2^0(t) \frac{8}{7} \sqrt{\frac{\pi}{5}} + \delta_{ijkl}^{(2)} b_4^0(t) \frac{16}{105} \sqrt{\pi} \right) \\
&= \frac{N}{\epsilon_o} \left(\delta_{ijkl}^{(0)} + \frac{\delta_{ijkl}^{(1)}}{3} + \frac{\delta_{ijkl}^{(2)}}{5} + b_2^0(t) \sqrt{\frac{\pi}{5}} \left(\delta_{ijkl}^{(1)} \frac{4}{3} + \delta_{ijkl}^{(2)} \frac{8}{7} \right) + b_4^0(t) \delta_{ijkl}^{(2)} \frac{16}{105} \sqrt{\pi} \right) \\
&= \frac{N}{\epsilon_o} \left(\chi_{iso}^{(3)} + b_2^0(t) \sqrt{\frac{\pi}{5}} \left(\delta_{ijkl}^{(1)} \frac{4}{3} + \delta_{ijkl}^{(2)} \frac{8}{7} \right) + b_4^0(t) \delta_{ijkl}^{(2)} \frac{16}{105} \sqrt{\pi} \right)
\end{aligned}$$

The various δ -coefficients are given by:

XXXX:

$$\delta_{xxxx}^{(0)} = \frac{1}{8} (3\gamma_{xxxx} + 6\gamma_{xxzz} + 3\gamma_{zzzz})$$

$$\delta_{xxxx}^{(1)} = \frac{1}{8} (2\gamma_{xxxx} + 12\gamma_{xxzz} - 6\gamma_{zzzz})$$

$$\delta_{xxxx}^{(2)} = \frac{1}{8} (3\gamma_{xxxx} - 18\gamma_{xxzz} + 3\gamma_{zzzz})$$

XXZZ:

$$\delta_{xxzz}^{(0)} = \frac{1}{6} (\gamma_{xxxx} + 3\gamma_{xxzz})$$

$$\delta_{xxzz}^{(1)} = \frac{1}{6} (2\gamma_{xxxx} - 15\gamma_{xxzz} + 3\gamma_{zzzz})$$

$$\delta_{xxzz}^{(2)} = \frac{1}{6} (-3\gamma_{xxxx} + 18\gamma_{xxzz} - 3\gamma_{zzzz})$$

ZZZZ:

$$\delta_{zzzz}^{(0)} = \gamma_{xxxx}$$

$$\delta_{zzzz}^{(1)} = 6\gamma_{xxzz} - 2\gamma_{xxxx}$$

$$\delta_{zzzz}^{(2)} = \gamma_{xxxx} - 6\gamma_{xxzz} + \gamma_{zzzz}$$

So, the time dependent third order susceptibility depends on the expectations values of $\cos^2 \theta$ and $\cos^4 \theta$. For higher-order interactions this means that the higher order non-linear response of the gas will depend on higher-order moments of the wave packet. This fact has been shown, for example, in the high harmonic signal obtained from an aligned ensemble of molecules. Fractional revivals of higher order, i.e., eight- and sixteenth revivals, have been observed from a variety of gases this way. More information can therefore be obtained about the quantum wave packet from higher-order non-linear interactions between a probe field and the aligned ensemble.

3.4 Laser Pulse Propagation in the presence of coherent nuclear motion

A very typical method of detecting coherent nuclear motion (CNM) is to observe its effect on a weak probe pulse after the pump pulse. The probe pulse is usually weak so it can be assumed that its non-linear interaction with the molecules is negligible, i.e., it doesn't appreciably affect the CNM excited by the strong pump pulse, nor does it excite CNM to any measurable degree. The probe field resulting after propagation may be modeled utilizing the above expressions for the effective susceptibilities. The probe field after propagation will differ in a variety of ways from a field propagated through a gas in thermal equilibrium. For example, as has been shown in Sec. 3.3.1, a gas is birefringent during the revival times of a rotational wave packet. This birefringence, of course, affects the propagation of a probe pulse which is linearly polarized at some angle with respect to the pump pulse. The change in the polarization state of the probe pulse may then be observed in a polarization gating method, which is exactly the way rotational wave packets were observed for the first time[45]. There are a variety of additional propagation effects which follow simply from considering the impact of a time-varying induced polarization density in the propagation equation.

To derive a propagation equation suitable for this purpose, we will start with Eq. 2.8, which is given as

$$\begin{aligned} (-k_x^2 - k_y^2 + \frac{\partial^2}{\partial z^2})\vec{\mathbf{E}}(k_x, k_y, z, \omega) + \frac{\omega^2}{c^2}\bar{\bar{\epsilon}}_r(\omega) : \vec{\mathbf{E}}(k_x, k_y, z, \omega) = \\ - \frac{i\omega}{c^2\epsilon_0}\vec{\mathbf{J}}(k_x, k_y, z, \omega) - \frac{\omega^2}{c^2\epsilon_0}\vec{\mathbf{P}}_{NL}(k_x, k_y, z, \omega). \end{aligned}$$

In order to simplify the derivation, we will assume plane wave propagation, as is given over the interaction length for example in a capillary, or for weakly focussed pulses where one can assume quasi-plane wave propagation over a short distance at

the focus. This results in an easier to follow derivation, while the nature of the propagation effects due to the CNM is not affected by this assumption at all. We will also assume that there is no ionization present, i.e., $\vec{\mathbf{J}}(\vec{\mathbf{r}}, t) = 0$. While the pump pulse will certainly ionize the molecules at its focus, the impact of the phase shift due to the space charge present at the focus is independent of pump-probe delay due to the comparatively long recombination time of the plasma. For the case of propagation in a capillary most of the propagation distance of the probe pulse in the presence of CNM will be in the absence of any plasma. This will simplify Eq. 2.8 to

$$\frac{\partial^2 \vec{\mathbf{E}}(z, \omega)}{\partial z^2} + \frac{\omega^2}{c^2} \bar{\epsilon}_r(\omega) : \vec{\mathbf{E}}(z, \omega) = -\frac{\omega^2}{c^2 \epsilon_o} \vec{\mathbf{P}}_{NL}(z, \omega),$$

which shall be the starting point of this derivation. We define

$$\bar{k}^2(\omega) = \frac{\omega^2}{c^2} \bar{\epsilon}_r(\omega)$$

and the field in terms of a rapidly oscillating phase and a slowly varying, complex envelope,

$$\vec{\mathbf{E}}(z, t) = \frac{1}{2} \left(\vec{\mathbf{A}}(z, t) e^{-i\omega_o t + ik_o z} + c.c. \right),$$

where ω_o and k_o are the central frequency and wave vector of the pulse, respectively. In the frequency domain the spectrum is then given by

$$\vec{\mathbf{E}}(z, \omega) = \frac{1}{2} \left(\vec{\mathbf{A}}(z, \omega - \omega_o) e^{ik_o z} + c.c. \right).$$

The propagation equation can be written in terms of an envelope equation as

$$\frac{\partial^2}{\partial z^2} \vec{\mathbf{A}}(z, \omega - \omega_o) e^{ik_o z} + \bar{k}^2(\omega) : \vec{\mathbf{A}}(z, \omega - \omega_o) e^{ik_o z} = -\frac{\omega^2}{c^2 \epsilon_o} \vec{\mathbf{P}}_{NL}(z, \omega),$$

The same equation holds for the complex conjugate part of the field. It is under-

stood that the real part of the solution to the propagation equation should be taken.

Carrying out the derivative with respect to z ,

$$\begin{aligned} \left(\frac{\partial^2 \vec{\mathbf{A}}(z, \omega - \omega_o)}{\partial z^2} + i2k_o \frac{\partial \vec{\mathbf{A}}(z, \omega - \omega_o)}{\partial z} \right) e^{ik_o z} + \left(\bar{k}^2(\omega) - k_o^2 \right) : \vec{\mathbf{A}}(z, \omega - \omega_o) e^{ik_o z} \\ = -\frac{\omega^2}{c^2 \epsilon_o} \vec{\mathbf{P}}_{NL}(z, \omega), \end{aligned}$$

Making the slowly varying envelope approximation, the propagation equation used to analyze the effects of a time-varying susceptibility on the propagation of a weak probe pulse is finally given by

$$i2k_o \frac{\partial \vec{\mathbf{A}}(z, \omega - \omega_o)}{\partial z} + \left[\bar{k}^2(\omega) - k_o^2 \right] : \vec{\mathbf{A}}(z, \omega - \omega_o) = -\frac{\omega^2}{c^2 \epsilon_o} \vec{\mathbf{P}}_{NL}(z, \omega) e^{-ik_o z} \quad (3.28)$$

The next step is to transform the resulting equation back into the time domain, since the time dependence of the effective susceptibilities is the origin of these additional propagation effects not present in a gas at thermal equilibrium. Therefore, the time domain lends itself to a more intuitive interpretation of the additional terms in the induced polarization density. However, the dispersion of the gas is more naturally taken into account in the frequency domain. For that reason a split step algorithm[21] will be employed for the implementation of this model which takes dispersion into account in the frequency domain, but the non-linear terms due to the effective time-varying susceptibility in the time domain. We will also move into the group frame of the probe pulse, and in order to arrive at an equation which lends itself to this procedure, we first expand the magnitude of the wave vector in terms of a power series centered at $\omega - \omega_o$ [33]:

$$\bar{k}(\omega) = \bar{k}(\omega_o) + k_1(\omega - \omega_o) + D,$$

where $D = \sum_{n=2}^{\infty} \frac{1}{n!} k_n (\omega - \omega_o)^n$ and $k_n = \frac{\partial^n \bar{k}(\omega)}{\partial \omega^n} |_{\omega_o}$. The first derivative of $k(\omega)$ is

singled out due to its physical interpretation of the inverse group velocity of the pulse.

With this,

$$\bar{k}^2(\omega) = \bar{k}^2(\omega_o) + 2\bar{k}(\omega_o)k_1(\omega - \omega_o) + 2\bar{k}^2(\omega_o)D + 2k_1D + k_1^2(\omega - \omega_o)^2 + D^2,$$

where $k_o \equiv \bar{k}(\omega_o)$. When transforming back into the time domain, the dispersion will be left in the frequency domain, due to the split step approach chosen for solving the equation, except for the term including the inverse group velocity, $2k_o k_1(\omega - \omega_o)$.

Now, Eq. 3.28 reads in the time domain, with $k_1 \equiv \frac{1}{v_g}$,

$$i2k_o \frac{\partial \vec{\mathbf{A}}(z, t)}{\partial z} e^{-i\omega_o t} + i2k_o \frac{1}{v_g} \frac{\partial \vec{\mathbf{A}}(z, t)}{\partial t} e^{-i\omega_o t} = \frac{1}{c^2 \epsilon_o} \frac{\partial^2 \vec{\mathbf{P}}_{NL}(z, t)}{\partial t^2} e^{-ik_o z} \quad (3.29)$$

and finally

$$\frac{\partial \vec{\mathbf{A}}(z, t)}{\partial z} + \frac{1}{v_g} \frac{\partial \vec{\mathbf{A}}(z, t)}{\partial t} = -\frac{i}{2c^2 k_o \epsilon_o} \frac{\partial^2 \vec{\mathbf{P}}_{NL}(z, t)}{\partial t^2} e^{-ik_o z + i\omega_o t} \quad (3.30)$$

Converting to the group frame of the probe pulse, we need to switch to a coordinate frame such that

$$\zeta = z$$

and

$$\tau = t - \frac{1}{v_g} z$$

which results in

$$\frac{\partial \vec{\mathbf{A}}(\zeta, \tau)}{\partial \zeta} = -\frac{i}{2c^2 k_o \epsilon_o} \frac{\partial^2 \vec{\mathbf{P}}_{NL}(\zeta, \tau)}{\partial \tau^2} e^{-ik_o \zeta + i\omega_o \tau} \quad (3.31)$$

Since we are making the assumption of an off-resonance interaction, and using the effective susceptibility to express the effect of the CNM on the induced polarization

density, the non-linear induced polarization density can be written as

$$\vec{\mathbf{P}}_{NL}(z, t) = \epsilon_o \bar{\chi}^{(1)}(t) : \vec{\mathbf{E}}(z, t) + \epsilon_o \bar{\chi}^{(3)}(t) : \vec{\mathbf{E}}(z, t) \vec{\mathbf{E}}(z, t) \vec{\mathbf{E}}(z, t). \quad (3.32)$$

This expression is valid for both coherent vibrational and rotational motion. The propagation effects due to any CNM can now be identified by transforming Eq. 3.32 into the group frame of the probe pulse and inserting the result into Eq. 3.31. In the following we will analyze the resulting effects of CNM on a weak probe pulse and treat the impact of the effective linear separately first. Then, the combined effects due to the effective linear and non-linear susceptibility will be analyzed.

3.4.1 Propagation effects due to $\bar{\chi}^{(1)}(t)$

If the probe pulse is weak, there will be no non-linear propagation effects due to the probe pulse, i.e., the contributions due to the effective third order susceptibility may be neglected. Then,

$$\vec{\mathbf{P}}_{NL}(z, t) = \epsilon_o \bar{\chi}^{(1)}(t) : \vec{\mathbf{E}}(z, t),$$

which reads in the rest frame of the probe pulse

$$\vec{\mathbf{P}}_{NL}(\zeta, \tau) = \epsilon_o \bar{\chi}^{(1)}(\tau - \tau_{PD}) : \vec{\mathbf{E}}(\zeta, \tau),$$

assuming that the rest frames of the pump and probe pulses are identical, i.e., both pump and probe pulses are centered at the same frequency. τ_{PD} is the delay of the probe pulse with respect to the pump pulse.

The vector notation for the field, as well as the tensor notation for the effective linear susceptibility, is carried on with the fact in mind that the gas is birefringent during rotational revivals, and may also show anisotropy for certain vibrational modes. This way it is possible to treat the propagation effects due to the CNM more generally,

with a probe field that can be of arbitrarily polarization propagating in an anisotropic medium. To simplify the notation somewhat, we will, however, write out the product of the effective linear susceptibility and the field in terms of its components, which is given by

$$\bar{\chi}^{(1)}(\tau - \tau_{PD}) : \vec{\mathbf{A}}(\zeta, \tau) = \chi_{ij}^{(1)}(\tau - \tau_{PD}) A_j(\zeta, \tau).$$

Then, by explicitly writing out the terms obtained from taking the partial derivative with respect to time of the induced polarization density we obtain the following:

$$\begin{aligned} \frac{\partial^2}{\partial \tau^2} \left\{ \chi_{ij}^{(1)}(\tau - \tau_{PD}) A_j(\zeta, \tau) e^{-i\omega_o \tau} \right\} = & \left(\chi_{ij}^{(1)}(\tau - \tau_{PD}) \frac{\partial^2 A_j(\zeta, \tau)}{\partial \tau^2} + 2 \frac{\partial \chi_{ij}^{(1)}(\tau - \tau_{PD})}{\partial t} \frac{\partial A_j(\zeta, \tau)}{\partial \tau} \right. \\ & - i 2 \omega_o \chi_{ij}^{(1)}(\tau - \tau_{PD}) \frac{\partial A_j(\zeta, \tau)}{\partial \tau} - i 2 \omega_o \frac{\partial \chi_{ij}^{(1)}(\tau - \tau_{PD})}{\partial \tau} A_j(\zeta, \tau) \\ & \left. + \frac{\partial^2 \chi_{ij}^{(1)}(\tau - \tau_{PD})}{\partial \tau^2} A_j(\zeta, \tau) - \omega_o^2 \chi_{ij}^{(1)}(\tau - \tau_{PD}) A_j(\zeta, \tau) \right) \\ & e^{-i\omega_o \tau}. \end{aligned}$$

Plugging this back into the propagation equation, we find that each component of the field is now given by

$$\begin{aligned} \frac{\partial A_i(\zeta, \tau)}{\partial \zeta} = & \frac{i}{2c^2 k_o} \chi_{ij}^{(1)}(\tau - \tau_{PD}) \frac{\partial^2 A_j(\zeta, \tau)}{\partial \tau^2} + \frac{i}{c^2 k_o} \frac{\partial \chi_{ij}^{(1)}(\tau - \tau_{PD})}{\partial \tau} \frac{\partial A_j(\zeta, \tau)}{\partial \tau} \\ & + \frac{\omega_o}{c^2 k_o} \chi_{ij}^{(1)}(\tau - \tau_{PD}) \frac{\partial A_j(\zeta, \tau)}{\partial \tau} + \frac{\omega_o}{c^2 k_o} \frac{\partial \chi_{ij}^{(1)}(\tau - \tau_{PD})}{\partial t} A_j(\zeta, \tau) \\ & + \frac{i}{2c^2 k_o} \frac{\partial^2 \chi_{ij}^{(1)}(\tau - \tau_{PD})}{\partial \tau^2} A_j(\zeta, \tau) - \frac{i\omega_o^2}{2c^2 k_o} \chi_{ij}^{(1)}(\tau - \tau_{PD}) A_j(\zeta, \tau) \quad (3.33) \end{aligned}$$

Among the six driving terms on the right hand side there are three terms which have an immediate intuitive physical interpretation. These three terms and their physical

interpretations are:

$$\begin{aligned}
\frac{i\omega_o^2}{2c^2k_o}\chi_{ij}^{(1)}(\tau - \tau_{PD})A_j(\zeta, \tau) &: \text{Temporal phase modulation} \\
\frac{\omega_o}{c^2k_o}\chi_{ij}^{(1)}(\tau - \tau_{PD})\frac{\partial A_j(\zeta, \tau)}{\partial \tau} &: \text{Group Velocity Modification} \\
\frac{\omega_o}{c^2k_o}\frac{\partial \chi_{ij}^{(1)}(\tau - \tau_{PD})}{\partial \tau}A_j(\zeta, \tau) &: \text{Energy conservation}
\end{aligned}$$

Temporal phase modulation will modify the spectrum of the pulse and leave the temporal envelope unchanged. If the phase modulation is weak, as would be the case for example for very short propagation lengths or very low gas pressures, the phase shift due to CNM can be measured using standard interferometry techniques and may be interpreted as an additional, time varying contribution to the index of refraction[34]. The different regimes in terms of the strength of the phase modulation and its effects on the pulse will be discussed in detail in Sec.5.4. A variety of techniques have been developed over time in order to measure the transient index of refraction due to coherent rotational motion, originally referred to as 'susceptibility echoes'[2, 68, 69, 70]. A single-shot technique which allows the measurement of the time dependence of the index of refraction for a rotational wave packet excited by an arbitrarily polarized pump pulse will be detailed in Sec. 5.2. A comprehensive review on the subject of rotational wave packets is [4].

Group Velocity Modification due to CNM has not been exploited up till now. It has been shown in this work that there is a change in the propagation time of a weak probe pulse due to a rotational wave packet of up to 20 fs, which is about half the duration of the pulse at FWHM.

3.4.2 Propagation effects due to $\bar{\chi}^{(3)}(t)$

Similarly, the effects on the propagation of a probe pulse may be analyzed for the non-linear effective susceptibilities. In this section, only the third order effective susceptibility is developed. The analysis follows analogously to that in Sec. 3.4.1. However, since the contribution is of third order in the field, many more terms appear in the induced polarization density. The only contribution by $\chi^{(3)}(t)$, however, which will be analyzed in detail is that which gives rise to a modulation of the third order susceptibility of the medium. It is expected that this term can be directly observed as a modulation of conversion efficiency to the third harmonic of the probe field. The non-linear induced polarization density will now include the effective linear, as well as third order, susceptibility, keeping in mind that the effective linear susceptibility describes scattering processes of third order in the field, and the effective third order susceptibility describes scattering processes of fifth order in the field. The field is now separated into two distinct spectral envelopes, one centered around the fundamental frequency, and the other centered around the third harmonic, so that

$$\vec{\mathbf{E}}(z, t) = \frac{1}{2} \left(\vec{\mathbf{A}}_1(z, t)e^{-i\omega_0 t + ik_0 z} + \vec{\mathbf{A}}_3(z, t)e^{-i\omega_0 t + ik_3 z} + c.c. \right).$$

With the polarization density given by

$$\vec{\mathbf{P}}_{NL}(z, t) = \epsilon_0 \bar{\chi}^{(1)}(t) : \vec{\mathbf{E}}(z, t) + \epsilon_0 \bar{\chi}^{(3)}(t) : \vec{\mathbf{E}}(z, t)\vec{\mathbf{E}}(z, t)\vec{\mathbf{E}}(z, t)$$

it is obvious that a large number of terms contributing to $\vec{\mathbf{P}}_{NL}(z, t)$ results. We will take only terms into account which oscillate at the fundamental and third harmonic frequencies, since terms oscillating at higher harmonics, originating for example from cascaded third order effects between the fundamental field and the third harmonic field, will contribute negligibly. Then, at the fundamental frequency we have self phase

modulation (SPM), cross phase modulation (XPM), and back conversion, while at the third harmonic the resulting terms describe SPM, XPM and THG. Explicitly, the i^{th} component of $\vec{\mathbf{P}}_{NL}(z, t)$ is given by

$$P_{i,NL}(z, t) = \epsilon_o \chi_{ij}^{(1)}(t) E_j(z, t) + \epsilon_o \chi_{ijkl}^{(3)}(t) E_j(z, t) E_k(z, t) E_l(z, t).$$

Expressing the field in terms of the complex envelopes and separating out the fast oscillating phase terms,

$$\begin{aligned} P_{i,NL}(z, t) &= \epsilon_o \chi_{ij}^{(1)}(t) (A_{1,j}(z, t) e^{-i\omega_o t + ik_o z} + A_{3,j}(z, t) e^{-i\omega_3 t + ik_3 z}) \\ &+ \frac{\epsilon_o \chi_{ijkl}^{(3)}(t)}{8} (A_{1,jkl}(z, t) e^{-i\omega_o t + ik_o z} + A_{3,jkl}(z, t) e^{-i\omega_3 t + ik_3 z}). \end{aligned}$$

where

$$A_{1,jkl}(z, t) = 3A_{1,j}(z, t)A_{1,k}^*(z, t)A_{1,l}(z, t) + 6A_{3,j}(z, t)A_{3,k}^*(z, t)A_{1,l}(z, t) + 3A_{1,j}^*(z, t)A_{1,k}^*(z, t)A_{3,l}(z, t) e^{-i\Delta k z}$$

$$A_{3,jkl}(z, t) = 3A_{3,j}(z, t)A_{3,k}^*(z, t)A_{3,l}(z, t) + 6A_{1,j}(z, t)A_{1,k}^*(z, t)A_{3,l}(z, t) + A_{1,j}(z, t)A_{1,k}(z, t)A_{1,l}(z, t) e^{i\Delta k z}$$

with the phase mismatch defined as $\Delta k = 3k_o - k_3$. Carrying out the same steps as in Sec. 3.4.1 in order to identify explicitly the effects due to the time varying effective third order susceptibility, we can separate the propagation equation into two coupled equations for the fundamental and third harmonic, respectively. For the fundamental,

$$\begin{aligned} \frac{\partial A_{1,i}(\zeta, \tau)}{\partial \zeta} &= \frac{i}{2c^2 k_o} \chi_{ij}^{(1)}(\tau - \tau_{PD}) \frac{\partial^2 A_{1,j}(\zeta, \tau)}{\partial \tau^2} + \frac{i}{c^2 k_o} \frac{\partial \chi_{ij}^{(1)}(\tau - \tau_{PD})}{\partial \tau} \frac{\partial A_{1,j}(\zeta, \tau)}{\partial \tau} \\ &+ \frac{\omega_o}{c^2 k_o} \chi_{ij}^{(1)}(\tau - \tau_{PD}) \frac{\partial A_{1,j}(\zeta, \tau)}{\partial \tau} + \frac{\omega_o}{c^2 k_o} \frac{\partial \chi_{ij}^{(1)}(\tau - \tau_{PD})}{\partial t} A_{1,j}(\zeta, \tau) \\ &+ \frac{i}{2c^2 k_o} \frac{\partial^2 \chi_{ij}^{(1)}(\tau - \tau_{PD})}{\partial \tau^2} A_{1,j}(\zeta, \tau) - \frac{i\omega_o^2}{2c^2 k_o} \chi_{ij}^{(1)}(\tau - \tau_{PD}) A_{1,j}(\zeta, \tau) \\ &+ \frac{i}{8c^2 k_o} \chi_{ijkl}^{(3)}(\tau - \tau_{PD}) \frac{\partial^2 A_{1,jkl}(\zeta, \tau)}{\partial \tau^2} + \frac{i}{4c^2 k_o} \frac{\partial \chi_{ijkl}^{(3)}(\tau - \tau_{PD})}{\partial \tau} \frac{\partial A_{1,jkl}(\zeta, \tau)}{\partial \tau} \\ &+ \frac{\omega_o}{4c^2 k_o} \chi_{ijkl}^{(3)}(\tau - \tau_{PD}) \frac{\partial A_{1,jkl}(\zeta, \tau)}{\partial \tau} + \frac{\omega_o}{4c^2 k_o} \frac{\partial \chi_{ijkl}^{(3)}(\tau - \tau_{PD})}{\partial t} A_{1,jkl}(\zeta, \tau) \\ &+ \frac{i}{8c^2 k_o} \frac{\partial^2 \chi_{ijkl}^{(3)}(\tau - \tau_{PD})}{\partial \tau^2} A_{1,jkl}(\zeta, \tau) - \frac{i\omega_o^2}{8c^2 k_o} \chi_{ijkl}^{(3)}(\tau - \tau_{PD}) A_{1,jkl}(\zeta, \tau) \end{aligned}$$

and for the third harmonic the propagation equation is

$$\begin{aligned}
\frac{\partial A_{3,i}(\zeta, \tau)}{\partial \zeta} + \Delta v_g \frac{\partial A_{3,i}(z, t)}{\partial \tau} &= \frac{i}{2c^2 k_3} \chi_{ij}^{(1)}(\tau - \tau_{PD}) \frac{\partial^2 A_{3,j}(\zeta, \tau)}{\partial \tau^2} + \frac{i}{c^2 k_3} \frac{\partial \chi_{ij}^{(1)}(\tau - \tau_{PD})}{\partial \tau} \frac{\partial A_{3,j}(\zeta, \tau)}{\partial \tau} \\
&+ \frac{\omega_3}{c^2 k_3} \chi_{ij}^{(1)}(\tau - \tau_{PD}) \frac{\partial A_{3,j}(\zeta, \tau)}{\partial \tau} + \frac{\omega_3}{c^2 k_3} \frac{\partial \chi_{ij}^{(1)}(\tau - \tau_{PD})}{\partial t} A_{3,j}(\zeta, \tau) \\
&+ \frac{i}{2c^2 k_3} \frac{\partial^2 \chi_{ij}^{(1)}(\tau - \tau_{PD})}{\partial \tau^2} A_{3,j}(\zeta, \tau) - \frac{i\omega_3^2}{2c^2 k_3} \chi_{ij}^{(1)}(\tau - \tau_{PD}) A_{3,j}(\zeta, \tau) \\
&+ \frac{i}{8c^2 k_3} \chi_{ijkl}^{(3)}(\tau - \tau_{PD}) \frac{\partial^2 A_{3,jkl}(\zeta, \tau)}{\partial \tau^2} + \frac{i}{4c^2 k_3} \frac{\partial \chi_{ijkl}^{(3)}(\tau - \tau_{PD})}{\partial \tau} \frac{\partial A_{3,jkl}(\zeta, \tau)}{\partial \tau} \\
&+ \frac{\omega_3}{4c^2 k_3} \chi_{ijkl}^{(3)}(\tau - \tau_{PD}) \frac{\partial A_{3,jkl}(\zeta, \tau)}{\partial \tau} + \frac{\omega_3}{4c^2 k_3} \frac{\partial \chi_{ijkl}^{(3)}(\tau - \tau_{PD})}{\partial t} A_{3,jkl}(\zeta, \tau) \\
&+ \frac{i}{8c^2 k_3} \frac{\partial^2 \chi_{ijkl}^{(3)}(\tau - \tau_{PD})}{\partial \tau^2} A_{3,jkl}(\zeta, \tau) - \frac{i\omega_3^2}{8c^2 k_3} \chi_{ijkl}^{(3)}(\tau - \tau_{PD}) A_{3,jkl}(\zeta, \tau)
\end{aligned}$$

where the group velocity mismatch between the fundamental and third harmonic pulses is taken into account through the walk-off $\Delta v_g = \frac{1}{v_{g,1}} - \frac{1}{v_{g,3}}$ between the pulses. Since dispersion is not very strong in a gas, and the interaction lengths are on the order of millimeters, this walk-off will only become significant for very short pulses.

3.4.2.1 Modulation of THG due to CNM

Due to the number of terms contributing to the non-linear induced polarization density it is difficult to determine the effect of every single terms. There is, however, one effect which can be experimentally verified. Due to the time dependence of the effective third order susceptibility the conversion efficiency to the third harmonic is expected to vary in time. This can be seen easily when all the other terms are neglected for clarity and only the SPM, XPM and THG terms are kept in the propagation equation of the third harmonic:

$$\frac{\partial A_{3,i}(\zeta, \tau)}{\partial \zeta} + \Delta v_g \frac{\partial A_{3,i}(z, t)}{\partial \tau} = -\frac{i\omega_3^2}{8c^2 k_3} \chi_{ijkl}^{(3)}(\tau - \tau_{PD}) A_{3,jkl}(\zeta, \tau)$$

From this, one would expect the energy in the third harmonic to vary with pump-probe, and more precisely, to vary as $\chi_{ijkl}^{(3)}(\tau - \tau_{PD})$. For a linearly polarized probe

pulse with its polarization direction parallel or orthogonal to the pump pulse, this is indeed what is observed[71]. However, for any other angle between the pump and probe polarizations there is an interplay between the time dependence of the effective linear susceptibility, which affects the polarization state of the probe field, as well as potentially the phase mismatch. The effect of any birefringence which may be present due to CNM is that in addition to Type I processes allowed in an isotropic medium, there are also Type II processes possible. This situation is analyzed in detail in Sec. 6.1.

Chapter 4

Dynamically structured nonlinearity for Quasi Phase Matching

The time varying effective third order susceptibility has been shown to result in a modulated conversion efficiency to the third harmonic. That modulation is a function of pump-probe delay. In this chapter, a potential application of this modulation is presented. It will be shown how the modulation may be utilized to enhance the overall conversion efficiency after propagation in a capillary filled with a gas of anisotropic molecules. There are several motivations, which in part have been outlined in the introduction already, for improving the conversion efficiency of optical frequency conversion processes in a gaseous medium. In principle, the dispersion of nonlinear optical media limits the conversion of an intense optical field from a fundamental to a harmonic frequency as a result of a phase velocity difference between the fundamental and harmonic fields. Phase matching techniques that equalize the fundamental and harmonic phase velocities are routinely employed to obtain efficient nonlinear optical frequency conversion. Armstrong and coworkers suggested an approach dubbed

quasi phase matching (QPM) that permits efficient nonlinear frequency conversion in the presence of a phase mismatch. The most common QPM technique modulates the nonlinear susceptibility along the direction of propagation of the fields, i.e. a *nonlinear grating* is created [72, 73].

Most QPM techniques that have been implemented are based on a periodic reversal of the nonlinear susceptibility for second-order processes. QPM in second-order nonlinear interactions has been demonstrated with stacks of oriented plates[74, 75, 76], rotationally twinned crystals[77], periodically poled crystal[78, 79], and poled polymers[80]. Alternating layers of 800-nm spin-coated polymer and 300 micron thick glass substrates have also been implemented to form a rectangular third-order nonlinear grating to quasi phase match third harmonic generation[81]. Each of these methods of QPM depend on the formation of a *permanent* spatial modulation of the nonlinear response of a medium. Such a permanent spatial structure of material properties is generally only possible in the solid material phase.

Nonlinear optical interactions occurring in the gas (and liquid) phase present problems for standard phase matching techniques. Unlike in the solid phase, the optical properties of a gas can not be permanently structured. Normally, gases exhibit an isotropic macroscopic optical response, precluding their use for birefringent or quasi phase matching. Despite this fact, interest in employing gases for nonlinear optical processes persists because they can be subjected to much higher intensities and exhibit both a broader transparency range and lower dispersion than solids. Conventional phase matching techniques for the gas phase rely on either focusing[82], resonances[83], or waveguide dispersion[84, 85, 86] and have limited applicability.

Application of QPM to gas-phase nonlinear optical interactions has been inhibited by the lack of a method to spatially structure the nonlinear response of a gas. A set of innovative experiments demonstrated that efficient quasi phase matched frequency conversion was possible in both liquids and gases without imposing a spatial modu-

lation on the *fields* involved in the nonlinear interaction. Levine demonstrated that periodically-patterned metal electrodes along a liquid filled waveguide could produce efficient electric field induced second harmonic generation through QPM[87]. Quasi phase matching of high harmonic generation in gases was demonstrated by modulating the inner diameter of a hollow core fiber, which modulates the intense driving laser pulse with a periodicity of twice the coherence length[88].

Here, we propose a new, fundamentally different approach for quasi phase matching of nonlinear optical processes based on the fact that an effective third order response due to CNM will result in a time dependent modulation of the conversion efficiency to the third harmonic. Specifically, we will consider dynamically structured nonlinear optical response of a molecular gas[1, 6, 13, 5] due to a rotational wave packet. The macroscopic nonlinear optical response of a molecular gas is given by the average of each molecule in the ensemble weighted by the relative molecule alignment probability. Because the nonlinear optical susceptibility for an anisotropic molecule is a non-uniform tensor, the ensemble-averaged macroscopic susceptibility of a collection of gas molecules strongly depends on the relative alignment of all of the molecules. Under conditions of thermal equilibrium, the relative alignment of molecules in a gas is random and exhibits an isotropic relative molecular alignment. We show that by controlling the molecular alignment, we can sculpt the nonlinear optical response of the gas.

In this approach to quasi phase matched nonlinear frequency conversion in the gas phase, we exploit the transient molecular alignment induced by an ultrafast alignment pulse to form a nonlinear susceptibility grating that evolves in time. Controlling the amplitude and pulse front tilt of the alignment pulse along the propagation direction of the fundamental pulse allows for control over the nonlinear susceptibility experienced by the fundamental pulse as it propagates through the coherence. With this spatio-temporal alignment control, we show that it is possible to create a nonlinear grating

in the reference frame of the fundamental pulse propagating along the axis of the grating. Simulations of third harmonic generation (THG) show that efficient nonlinear frequency conversion is possible with dynamic QPM. Although we specifically discuss THG, dynamic QPM is applicable to many nonlinear optical processes in a molecular gas, including four-wave mixing and high harmonic generation.

4.1 Dynamically Structured Nonlinearities with CNM

As a reminder, we will briefly outline the rotational tensor averaging process which is applied to find the macroscopic response of the gas in the presence of a rotational wave packet. The induced polarization density averaged over the molecular ensemble can be written as

$$\mathbf{P} = N \langle \langle \mu_I \rangle \rangle \equiv \bar{\chi} : \mathbf{E}, \quad (4.1)$$

where $\bar{\chi}$ defines the macroscopic susceptibility tensor of the gas, N is the molecular density of the gas, and

$$\mu_I = \alpha_{IJ} E_J + \beta_{IJK} E_J E_K + \gamma_{IJKL} E_J E_K E_L + \dots, \quad (4.2)$$

is the dipole moment induced in each molecule in the gas where E_A is a component of the applied electric field, α_{IJ} is the linear polarizability, β_{IJK} is the hyperpolarizability which contributes to the second-order optical response of the gas, and γ_{IJKL} is the second hyperpolarizability which contributes to the third-order optical response of the gas. The indices (I, J, K, \dots) indicate the principle coordinates in the molecular frame, and summation over repeated indices is implied.

For molecules that possess a center of inversion, β_{IJK} identically vanishes. Moreover, even if a molecule is not centrosymmetric, there will be no coherent macroscopic second-order nonlinear response unless the hyperpolarizability tensor contains rota-

tionally invariant components (i.e. is chiral) or if the molecules are directionally ordered. Molecular orientation, which would constitute directional ordering of the molecules, is only possible if the pump pulse is a half-cycle pulse. This case will be neglected in this analysis. Under these conditions, the lowest order macroscopic coherent nonlinear response in the molecular gas is third-order.

The induced polarization density given in Eq. (4.1) defines the macroscopic third order susceptibility tensor that is attributable to the orientational average of the second hyperpolarizability and is given by

$$\chi_{ijkl}^{(3)} = N \langle \langle \gamma_{IJKL} \rangle \rangle_{ijkl}, \quad (4.3)$$

where the orientational average is defined by

$$\langle \langle \gamma_{IJKL} \rangle \rangle_{ijkl} = \gamma_{IJKL} \int \int_{4\pi} a_{iI} a_{jJ} a_{kK} a_{lL} G(\phi, \theta) d\Omega, \quad (4.4)$$

a_{qQ} are the direction cosines between the molecular and lab frames, and $G(\phi, \theta)$ is the orientational probability density of the ensemble of molecules in the gas [33].

The orientational probability density of the molecular ensemble can be computed with the expression

$$G(\theta, \phi, t) = \sum_{J_0} P(J_0) \sum_{M_0=-J_0}^{J_0} |\psi_{J_0}^{M_0}(\theta, \phi, t)|^2, \quad (4.5)$$

where the orientational probability density is normalized such that the integral is unity and the ensemble of molecules is described as a mixed quantum mechanical state with the wave function of each independent rotational eigenstate given by

$$\psi_{M_0}^{J_0}(\theta, \phi, t) = \sum_J \sum_{M=-J}^J c_{M_0 M}^{J_0 J} Y_J^M(\theta, \phi) e^{iE_J t/\hbar}. \quad (4.6)$$

In order to find the coefficients of the wave function, $c_{M_o}^{J_o J}$, Schrödinger's Equation was solved numerically. The Hamiltonian describing the interaction was simplified by making the rigid rotor approximation for the molecule, and the dipole approximation for the interaction of the field and the molecule. The contribution of each rotational state to the orientational probability density is weighted according to the Boltzman occupational probability, $P_{J_o} = Q^{-1} \exp[-E_{J_o}/kT]$, of each state, where the rotational energies are given by $E_{J_o} = BJ_o(J_o + 1)$ and the partition function is given by $Q = \sum_{J_o} (2J_o + 1) \exp[-E_{J_o}/kT]$.

From Eq. (4.4) and Eq. (4.5) it is clear that both the molecular structure and the orientational probability density influence the macroscopic third-order susceptibility of the molecular gas. Hence, for a specific molecular gas, control over the optical susceptibility requires that one controls the orientational probability density.

We apply the control of the third order susceptibility to the process of third harmonic generation using an ensemble of linear, non-polar molecules. Using the symmetry of the molecules, as well as the degeneracy of the involved frequencies allows for significant simplification of the general tensor. The nonzero elements of the orientationally averaged susceptibility of the aligned ensemble of non-polar linear molecules are given by

$$\begin{aligned} \chi_{zzzz}^{(3),THG} \\ \chi_{xxxx}^{(3),THG} = \chi_{yyyy}^{(3),THG} = 3\chi_{xxyy}^{(3),THG} \\ \chi_{xxyy}^{(3),THG} = \chi_{xyxy}^{(3),THG} = \chi_{xyyx}^{(3),THG} = \chi_{yyxx}^{(3),THG} = \chi_{yxyx}^{(3),THG} = \chi_{yxxy}^{(3),THG} \\ \chi_{zzzz}^{(3),THG} = \chi_{xxzz}^{(3),THG} = \chi_{yyzz}^{(3),THG} = \chi_{yzzz}^{(3),THG} = \chi_{xzzz}^{(3),THG} = \chi_{yzyz}^{(3),THG} \\ \chi_{zzzz}^{(3),THG} = \chi_{zyyz}^{(3),THG} = \chi_{zzzx}^{(3),THG} = \chi_{zzzy}^{(3),THG} = \chi_{zxzx}^{(3),THG} = \chi_{zyzy}^{(3),THG} \end{aligned}$$

The general form of the four independent tensor elements is written as $\chi_{ijkl}^{(3),THG} = \frac{N}{8\epsilon_0} \delta_{ijkl}^0 (\delta_{ijkl}^1 + \delta_{ijkl}^2 \langle \langle \cos^2 \theta \rangle \rangle + \delta_{ijkl}^3 \langle \langle \cos^4 \theta \rangle \rangle)$. The coefficients for the nonzero tensor elements are given by $\delta_{zzzz}^0 = 1$, $\delta_{zzzz}^1 = 3\gamma_{xxyy}$, $\delta_{zzzz}^2 = 3(-2\gamma_{xxyy} + \gamma_{xzzz} + \gamma_{zxzx})$, $\delta_{zzzz}^3 =$

$3\gamma_{xxyy} - 3\gamma_{zzzz} - 3\gamma_{zxzx} + \gamma_{zzzz}$ for $\chi_{zzzz}^{(3),THG}$; by $\delta_{xxxx}^0 = \frac{3}{8}, \delta_{xxxx}^1 = 3\gamma_{xxyy} + \gamma_{zzzz} + \gamma_{zxzx} + \gamma_{zzzz}, \delta_{xxxx}^2 = 2(\gamma_{xxyy} + \gamma_{zzzz} + \gamma_{zxzx} - \gamma_{zzzz}), \delta_{xxxx}^3 = \delta_{zzzz}^3$ for $\chi_{xxxx}^{(3),THG}$; by $\delta_{zzxz}^0 = \frac{1}{2}, \delta_{zzxz}^1 = \gamma_{xxyy} + \gamma_{zzzz}, \delta_{zzxz}^2 = 2\gamma_{xxyy} - 4\gamma_{zzzz} - \gamma_{zxzx} + \gamma_{zzzz}, \delta_{zzxz}^3 = -\delta_{zzzz}^3$ for $\chi_{zzxz}^{(3),THG}$; and by $\delta_{zzzx}^0 = \frac{1}{2}, \delta_{zzzx}^1 = \gamma_{xxyy} + \gamma_{zxzx}, \delta_{zzzx}^2 = 2\gamma_{xxyy} - \gamma_{zzzz} - 4\gamma_{zxzx} + \gamma_{zzzz}, \delta_{zzzx}^3 = -\delta_{zzzz}^3$ for $\chi_{zzzx}^{(3),THG}$. For QPM THG processes, only the $\chi_{zzzz}^{(3),THG}$ and $\chi_{xxxx}^{(3),THG}$ terms are relevant. The non-zero terms $\chi_{zzzz}^{(3),THG}$ and $\chi_{zzxz}^{(3),THG}$ show that Type II birefringent phase matching is possible with transient molecular alignment[15].

In the expression for the THG third-order susceptibility tensor components, the expressions

$$\langle\langle \cos^2\theta(t) \rangle\rangle = \sum_{J_0} P_{J_0} \sum_{M=-J_0}^{J_0} \langle \psi_{J_0,M} | \cos^2\theta | \psi_{J_0,M} \rangle \quad (4.7)$$

and

$$\langle\langle \cos^4\theta(t) \rangle\rangle = \sum_{J_0} P_{J_0} \sum_{M=-J_0}^{J_0} \langle \psi_{J_0,M} | \cos^4\theta | \psi_{J_0,M} \rangle \quad (4.8)$$

arise. The quantity $\langle\langle \cos^2\theta(t) \rangle\rangle$ is a measure of the molecular alignment [1] and $\langle\langle \cos^4\theta(t) \rangle\rangle$ can be simply viewed as a higher-order alignment metric. For a uniform orientational probability density, i.e. $G(\theta, \phi) = 1$, the alignment metrics evaluate to $\langle\langle \cos^2\theta(t) \rangle\rangle = \frac{1}{3}$ and $\langle\langle \cos^4\theta(t) \rangle\rangle = \frac{1}{5}$. Substitution of these values into the expressions for the aligned tensor components recovers the THG tensor for isotropic media. The quantity $\langle\langle \cos^2\theta(t) \rangle\rangle$ lends itself to a simple physical interpretation: $\langle\langle \cos^2\theta(t) \rangle\rangle = 1$ means that the long axis of each molecule in the ensemble points along the direction of the alignment pulse polarization (full alignment), whereas $\langle\langle \cos^2\theta(t) \rangle\rangle = 0$ indicates that the molecules are aligned perpendicular to the alignment polarization (full anti alignment). The transient molecular alignment for a typical linear molecule (e.g., CO_2) is shown in Fig. 4.1, where alignment, τ_I , anti-alignment, τ_{II} , and non-alignment, τ_{III} , are marked.

Because the duration and energy of the ultrafast alignment pulse control the strength of the molecular alignment induced in the gas, we can adjust the properties

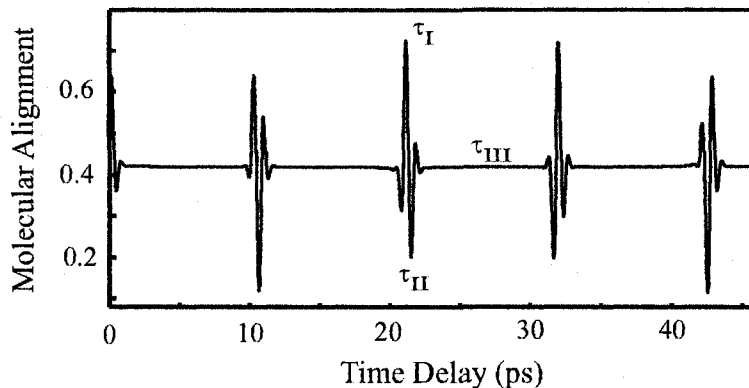


Figure 4.1: Typical molecular alignment vs. time induced in a linear molecule (shown here is the time-scale for CO_2). The figure shows that the alignment of the molecular ensemble is significantly modified only near revival events. The labels τ_I , τ_{II} , and τ_{III} refer to times of molecular alignment, anti-alignment, and non-alignment during the transient molecular alignment.

of the alignment pulse to control the nonlinear optical response of the medium. In the next section, we describe an approach to create transiently structured nonlinear gratings with the spatially controlled molecular alignment.

4.2 Proposed experimental setup

The control over the strength of the nonlinear optical response in a molecular gas discussed in the preceding section can be adapted to permit efficient nonlinear frequency conversion through quasi phase matching. By spatially modulating the molecular alignment, a grating in the strength of the nonlinear susceptibility can be formed. Efficient nonlinear optical frequency conversion occurs when the periodicity of the nonlinear grating is set to twice the coherence length of the nonlinear mixing process. Owing to the transient nature of the molecular alignment, any nonlinear grating formed by this method will evolve with time. Below, we show that with proper spatio-temporal control of the alignment pulse, a time-varying nonlinear grating formed can be used for efficient nonlinear frequency conversion.

A schematic of the transiently aligned molecule QPM concept is shown in Fig. 4.2.

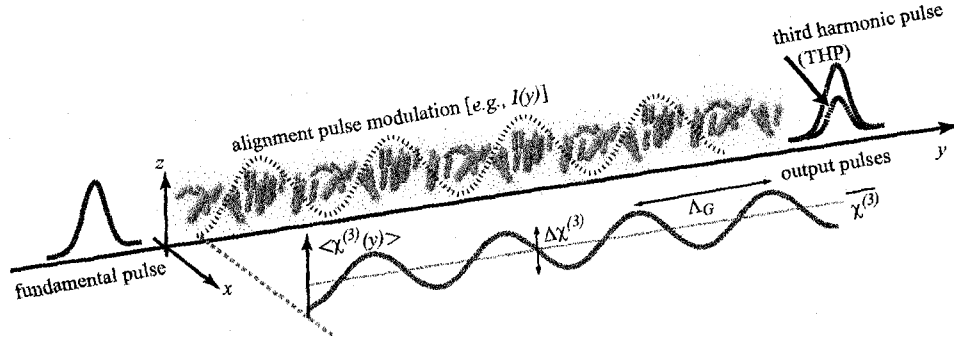


Figure 4.2: In the dynamic QPM concept, a spatio-temporally controlled ultrafast alignment pulse propagating in the x -direction creates a spatially modulated molecular alignment that evolves in time. A properly shaped alignment pulse creates a grating in the macroscopic nonlinear optical susceptibility of the molecular gas that is stationary in the group frame of the fundamental pulse. Setting the periodicity of the nonlinear grating to a periodicity of twice the coherence length for third harmonic generation leads to efficient conversion from the fundamental to the third harmonic.

An alignment pulse propagating along the x -direction is focused to a line along the direction of propagation of the fundamental pulse, i.e. the y -direction, and spatially modulated to control the molecular alignment along y . Since the molecular alignment is transient, the specific molecular alignment encountered by the fundamental pulse for a spatial location along y depends on the spatio-temporal profile of the alignment pulse and the relative delay between the alignment and fundamental pulses, $\tau_{a-f}(y)$.

The spatio-temporal evolution of the molecular alignment is illustrated in Fig. 4.3. If the alignment pulse propagating along the x -direction contains zero pulse front tilt along the y -direction, then the transient molecular alignment is initiated simultaneously along the entire line focus. The group delay accumulated by the fundamental pulse leads to a linear increase in the delay between the alignment and fundamental pulses given by $\tau_{a-f}(y) = \tau_0 + v_g^{-1} y$, where v_g is the group velocity of the fundamental pulse and τ_0 is the alignment-fundamental delay at the entrance of the gas (i.e. $y = 0$) as shown in Fig. 4.3(b). The increasing τ_{a-f} leads to a variation of alignment sampled by the fundamental pulse as it propagates and is illustrated in fig. 4.3(c).

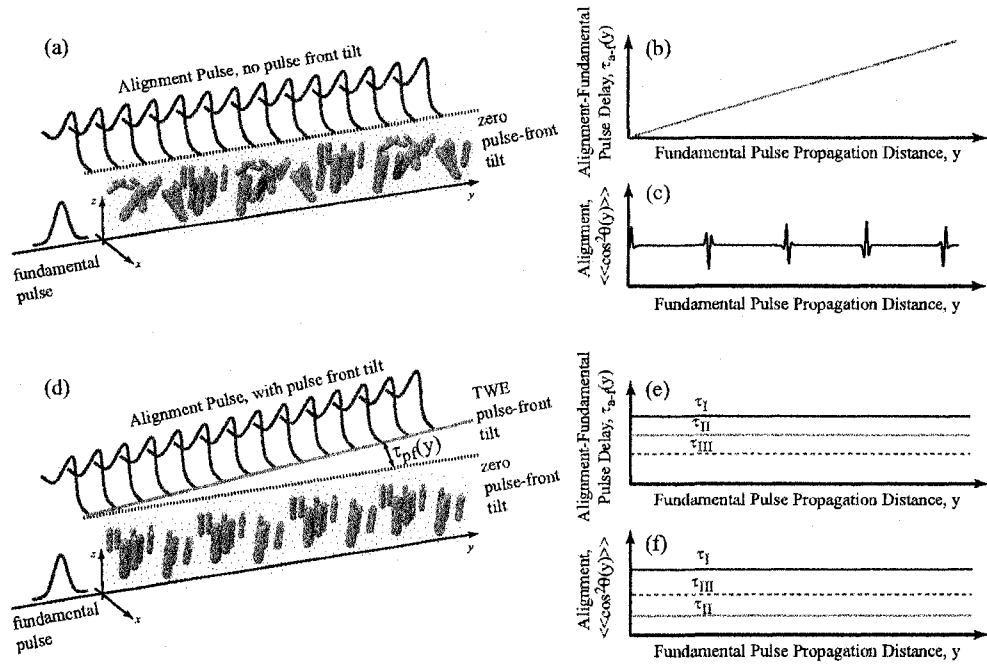


Figure 4.3: The spatio-temporal evolution of the molecular alignment in the group frame of the fundamental pulse is shown here. For an alignment pulse with no pulse-front tilt (a), the transient alignment begins at each y location simultaneously. With propagation, the delay between the alignment and fundamental pulses, $\tau_{a-f}(y)$, increases at the rate of the fundamental pulse group velocity (b). The variation in $\tau_{a-f}(y)$ results in an evolution of the molecular alignment experienced by the fundamental pulse with propagation (c). By matching the group-delay of the fundamental pulse and pulse-front tilt of the alignment pulse [i.e. TWE criterion] (d), a stationary alignment-fundamental pulse delay [i.e., $\tau_{a-f}(y) = \text{const}$] (e) and thereby a constant alignment with propagation [i.e., $\langle\langle\cos^2\theta(y)\rangle\rangle = \text{const}$] (f) can be selected.

The variation of the molecular alignment with propagation of the fundamental pulse prevents control over the nonlinear susceptibility in the reference frame of the fundamental pulse. Moreover, the large changes in the nonlinear susceptibility which are necessary to form an efficient QPM nonlinear grating only occur near revival events. Between the revivals the orientational probability density is nearly uniform. To attain strong control of the nonlinear susceptibility, we must maintain the arrival time of the fundamental pulse relative to the alignment pulse for any propagation distance y within a ~ 100 -fs temporal window. If the alignment pulse has no pulse-

front tilt (Fig. 4.3(a)), then with propagation, the accumulated relative delay between the alignment and fundamental pulses will exceed 100-fs after propagating only 30- μm , which is a small fraction of the coherence length of the process. Clearly, the transient nature of the alignment requires both spatial and temporal control over the molecular dynamics along the y -direction.

The introduction of a pulse-front tilt along the y -direction of the alignment pulse as shown in Fig. 4.3 (d) allows control over the pulse delay between the alignment and fundamental pulses, τ_{a-f} . The alignment fundamental pulse delay slip that occurs with a simple line focus can be eliminated by setting the pulse-front tilt along the y -direction to be the group velocity of the fundamental pulse, meeting the travelling wave excitation (TWE) criterion. This may be accomplished by inserting an optical element causing angular dispersion, such as a prism, into the alignment beam path. The angular dispersion causes a pulse front tilt, which allows meeting the TWE criterion, as is shown for example in Ref. [89]. It follows that when the alignment fundamental pulse delay is invariant with propagation, a constant molecular alignment as shown in Fig. 4.3(e) is maintained in the reference frame of the fundamental pulse along its propagation direction. Fig. 4.3(f) illustrates how an adjustment of the alignment fundamental pulse delay allows the constant molecular alignment experienced by the fundamental pulse to be chosen.

However, to make use of the controlled molecular alignment for quasi phase matching, the fundamental pulse must experience a variation in the nonlinear susceptibility with propagation along the y -direction. There are many ways that a periodic modulation of the molecular alignment and thus a periodic modulation of the nonlinear susceptibility can be realized. Fig. 4.4 shows two examples. In Fig. 4.4 (a), the intensity of the alignment pulse is modulated periodically along the y -direction. Because we have met the TWE criterion, the local intensity modulation of the pump pulse at a specific spatial location y translates into a modulation of the molecular

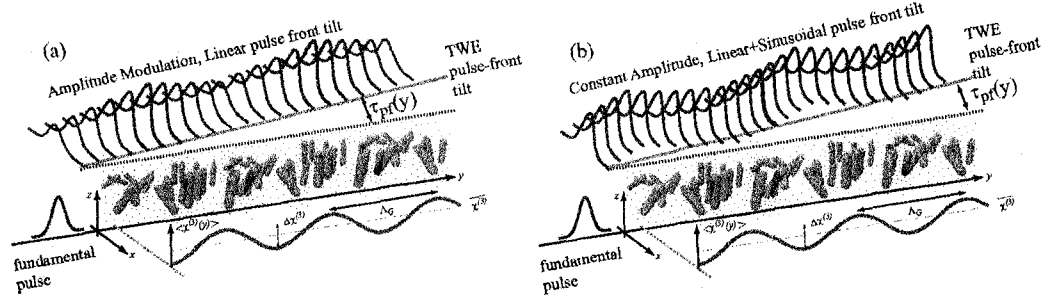


Figure 4.4: A nonlinear susceptibility grating in the frame of the propagating fundamental pulse can be formed by (a) spatially modulating the alignment pulse intensity and meeting the TWE criterion or by (b) modulating the pulse front delay of the alignment pulse to modulate the alignment strength experienced by the fundamental pulse.

alignment experienced by the fundamental pulse. The periodic molecular alignment translates directly into a periodic modulation of the nonlinear susceptibility, forming a nonlinear grating in the group frame of the fundamental pulse. Another route to the formation of a nonlinear grating is through a modulation the pulse-front tilt of the alignment pulse as shown in Fig. 4.4(b). In this method, a sinusoidal modulation on the pulse front tilt is added to the linear pulse front tilt that meets the TWE criterion. The magnitude of the pulse front tilt modulation is such that the alignment in the reference frame of the fundamental pulse oscillates between maximum (Fig. 4.1, τ_I) and minimum (Fig. 4.1, τ_{II}) alignment after a coherence length. The pulse-front modulation approach provides the largest depth of modulation on the nonlinear grating, and thus is capable of the highest conversion efficiency in the nonlinear mixing process. Experimentally, this may be realized by inserting a phase grating, consisting, for example, of fused silica.

With the spatial modulation of the alignment pulse, a dynamic nonlinear grating in the nonlinear susceptibility can be formed in a molecular gas that appears as a spatially varying nonlinear grating in the group frame of the fundamental pulse. This grating formation and the relevant dynamic quasi phase matching that the dynamic grating formation enables are unique to gas and liquid phases. For efficient

nonlinear frequency conversion with the dynamic QPM grating, the alignment pulse must then be spatially modulated with a periodicity of twice the coherence length of the nonlinear conversion process. In the next section, we numerically simulate the dynamic QPM process in a molecular gas.

4.3 Estimation of achievable enhancement

In the previous section, we described a method for sculpting the spatio-temporal evolution of the transient alignment of molecules in a gas to form a nonlinear grating for QPM. Although, this approach will work for many nonlinear optical processes, we demonstrate its efficacy by simulating the dynamic QPM process for third harmonic generation (THG). The phase mismatch of the THG process in molecular gases at atmospheric pressure requires a \sim mm-scale grating period, which is an experimentally accessible region for both intensity and pulse front modulation. In the specific geometry considered in Fig. 4.4 (b), we sinusoidally modulate the alignment pulse along the propagation direction of the fundamental (y -direction). This forms a grating in the third-order nonlinear susceptibility along the y -direction of the form $\langle \chi_{jjjj}^{(3)}(y) \rangle = \bar{\chi}^{(3)} + \frac{1}{2}\Delta\chi^{(3)}\cos(K_G y)$, where the average susceptibility of the nonlinear grating, $\bar{\chi}^{(3)} \equiv \langle \chi_{jjjj}^{(3)} \rangle_{avg}$, and the grating depth of modulation, $\Delta\chi^{(3)} = \langle \chi_{jjjj}^{(3)} \rangle_{max} - \langle \chi_{jjjj}^{(3)} \rangle_{min}$, are determined by the molecular alignment. The periodicity of the non linear grating is set to be twice the coherence length of the THG process, where the coherence length is defined as $L_{coh} = \pi/\Delta k$ and $\Delta k = 3k(\omega_1) - k(\omega_3)$ is the phase mismatch of the THG interaction. The wave vector of the grating is $K_G = 2\pi/\Lambda_G$, where $\Lambda_G = 2L_{coh}$ is the grating period. For example, the coherence length of THG at 1000 Torr for is ~ 0.4 mm for C_2H_2 [90].

Because the conversion efficiency is proportional to $(\Delta\chi^{(3)})^2$, we consider the limiting case of the depth of modulation where the maximum susceptibility occurs

for nearly full alignment ($\langle \cos^2\theta \rangle \simeq 1$) and the minimum of the susceptibility at nearly minimal alignment ($\langle \cos^2\theta \rangle \simeq 0$). We calculate the expectation values of $\langle \cos^2\theta(\tau_d) \rangle \equiv \langle \psi(\tau_d) | \cos^2\theta | \psi(\tau_d) \rangle$ and $\langle \cos^4\theta(\tau_d) \rangle$, using the rotational wave function, $|\psi(\tau_d)\rangle$, for low-temperature molecular alignment in the impulsive limit[91], where τ_d is the time after the alignment pulse. The ensemble-averaged susceptibility is evaluated at $\tau_d = \tau_{max}$ and $\tau_d = \tau_{min}$, where τ_{max} and τ_{min} are the times of strong alignment and anti-alignment of the molecules, respectively. The numerical values are $\langle \cos^2\theta(\tau_{min}) \rangle = 0.154$, $\langle \cos^4\theta(\tau_{min}) \rangle = 0.055$, $\langle \cos^2\theta(\tau_{max}) \rangle = 0.845$ and $\langle \cos^4\theta(\tau_{max}) \rangle = 0.780$. Applying these alignment factors to the averaged susceptibility yields $\bar{\chi}^{(3)} = 1.5 \cdot 10^{-24} m^2 V^{-2}$ and $\Delta\chi^{(3)} = 4.7 \cdot 10^{-25} m^2 V^{-2}$ for 1000 Torr of acetylene[90] for $j=z$.

Due to the transient nature of the molecular alignment, the fundamental pulse must be shorter than the duration of a rotational revival. For the required ultrashort laser pulses, the group velocity walk-off becomes important and must be considered in the calculation. As a result, we must numerically solve the propagation equations describing the nonlinear interaction. The equations describing the evolution of the complex, slowly-varying envelope of the fundamental and third harmonic plane-wave pulses, where $E_m(y, t) = \frac{1}{2}\{A_m(y, t)\exp[i(k_my - \omega_mt)] + c.c.\}$, can be written as:

$$\frac{\partial A_1(y, t)}{\partial y} + \frac{1}{v_{g1}} \frac{\partial A_1(y, t)}{\partial t} - i\tilde{D}_1 A_1(y, t) = -\gamma_1 [3A_1|A_1|^2 + 6A_1|A_3|^2 + 3A_3A_1^*A_1^* e^{-i\Delta ky}] \quad (4.9)$$

$$\frac{\partial A_3(y, t)}{\partial y} + \frac{1}{v_{g3}} \frac{\partial A_3(y, t)}{\partial t} - i\tilde{D}_3 A_3(y, t) = -\gamma_3 [3A_3|A_3|^2 + 6A_3|A_1|^2 + A_1^3 e^{i\Delta ky}], \quad (4.10)$$

where $v_{gm} = (\partial k(\omega)/\partial \omega|_{\omega_m})^{-1}$ is the group velocity at frequency ω_m , $\gamma_m = \langle \chi_{jjjj}^{(3)}(y) \rangle \omega_m / (8cn_m)$ is the non linear coupling coefficient, n_m is the refractive index at frequency ω_m , c is the speed of light in vacuum, and $\tilde{D}_m = \sum_{l=2}^{\infty} 1/l! k_{m,l} (i\partial/\partial t)^l$ describes higher order

dispersion. The expansion coefficients $k_{m,l}$ are given by $k_{m,l} = \partial^l k(\omega) / \partial \omega^l |_{\omega_m}$.

Equations (4.9) and (4.10) were solved numerically using the symmetric split-step method[21], including dispersion up to fourth order. The numeric solutions demonstrate that the group velocity mismatch (GVM), self phase modulation (SPM) and cross phase modulation (XPM) limit the conversion efficiency. GVM, defined as $\Delta v_g^{-1} = v_g(\omega_1)^{-1} - v_g(\omega_3)^{-1}$, causes a temporal walk-off between the fundamental and third harmonic pulses, reducing the conversion efficiency. The characteristic length of this walk-off, $L_w = \tau |\Delta v_g|$, scales with the pulse duration.

In these calculations, we propagate 50-fs Gaussian laser pulses with a peak intensity of 10^{12} Wcm^{-2} centered at 800-nm in 1000-Torr of acetylene gas. We compare the conversion efficiencies of dynamic-QPM for the cases of substantial group velocity mismatch and nearly compensated GVM. For GVM compensation, we consider propagation in a $21.7 \mu\text{m}$ diameter hollow-core fiber, yielding a walk-off rate of 0.053 fscm^{-1} in 1000-Torr of C_2H_2 . With this fiber diameter, the fiber dispersion nearly matches the group velocity of the fundamental and harmonic pulses and requires a propagation length of 9.4-m for two 50-fs laser pulses to become temporally separated. The limiting effect of GVM is demonstrated by comparing the GVM-compensated case to propagation in a $60 \mu\text{m}$ diameter hollow-core fiber. In this wider fiber, the walk-off rate between the fundamental and third harmonic laser pulses is 10.2 fscm^{-1} , resulting in a 4.9-cm walk-off length for 50-fs pulses.

Figure 4.5 shows the calculated conversion efficiency $\eta(y) = \int dt |A_3(y, t)|^2 / |A_1(y = 0, t)|^2$ of dynamic-QPM for the two cases considered. The parameters used in the calculations were: $\gamma_1 = 1.48 \cdot 10^{-18} \text{ m/V}^2$, $\gamma_3 = 4.45 \cdot 10^{-18} \text{ m/V}^2$ using $\bar{\chi}^3$ and $\gamma_3 |A_1|^2 L = 0.465$; the dispersion was applied in the frequency domain. The values for the dispersion parameters in the rest frame of the fundamental pulse for the case of GVM compensation were: $k_{1,0} = 7.856 \cdot 10^6 \text{ 1/m}$, $k_{1,1} = 0$, $k_{1,2} = -1.0375 \cdot 10^3 \text{ fs}^2/\text{m}$, $k_{1,3} = 1.4818 \cdot 10^3 \text{ fs}^3/\text{m}$, $k_{1,4} = -2.4337 \cdot 10^3 \text{ fs}^4/\text{m}$ for the fundamental pulse,

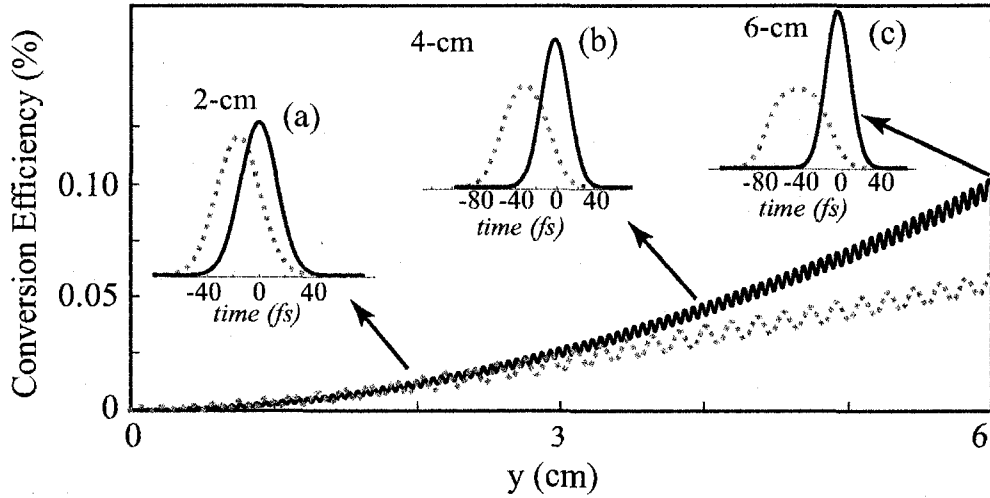


Figure 4.5: Conversion efficiency for a 50-fs fundamental pulse propagating in a $60 \mu\text{m}$ (dashed) and $21.7 \mu\text{m}$ [GVM-compensated] (solid) diameter hollow-core fiber filled with C_2H_2 . The insets show the third harmonic pulse shapes after 2(a), 4(b), and 6(c) cm of propagation.

and $k_{3,0} = 2.358 \cdot 10^7 \text{ 1/m}$, $k_{3,1} = -5.2994 \text{ fs/m}$, $k_{3,2} = 4.4406 \cdot 10^2 \text{ fs}^2/\text{m}$, $k_{3,3} = 1.6064 \cdot 10^2 \text{ fs}^3/\text{m}$, and $k_{3,4} = 23.2036 \text{ fs}^4/\text{m}$ for the third harmonic pulse. The solid line represents the conversion efficiency for GVM compensated propagation of the fundamental and third harmonic pulses, the dashed line represents the conversion efficiency for no GVM compensation. The insets show the third harmonic pulses after propagating 2, 4 and 6 cm respectively for GVM compensation (solid) and no GVM compensation (dashed). Since the maximum conversion efficiency is $\approx 0.1 \%$, the change in the intensity of the fundamental pulse is minimal and not shown. Initially, the larger diameter fiber proves more efficient due to the longer coherence length (determined by overall dispersion). However, after propagation through a walk-off distance, the conversion efficiency in the $60 \mu\text{m}$ diameter fiber ceases to increase substantially with further propagation. The GVM-compensated conversion efficiency, however, continues to increase rapidly as shown in Fig. 4.5. The reduction in conversion efficiency due to pulse walk-off can be seen in Fig. 4.6 as a stretching of

the pulse THG pulse in time, distorting the temporal shape and reducing the phase-matched bandwidth. A red-shifting of the pulse that has walked off is evident due to cross-phase modulation from the fundamental laser pulse.

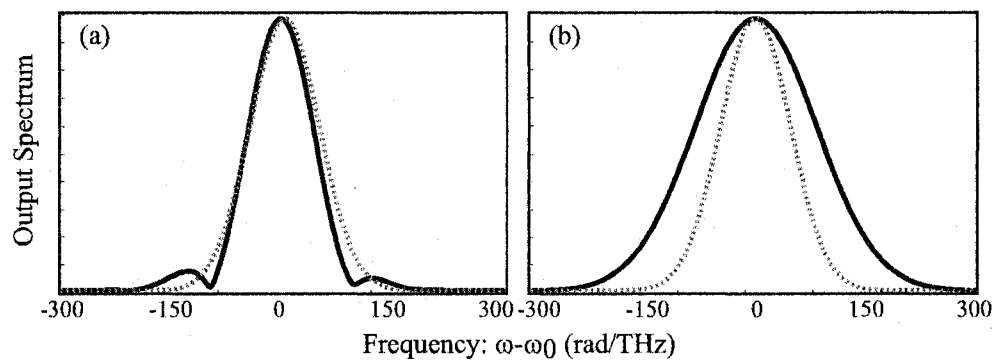


Figure 4.6: Normalized spectra of fundamental (dotted line) and third harmonic pulses (solid line) after 6-cm of propagation in a nonlinear grating formed through molecular alignment for $60 \mu\text{m}$ (a) and $21.7 \mu\text{m}$ [GVM-compensated] (b) diameter hollow-core fibers.

Part II

Experimental Observations

In this part we will present experimental observations of the propagation effects due to coherent nuclear motion (CNM). In Chap. 5 the propagation effects due to the effective linear susceptibility will be presented. We start off by showing that spectral interferometry can be used to detect molecular alignment via the change in the index of refraction of the medium during rotational wave packet revivals. In Sec. 5.2 we describe a modified version of spectral interferometry which allows the detection of CNM in a single shot over the duration of 1-2 ps. Contrary to standard polarization gating techniques this single-shot technique allows the detection of a rotational wave packet from an arbitrarily polarized pump pulse. One of the traditional ways of detecting rotational revivals is to utilize the alignment-induced birefringence. However, for a circularly polarized pump pulse the gas is not birefringent in the polarization plane of the pump pulse since the orientational probability distribution of the molecules is azimuthally symmetric about the direction of propagation in this case. The last effect of the time-dependent "linear" susceptibility arising due to CNM described here is a modification of the group velocity of the probe pulse. The modulation on the pump-probe delay is expected to vary as $\chi(t)$ based on the theory developed. What has been observed, on the other hand, is a modulation of the group velocity which appears proportional to either the derivative or the integral of $\chi^{(3)}(t)$ with respect to the pump-probe delay. This discrepancy has not been resolved at the time of this writing. In Sec. 5.4 we show that the effect of temporal phase modulation due to CNM ranges from essentially a pure phase modulation with negligible spectral distortions to extreme spectral modulation. Specifically, if a weak linearly polarized probe pulse propagates during a revival of a rotational wave packet the action of the effective linear susceptibility will range from changing the polarization state of the pulse due to the birefringence present in the medium to splitting the probe pulse into two pulses which are distinct in their polarization state as well as in their spectral content.

In addition to the propagation effects due to the effective linear susceptibility, the effects originating from the dependence of the non-linear induced polarization density on CNM have been investigated as well and are detailed in Chap. 6. In particular, we have focused on the dependence of $\chi^{(3)}(t)$ on coherent rotational as well as vibrational motion of the nuclei. That dependence is expected to manifest itself in a variation of the conversion efficiency to the third harmonic as a function of pump-probe delay. First, we discuss THG during molecular alignment. The gas no longer acts as an isotropic medium with only Type I conversion processes allowed, but as a birefringent medium which allows Type I as well as Type II processes. We have identified the presence of both in our experiments and discuss the possibility for phase matching Type II processes for strong molecular alignment such as could be achieved when the gas is rotationally cool. A modulation of the conversion efficiency for vibrational motion has been observed as well. We have used SF₆ for this purpose since it possesses a relatively low-frequency, fully-symmetric breathing mode with a large Raman cross-section which can be impulsively excited with ≈ 40 -fs pulses.

Finally, in Sec. 6.2 a strongly enhanced conversion to the third harmonic is discussed. This effect is independent from CNM. It has been measured in molecular as well as atomic gases and is attributed to the presence of a laser induced plasma in the focal region of the probe pulse. The level of enhancement depends in detail on a variety of experimental parameters, e.g., gas pressure, pump- and probe pulse energies, the focal length, and the ionization potential of the molecule or atom, just to name a few. We are developing a theoretical model to shed light on the underlying physics responsible for the effect. With guidance from a good model, it is anticipated that the enhancement can be further optimized and this technique might serve as the starting point for the development of a broadband UV source.

Chapter 5

Propagation effects due to "linear" susceptibility modulation

5.1 Spectral Interferometry as a way to detect molecular alignment

The index of refraction of an ensemble of gas molecules is modulated by transient molecular alignment. This has been shown in Sec. 3.3, where an expression for an effective linear susceptibility due to coherent nuclear motion was derived, and has been the basis of the earliest detection methods via the birefringence induced in the medium by the alignment. The relative phase accumulated by a weak, linearly polarized probe pulse will therefore vary as a function of pump-probe delay during wave packet revivals. If a reference pulse, co-propagating with the probe pulse, but adequately delayed such that the reference pulse propagates in-between revivals, is made to interfere with the probe pulse in a spectrometer, the relative phase difference as a function of pump-probe delay can be extracted from the interferogram. This technique allows for the direct detection of $\langle\langle\cos^2\theta(t)\rangle\rangle$, whereas other techniques merely detect its modulus.

To demonstrate the feasibility of using spectral interferometry for the detection of molecular alignment we use it to map the quarter revival of a rotational wave packet in CO₂. A half-wave plate and polarizing beam splitter were used to separate 1.3-mJ, \approx 50-fs pump pulses from a Ti:sapphire amplifier into pump and probe arms where 90% of the pulse energy remained in the pump arm. The probe arm contained a 12-mm thick KDP crystal cut at 44.9 and a retro reflecting mirror mounted on a motorized translation stage to vary the pump-probe delay. The crystal angle was set to produce two pulses separated by 2.2 ps after double-passing the KDP crystal, forming a probe pulse-pair that was orthogonally polarized to the pump pulse[92]. All pulses were then focused into a gas cell containing CO₂ at a pressure of 810 Torr. The relative delay between the probe pulses and the pump pulse was set to $\tau_o \approx 10.6$ ps, so that the probe pulses coincided with the quarter revival of the wave packet. The pump-probe delay was then scanned about τ_o and the interferogram between the probe pulse pair was recorded with an Ocean Optics USB2000 spectrometer.

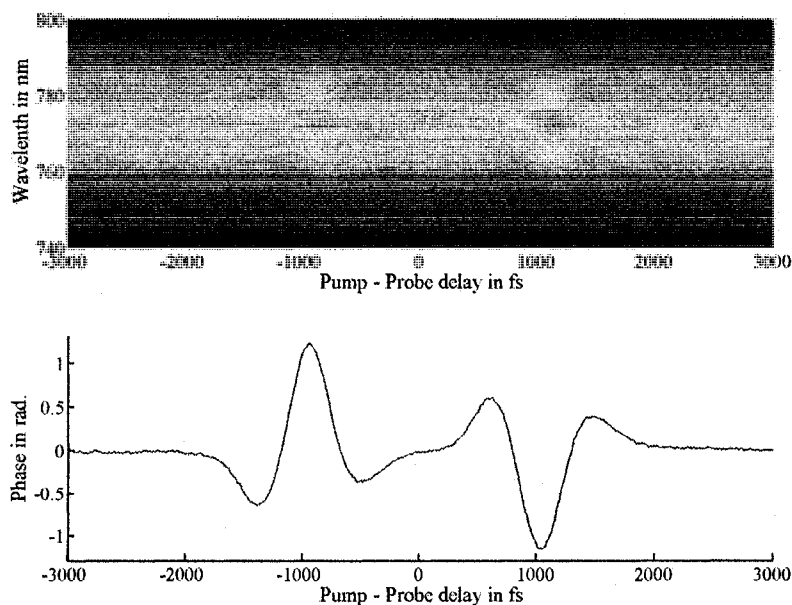


Figure 5.1: (a) Measured interferogram at a gas pressure of 810 Torr. (b) Relative phase between probe and reference pulses. The noise is extremely low since we were using a birefringent crystal to split the probe pulse into a probe-reference pulse pair.

The measured interferogram is shown in Fig. 5.1(a) for a scan interval of ± 3 ps, while (b) shows the extracted phase. Using a birefringent crystal in order to split up the probe pulse into a probe-reference pulse pair results in an extremely low-noise interferogram since the probe and reference pulses travel on a common path. The phase difference accumulated between probe and reference is clearly visible, and is directly proportional to the molecular alignment.

5.2 Single Shot Measurement of Temporal Phase Modulation

As outlined in Sec. 3.3, the linear propagation effect of a rotational wave packet on a weak probe pulse can be expressed in terms of an effective, time-varying linear susceptibility. The polarization state of the pump pulse determines whether the resulting effective linear susceptibility tensor is uniaxial or biaxial. Direct measurements of the transient susceptibility provide detailed information regarding the rotational wave packet. In particular, it is useful to be able to resolve the time-varying susceptibility along the eigenpolarization directions of the tensor. Earlier methods of probing the rotational wave packet dynamics using the transient birefringence [45, 68] do not resolve the time-varying susceptibility along the eigenpolarization directions of the tensor. Also, since the birefringence of the medium lies in a plane orthogonal to the polarization plane of the pump pulse, and for co-propagating pulses, consequently also the probe pulse, these methods will not result in a signal due to the molecular alignment at all.

5.2.1 Phase accumulation and birefringence due to a rotational wave packet

Briefly, we will illustrate the resulting molecular alignment symmetry for various cases of pump pulse polarization. For a linearly polarized pump pulse, the coordinate system is defined by the direction of polarization (\hat{z}) and the direction of propagation (\hat{y}). The molecules align along the polarization direction of the pump pulse and anti-align in the $\hat{x}\hat{y}$ -plane. With the interaction Hamiltonian given by

$$H_{\text{lin}} = -\frac{\Delta\alpha}{4}\mathcal{E}^2(t)\cos^2\theta,$$

it can be seen that the interaction is independent of ϕ , i.e., the orientational probability distribution will be symmetric about the z -axis. A linearly polarized probe pulse co-propagating with the pump pulse, i.e., the polarization of the probe pulse lies in the $\hat{z}\hat{x}$ -plane, will therefore accumulate a phase difference between its \hat{z} and \hat{x} components. The gas acts as a uniaxial crystal with $n_z(\omega) \neq n_x(\omega)$. This is precisely the effect which has been used by earlier methods to detect molecular alignment.

For a circularly polarized pump pulse, on the other hand, the interaction Hamiltonian is given by

$$H_{\text{circ}} = -\frac{\Delta\alpha}{8}\mathcal{E}^2(t)(\cos^2\theta + \cos^2\phi).$$

The direction of propagation is again \hat{y} , with the plane of polarization defined by \hat{x} and \hat{z} . The interaction is no longer azimuthally symmetric in this frame. If, however, we define \hat{z} to be given by the direction of propagation so that \hat{x} and \hat{y} define the polarization plane of the circularly polarized pulse, the Hamiltonian can be written as

$$H_{\text{circ}} = -\frac{\Delta\alpha}{8}\mathcal{E}^2(t)\cos^2\theta.$$

From this, one can see that in this new frame the interaction is again independent of

ϕ , i.e., the orientational probability distribution is azimuthally symmetric about the direction of propagation. The molecules align along the direction of propagation and anti-align in the plane of polarization. So, there is no birefringence in the xy -plane but $n_z(\tau) \neq n_x(\tau)$. Therefore, the gas acts like a uniaxial crystal during the alignment periods for both linearly and circularly polarized pump pulses.

5.2.2 Chirped Spectral Interferometry

We have introduced a method to directly measure the phase modulation due to transiently aligned molecules for arbitrarily polarized pump pulses. This method no longer relies on a polarization state modification due to the aligned molecules, but directly measures the phase accumulated by the pulse with propagation. In addition to that, the method we are using here allows for the mapping of the temporal phase dynamics during a revival of the wave packet in a single-shot. Our single-shot measurement technique is based on the idea originally suggested by Valdmanis [93]. In his proposal, he suggests to use a strongly linearly-chirped ultrafast probe pulse to map the temporal dynamics due to the wave packet onto the probe pulse spectrum. The resulting phase accumulated by the spectral components of the pulse can then be mapped to the time axis via the linear chirp. This time-spectrum mapping has been applied to many physical systems [?, 94, 95]. A chirped spectral interferometry (CSI) adaptation of Valdmanis' technique has also been applied for the single-shot measurement of systems with a transient phase [96, 97, 98, 99].

The single-shot measurement of molecular phase modulation uses spectral interferometry between two identically chirped broad bandwidth laser pulses. This probe-reference pulse pair is sent into a molecular gas in which a pump pulse has excited a rotational wave packet, leading to a transient optical susceptibility. To measure the time-varying phase modulation imposed on a probe pulse by the transient optical susceptibility, the probe pulse is time delayed with respect to the pump pulse as to

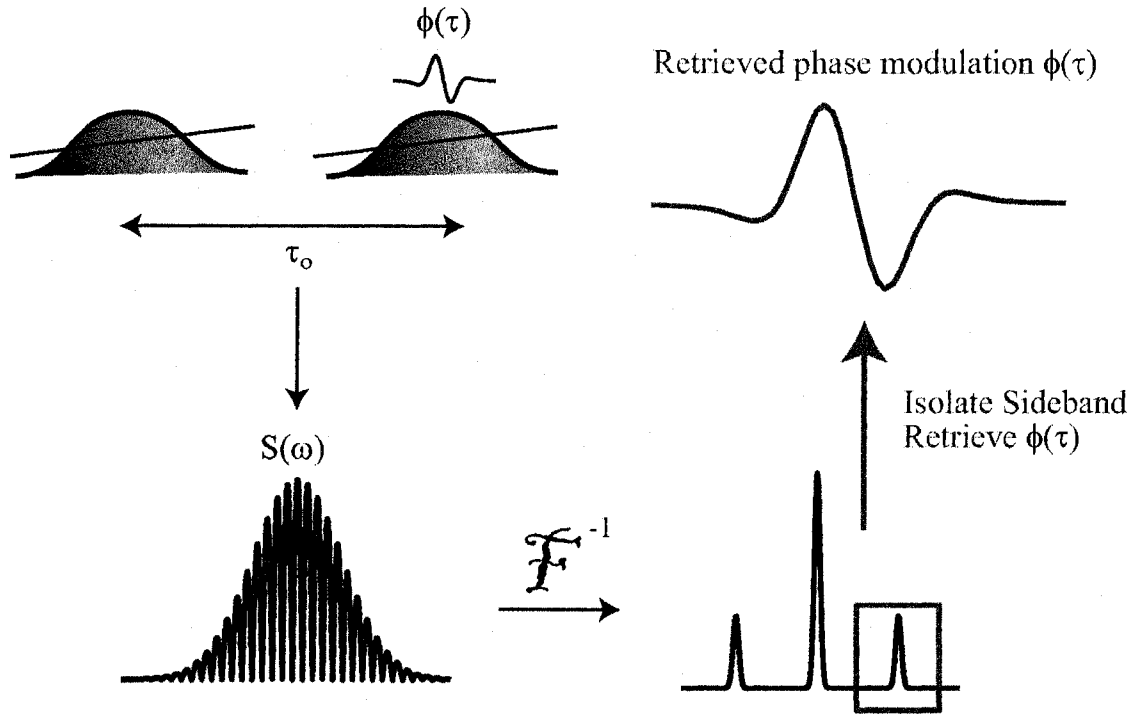


Figure 5.2: Algorithm for the phase retrieval of a single-shot measurement

coincide with a revival of the rotational wave packet, which is indicated schematically in Fig. 5.4(a). It thus accumulates phase as a function of time. The reference pulse delay is set so that it overlaps with a time-invariant region of the transient molecular response. Hence, the transient phase modulation can be extracted directly from the interferogram of the probe and reference pulses. It is therefore possible to fully resolve the time dependence of the linear susceptibility tensor components. By contrast, polarization gating techniques[45, 68] measure the modulus of a time-varying birefringence, i.e, the magnitude of the difference between two components of the linear transient susceptibility tensor.

5.2.3 $\chi_{\text{eff}}^{(1)}(t)$ in the presence of a rotational wave packet

The procedure for obtaining the effective linear susceptibility in the presence of a rotational wave packet has been outlined already. Hence, only a brief summary of previous results is given here. Formally, the macroscopic linear optical susceptibility tensor for

transiently-aligned molecules in a dilute, non-absorbing gas is found by computing the orientational average $\chi_{ij}(t) = \frac{N}{c_0} \int r_{ik} \alpha_{kl} r_{lj} G(\theta, \phi, t) d\Omega$, where repeated indices are summed over. Here, $G(\theta, \phi, t)$ is the orientational probability distribution in the presence of the rotational wave packet, and r_{ij} are direction cosines which transform between the laboratory $(\hat{x}, \hat{y}, \hat{z})$ and molecular coordinates $(\hat{X}, \hat{Y}, \hat{Z})$. Considering the properties of $G(\theta, \phi, t)$ and the pump-pulse-molecule interaction, one finds that for a single pump pulse, the linear susceptibility tensor is diagonal in the coordinate system defined by the propagation direction and the polarization plane of the pulse. For an elliptically-polarized pump pulse, the tensor is biaxial, and reduces to a uniaxial tensor for a linearly or circularly polarized pump pulse. When the probe and reference pulses propagate collinearly with the pump pulse, the propagation direction is along one principle axis of the linear susceptibility tensor. The eigen-polarization directions of the transient susceptibility tensor are along the other two principle axes. It is interesting to note that for the special case of a circularly polarized pump pulse, the propagation direction is commensurate with the optical axis of the transient susceptibility tensor, implying an absence of birefringence in the polarization plane of the probe pulse.

5.2.4 Experimental setup

In the experiments, pulses of up to ~ 1.6 mJ in energy with a duration of ≈ 40 -fs and centered at 780-nm are produced by a multipass Ti:sapphire amplifier (KMLabs). The experimental setup is schematically depicted in Fig. 5.3. Approximately 10% of the pulse energy is split off and frequency doubled in a 150- μm thick BBO crystal and subsequently chirped with a 9-cm long BK7 glass rod to a duration of ≈ 1.3 ps. The probe and reference pulses are formed from the chirped frequency-doubled pulse with a Michelson interferometer. The remaining energy comprises the pump pulse. A half wave plate is used to rotate the polarization of the pump pulse prior to passing

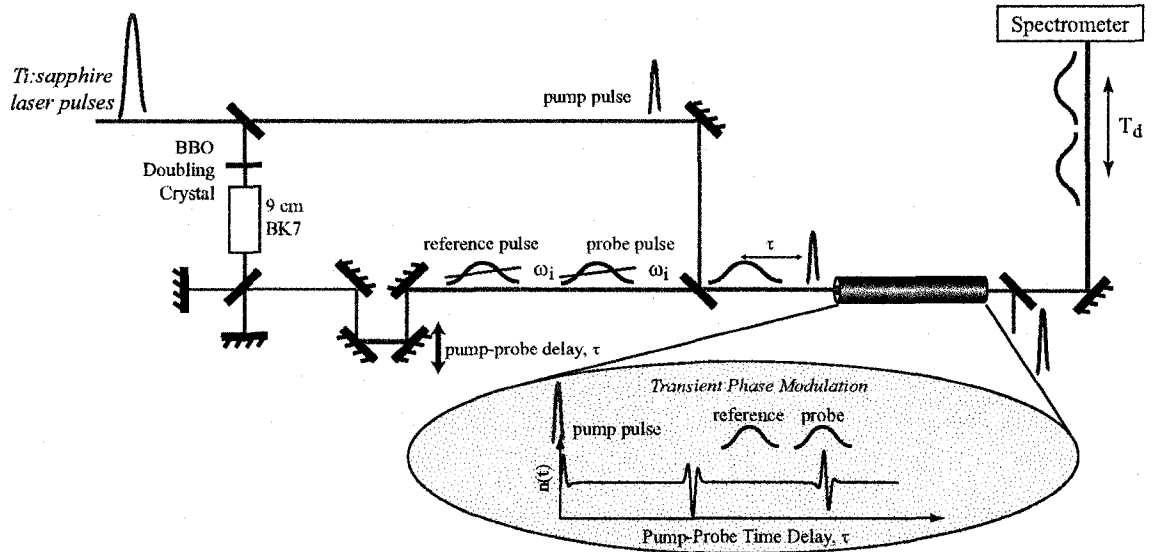


Figure 5.3: Single-shot experimental setup

through a quarter wave plate. The combination of the half and quarter wave plates allows control of the pump pulse polarization, while keeping the eigen-directions of the excited transient susceptibility tensor fixed. Thus, the slow and fast axes of the quarter-wave plate define \hat{z} and \hat{x} , respectively. The delay between the probe-reference pulse pair and the pump pulse is set to ≈ 10.65 ps so that it coincides with the quarter revival of the wave packet. The reference pulse is delayed with respect to the probe pulse by ≈ 2.8 ps, ensuring that it propagates in between wave packet revivals without accumulating any transient phase. In the cases of linear and circular pump pulse polarization, the pulses are coupled into a 15-cm long, 150- μm diameter hollow core fiber filled with ~ 20 to ~ 40 Torr of CO_2 gas. The gas pressure is kept low in order to prevent substantial modification of the spectrum due to the temporal phase modulation[34]. At the exit of the fiber, a dichroic beam splitter directs the probe and reference pulses into a spectrometer (Ocean Optics HR4000) where an interference pattern is recorded.

5.2.5 Analysis of experimental results

The measured interferogram can be written as

$$S(\Omega) = |\tilde{E}_{\text{ref}}(\Omega)|^2 + |\tilde{E}_{\text{pr}}(\Omega)|^2 + \tilde{E}_{\text{ref}}^*(\Omega)e^{-iT_d\Omega}\tilde{E}_{\text{pr}}(\Omega) + \tilde{E}_{\text{ref}}(\Omega)e^{iT_d\Omega}\tilde{E}_{\text{pr}}^*(\Omega),$$

where $\tilde{E}_{\text{pr}}(\Omega)$ and $\tilde{E}_{\text{ref}}(\Omega)$ are the Fourier representations of the probe and reference pulses, respectively. The chirped probe and reference pulses are approximately given by $\mathcal{E}_c(t) = E_c \exp[-(a_c - ib)t^2] e^{i\omega_0 t}$ where $a_c = 2 \ln 2\tau_c^{-2}$ and $2b$ is the chirp rate. After propagation with the rotational wave packet, the probe pulse acquires a phase modulation due to the transient susceptibility, $\phi_{\text{mol}}(t)$, which varies across the duration of the pulse. This transient phase maps directly onto the spectral phase of the probe pulse with $t_\Omega = \Omega/2b$ with $\Omega = \omega - \omega_0$. Note that the temporal phase modulation is weak, and therefore, that distortion of the probe spectrum is negligible. Thus, the probe spectrum is approximately $\tilde{E}_{\text{pr}}(\Omega) \approx \tilde{E}_{\text{ref}}(\Omega)e^{i\phi_{\text{mol}}(t_\Omega)}$. With that, the mixing terms in the interferogram take the form, $\tilde{E}_{\text{pr}}(\Omega)\tilde{E}_{\text{ref}}^*(\Omega) = |\tilde{E}_{\text{ref}}(\Omega)|^2 e^{i\phi_{\text{mol}}(t_\Omega)}$. The spectral phase extracted with standard Fourier processing techniques contains the desired temporal phase modulation acquired by the probe pulse. Using the chirp rate of the probe pulse, the spectral phase difference can be mapped to the time domain and the transient modulation of the index of refraction can be obtained from that. It is directly proportional to the molecular alignment.

Accuracy of the single-shot phase measurement is validated by comparing to a scanning spectral interferometry (SSI) measurement of the phase due to the rotational wave packet. In the SSI experiment, a probe-reference pair with a short temporal duration is scanned through the quarter rotational revival as indicated in Fig.5.4(b). The phase modulation is retrieved from the SSI interferogram in a similar manner to CSI for each specific pump-probe delay. Fig. 5.4(c) shows a comparison of the transient phase response measured by both SSI and CSI due to the quarter revival

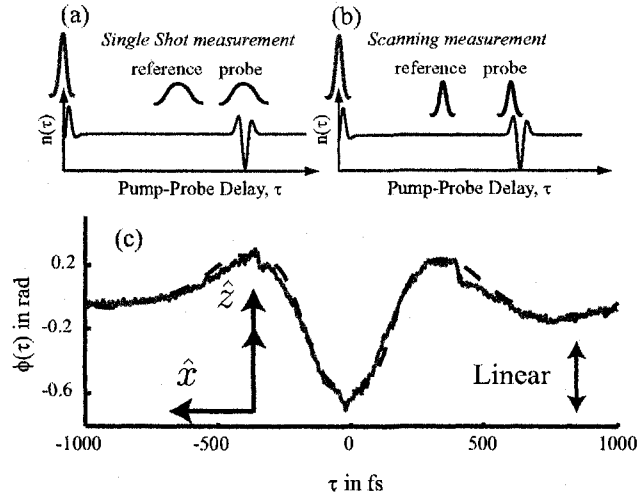


Figure 5.4: Relative timing of pump, reference, and probe pulses with respect to the transient index of refraction for scanning (a) and chirped single-shot measurements. (c) Comparison between the phase extracted from scanning (solid line) and single-shot (dashed line) interferograms.

of a rotational wave packet in 30 Torr of CO_2 . As indicated by the insets, the pump and probe pulses were co-polarized (i.e., along \hat{z}) for these measurements. The excellent agreement between the scanning (solid line) and single-shot (dashed line) measurements validates the accuracy of the single-shot technique which is based on the reliability of the simple linear spectral-to-temporal mapping and sufficient temporal resolution (estimated at $\approx 140\text{fs}$) of the retrieval algorithm applied to the single-shot interferogram. We note improved temporal resolution can be obtained with careful characterization of the reference pulse and processing the interferogram as a hologram [99].

Single-shot measurements of the transient phase modulation at the quarter-revival of CO_2 excited by a circularly polarized pump are shown in Fig. 5.5 for a linearly-polarized probe-reference pair oriented along \hat{x} (dashed line), \hat{z} (dotted line), and along 45° relative to \hat{z} (solid line), as indicated by the insets. The measured phase along those three directions is essentially identical, confirming an absence of birefringence as expected. We have experimentally verified that polarization gating (both

scanning and single-shot) indeed yields a null result as expected.

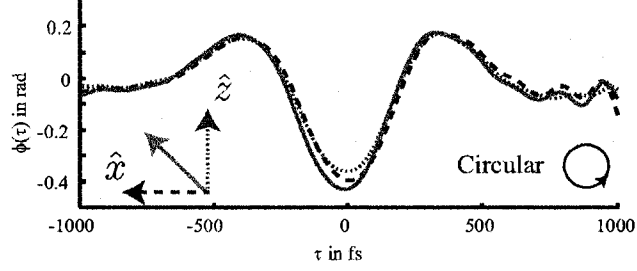


Figure 5.5: Measured single-shot phase accumulated by the probe pulse along \hat{x} (dashed, blue), \hat{z} (dotted, red) and 45° relative to \hat{z} (solid, green) for a wave packet excited by a circularly polarized pump pulse.

When moving to single-shot measurements with elliptically-polarized pump pulses, we replaced the hollow-core fiber with a simple gas cell, reducing the interaction to 7-mm. The reduction in interaction length allowed for a better assessment of the sensitivity limits of this measurement. By adjusting the gas pressure, we estimate the phase sensitivity of the single-shot measurements to be $\leq \pi/20$. Fig. 5.6 shows the single-shot measurements of phase modulation of the probe pulse for a rotational wave packet excited by an elliptically polarized pump pulse, resolved along \hat{x} (dotted) and \hat{z} (dashed). The pump pulse ellipticity is set by rotating the half wave plate in the pump arm to set the relative field strengths along \hat{z} and \hat{x} to a and b , respectively. In this measurement, the $\lambda/2$ -plate was rotated to an angle of $\approx 20^\circ \pm 4^\circ$ from an eigen-axis from which we estimate $a = 0.940 \pm 0.02$ and $b = 0.34 \pm 0.06$.

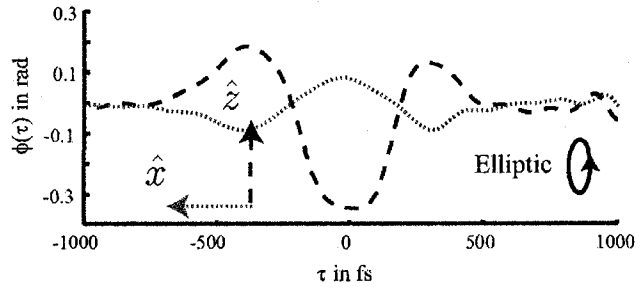


Figure 5.6: Measured phase modulation of the probe pulse along \hat{x} (dotted) and along \hat{z} (dashed) due to a wave packet excited by an elliptically polarized pump pulse.

5.2.6 Summary

We have developed a new technique that directly measures the time dependence of the linear susceptibility tensor components due to field-free rotational revivals excited by pump pulses of any polarization with high sensitivity. Unlike polarization gating which has been used in the past, our CSI method directly measures transient phase as opposed to the modulus of the birefringence. Moreover, we have demonstrated transient susceptibility measurements for circularly polarized pump pulses, as well as the experimental determination of the phase modulation along eigen-polarization directions of the transient susceptibility tensor. Beyond the application of transient susceptibilities for molecular phase modulation of ultrafast optical pulses, there are many other applications, which have been extensively discussed by Seideman et al[4].

5.3 Modification of Group Velocity due to molecular alignment

In addition to a time dependent phase accumulation by a weak probe pulse, a rotational wave packet and the molecular alignment occurring during the revivals of the wave packet affect the group velocity of the probe pulse. This effect is expected based on the time dependence of the effective linear susceptibility identified in Sec. 3.4. Using the propagation equation for the envelope found there and neglecting dispersion as well as any other term not of interest at the moment we can write the simplified equation as

$$\frac{\partial A_i(\zeta, \tau)}{\partial \zeta} = \frac{\omega_o}{c^2 k_o} \chi_{ij}^{(1)}(\tau - \tau_{PD}) \frac{\partial A_j(\zeta, \tau)}{\partial \tau} - \frac{i\omega_o^2}{2c^2 k_o} \chi_{ij}^{(1)}(\tau - \tau_{PD}) A_j(\zeta, \tau)$$

where we can see that the term

$$\frac{\omega_o}{c^2 k_o} \chi_{ij}^{(1)}(\tau - \tau_{PD}) \frac{\partial A_j(\zeta, \tau)}{\partial \tau}$$

can be interpreted as a modification of the group velocity of the pulse where the modification is proportional to $\chi^{(1)}(\tau)$. This relationship between the group velocity modification and the molecular alignment has not been confirmed experimentally. While the experiment does show a modified group velocity, its dependence on the alignment is not proportional to $\chi^{(1)}(\tau)$. In Sec. 5.3.2 we describe the model used to theoretically investigate this effect. We have solved Eq. 3.33 in order to find the field of the probe pulse after propagating in the presence of a rotational coherence, and we have carried out pump-probe experiments to verify the group velocity modification due to molecular alignment. The details of the experiment and the results are shown in Sec. 5.3.1.

5.3.1 Experimental investigations

For these experiments, the amplifier configuration differs from the other experiments described. Specifically, the difference lies in the pump laser used. Instead of the Coherent Evolution 30, a Quantronix Eagle was used delivering ≈ 90 W average power at 8 kHz repetition rate. With the increase in repetition rate the average output power is about 8 W resulting in pulses of about 0.8 mJ in energy. The pulse duration and the center wavelength remain at around 40 fs and 780 nm respectively. The experimental setup is shown in Fig. 5.7(a) and is mostly identical to that used for the CSI and TWP experiments. Using a surface reflection, approximately 10% of the pulse energy is split off and frequency doubled in a 150- μm thick BBO crystal, while the remaining energy constitutes the pump.

We use a dispersion compensated Michelson interferometer to obtain a probe-

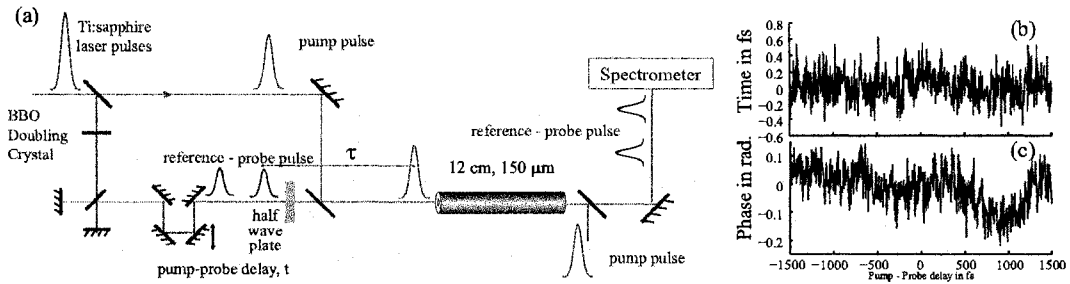


Figure 5.7: (a) Schematic of experimental setup used for detecting the group velocity modification of a weak probe pulse due to the transient molecular alignment. (b) Centroid of the sideband as a function of pump-probe delay at a gas pressure of 3 Torr. (c) Relative phase accumulated by the probe pulse during the half revival at a gas pressure of 3 Torr.

reference pulse pair in the probe arm. The delay between the probe-reference pulse pair and the pump pulse is set to ≈ 21.4 ps so that the probe pulse coincides with the half revival of the wave packet. All pulses are linearly polarized along \hat{z} . The reference pulse is delayed with respect to the probe pulse by ≈ 2.6 ps, ensuring that it propagates in between wave packet revivals without accumulating any transient phase or having its group velocity modified by the molecular alignment. The pulses are coupled into a 15-cm long, 150- μm diameter hollow core fiber filled with ~ 3 to ~ 240 Torr of CO_2 gas. As with the single-shot experiment, the gas pressure is again kept low to prevent substantial spectral modification[34]. A dichroic beam splitter directs the probe and reference pulses into a spectrometer (Ocean Optics HR4000) where an interference pattern is recorded.

5.3.1.1 Experimental Results

The relative phase accumulated by the probe pulse as well as its group velocity modification while propagating during a revival of a rotational wave packet can be extracted from the recorded interferograms. The interferograms have been recorded as a function of pump-probe delay centered around the half revival of the wave packet, which for CO_2 corresponds to a pump-probe delay of 21.4 ps. For each pump-probe

delay, the interferogram is inverse-Fourier transformed and the sideband is isolated. Any change in the group velocity of the probe pulse will of course result in a different spacing in time of the probe and reference pulses. This is detected in a variation of the fringe periodicity of the spectral interferogram, and consequently, in a modulation of the sideband's centroid. This centroid is shown in Fig. 5.7(b) for the case of an evacuated fiber. The probe-reference spacing should not change at all in that case, of course. The maximum change recorded however is about 0.5 fs, which represents the detection limit. Similarly, the relative phase accumulated by the probe pulse is extracted by Fourier transforming the sideband, and is shown in Fig. 5.7(c) for the case of an evacuated fiber. The relative phase between the probe and reference pulses exhibits a small drift of about 0.2 radians over the recorded pump-probe delay interval. The initial temporal spacing between the probe and reference pulses is 2.68 ps. Fig. 5.8(a) shows the recorded spectral interferograms, (b) the isolated sideband, (c) the extracted relative phase accumulated by the probe pulse, and finally, (d) the centroid of the sideband for a gas pressure of 80 Torr, and Fig. 5.9 shows the same data for a gas pressure of 240 Torr.

The accumulated relative phase as well as the changes in the probe-reference pulse spacing are well above the detection limits for both cases. The interferogram for a CO₂ pressure of 80 Torr shows that the probe spectrum is very slightly distorted, but quite negligibly so. This means that the maximum change in the probe-reference spacing of 8 fs is most likely not due to changes in dispersion. If the group velocity modification were due to a change in dispersion, a doubling of the center frequency of the probe pulse spectrum would result in a change in propagation time of less than 10 fs. As is obvious from the interferogram, the distortion of the spectra due to the temporal phase modulation of the transient molecular alignment is not nearly that strong for either case. The accumulated phase as well as the group velocity modification are about three times larger for 240 Torr than for 80 Torr which would

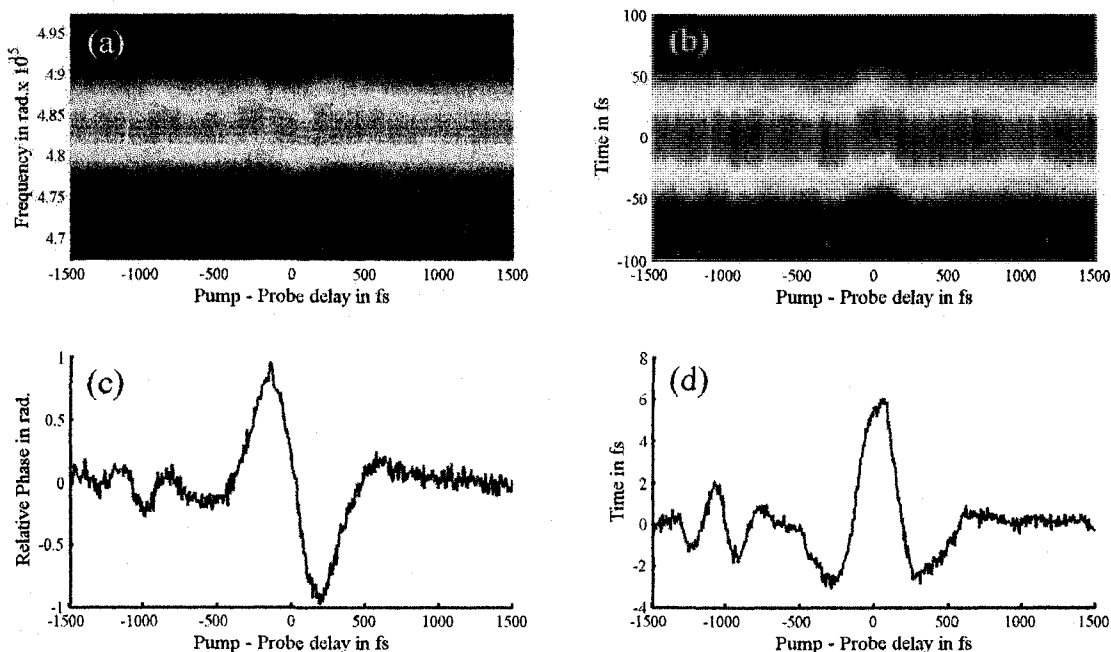


Figure 5.8: (a) The measured interferogram between the probe and reference pulses after propagation through the fiber which was filled with CO_2 at 80 Torr. (b) shows the sideband found by inverse-Fourier transforming the interferogram. (c) and (d) show the phase extracted from the sideband and its centroid, respectively.

be expected for a dilute gas. The maximum change in probe-reference pulse spacing is about 20 fs at 240 Torr of CO_2 .

Fig. 5.8(c) as well as Fig. 5.9(c) show clearly that the relative phase accumulated by the probe pulse due to the wave packet is directly proportional to the effective linear susceptibility, and hence, the molecular alignment. This is expected based on the terms found for the induced polarization density in the presence of a rotational wave packet. The change in group velocity due to the wave packet on the other hand is not proportional to the effective susceptibility, rather, it is proportional to either its derivative or integral.

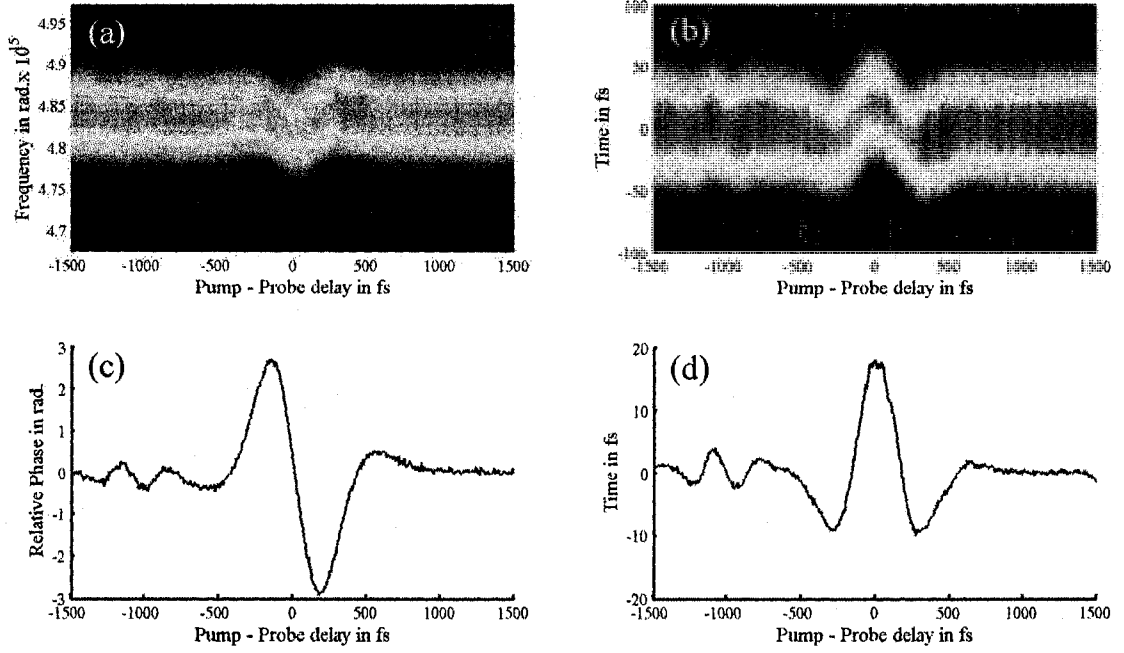


Figure 5.9: (a) shows the spectra, (b) the sideband, (c) the extracted phase, and (d) the centroid of the sideband.

5.3.2 Modelling Group Velocity Modification due to $\chi^{(1)}(\tau)$

The pulse propagation equation was solved again using a split-step approach, with diffraction neglected and dispersion taken into account in the frequency domain and the effect of the molecular alignment in the time domain in the form of an effective linear susceptibility. The two equations are given by

$$\begin{aligned} \frac{\partial \vec{A}(k_x, k_y, \zeta, \omega - \omega_o)}{\partial z} &= \frac{i}{2k_o} \left(\frac{\omega^2}{c^2} \bar{\epsilon}(\omega) - k_o^2 \right) \vec{A}(k_x, k_y, \zeta, \omega - \omega_o) \\ \frac{\partial A_i(\zeta, \tau)}{\partial \zeta} &= \frac{i}{2c^2 k_o} \chi_{ij}^{(1)}(\tau - \tau_{PD}) \frac{\partial^2 A_j(\zeta, \tau)}{\partial \tau^2} + \frac{i}{c^2 k_o} \frac{\partial \chi_{ij}^{(1)}(\tau - \tau_{PD})}{\partial \tau} \frac{\partial A_j(\zeta, \tau)}{\partial \tau} \\ &+ \frac{\omega_o}{c^2 k_o} \chi_{ij}^{(1)}(\tau - \tau_{PD}) \frac{\partial A_j(\zeta, \tau)}{\partial \tau} + \frac{\omega_o}{c^2 k_o} \frac{\partial \chi_{ij}^{(1)}(\tau - \tau_{PD})}{\partial t} A_j(\zeta, \tau) \\ &+ \frac{i}{2c^2 k_o} \frac{\partial^2 \chi_{ij}^{(1)}(\tau - \tau_{PD})}{\partial \tau^2} A_j(\zeta, \tau) - \frac{i\omega_o^2}{2c^2 k_o} \chi_{ij}^{(1)}(\tau - \tau_{PD}) A_j(\zeta, \tau) \end{aligned}$$

We take into account the fact that the central frequency of the probe is twice that of the pump pulse, which means that there will be a change in the pump-probe delay with propagation of the probe due to the gas dispersion. While gas dispersion is very weak, the probe pulse nevertheless will not sample the same molecular alignment throughout, but there will be a small walk-off. Over about 20 cm of fiber length this walk-off due to dispersion amounts to roughly 15 fs. This is very little walk-off considering that the effective linear susceptibility varies very slowly compared to the pulse duration, so that the changes in the effective susceptibility, and in turn the polarization density induced by the probe pulse, are very small. While the solution of this propagation equation using a split-step propagator is only an approximation, it should be accurate enough to model the pulse propagation for a weak probe pulse and a relatively weak coherence where the non-linear polarization density can be assumed small compared to the linear propagation density. Below, we show the results obtained from this model. We have assumed plane wave propagation in a capillary with a diameter of 150 μm , a length of 12 cm and gas pressures ranging from 50 to 300 Torr. The results of simulation for a pump-probe delay of $21.4 \pm 1\text{ps}$ is shown in Fig. 5.10, i.e., the modulation seen is due to the half revival of the rotational wave packet. The results shown are the spectral interferogram (panel (a)), the sideband obtained by inverse Fourier-transforming the spectra (panel (b)), the phase obtained from Fourier-transforming the sideband (panel (c)), as well as the centroid of the sideband (panel (d)). The probe-reference delay is 2 ps, and the gas pressure in this case is 300 Torr. The phase difference accumulated is proportional to $\chi^{(1)}(\tau)$, as expected and observed in the experiment. The change in the group velocity seen from the simulation is also proportional to the effective linear susceptibility. While the model captures the nature of the interaction, there is no qualitative agreement with the experiment regarding the functional dependence on the effective linear susceptibility. This discrepancy between theory and experiment has so far not been resolved and

comes as a bit of a surprise, since the other propagation effects attributed to $\chi^{(1)}(\tau)$ have been readily observed.

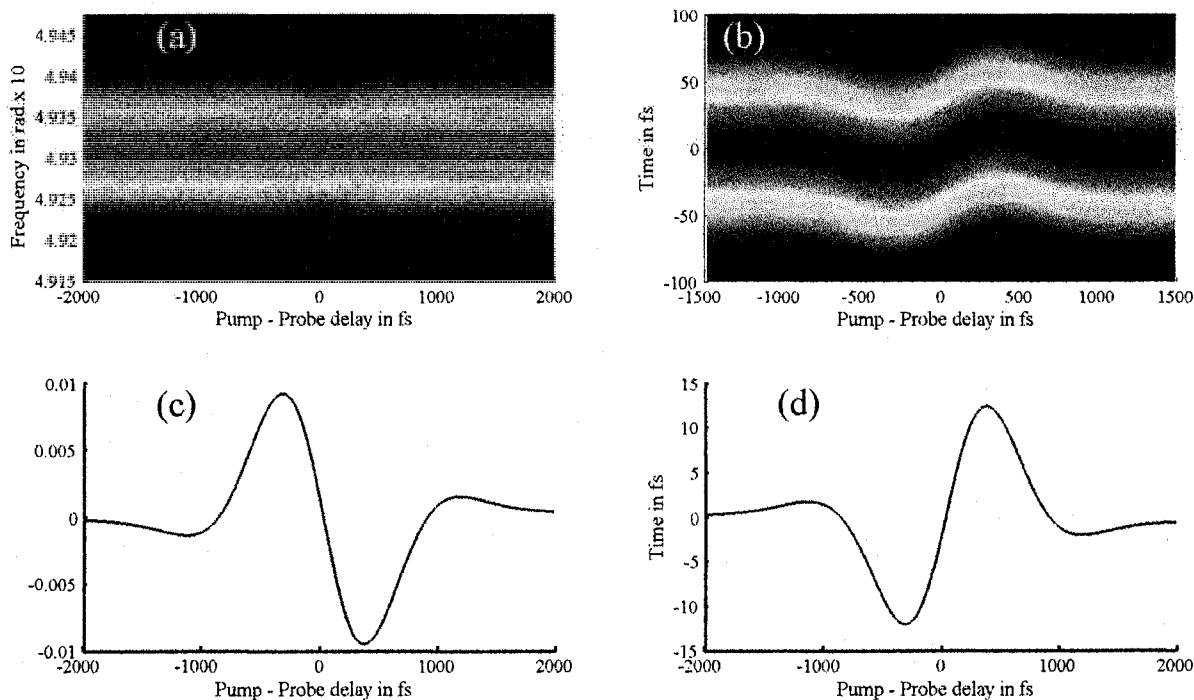


Figure 5.10: (a) shows the calculated interferogram, (b) the extracted sideband, (c) the phase extracted from the sideband, and finally (d) shows the centroid of the sideband

5.4 Transient Birefringence in a gas - A Transient Waveplate

The transient birefringence present in a gas during the revivals of a rotational wave packets can be utilized as a wave plate, like any other birefringent medium. While propagation of polarized pulses through regular birefringent media, e.g. a crystal, is well understood, there are additional "features" which arise from the time dependence of the phase modulations and which make the Transient Wave Plate (TWP) an interesting application of molecular alignment. Previously, when people were using

this effect in order to observe the revivals of the wave packet they were doing so using a linearly polarized probe pulse and a crossed analyzer [45] and were limited to the regime of weak temporal phase modulation where the accumulated phase change $\Delta\phi \ll 2\pi$ across the duration of the pulse. The effects on ultrashort laser pulses due to the propagation through a transient wave plate in a strong phase modulation regime ($\Delta\phi \gg 2\pi$) deviate substantially from those in a birefringent crystal. A detailed understanding of the spectral and polarization evolution of a probe pulse modulated by weak, medium, and strong phase accumulation is detailed below, and is important for probing strong quantum beating phenomena [100] and pulse shaping through molecular modulation [13, 101]. Further developments in pulse shaping with propagation in non-time-stationary optical media may find application in quantum coherent control [102, 103, 104].

Probe pulses with a linear polarization at an arbitrary angle relative to the eigenpolarization directions of the TWP are considered. In this regime, a *single input probe pulse* splits into *two nearly distinct, orthogonally polarized output laser pulses* due to substantial spectral changes accumulated during propagation. The two output pulses adopt the eigenpolarization directions of the TWP, suggesting that polarization splitting can be used to determine eigenpolarization directions. Eigenpolarization measurements for a given propagation direction are related to the principal transient susceptibility frame through a rotational transformation for most gases. Thus, these measurements will be useful for studying transient susceptibility tensors created by complex pump pulses. In contrast, previous weak phase modulation experiments observe a modification of the polarization state of a *single pulse*.

5.4.1 Experimental Setup

The experiment, shown in Fig. 5.11, used ~ 0.8 -mJ, 40-fs, linearly polarized pulses centered at 780 nm which are produced by a single-stage, multi-pass Ti:sapphire

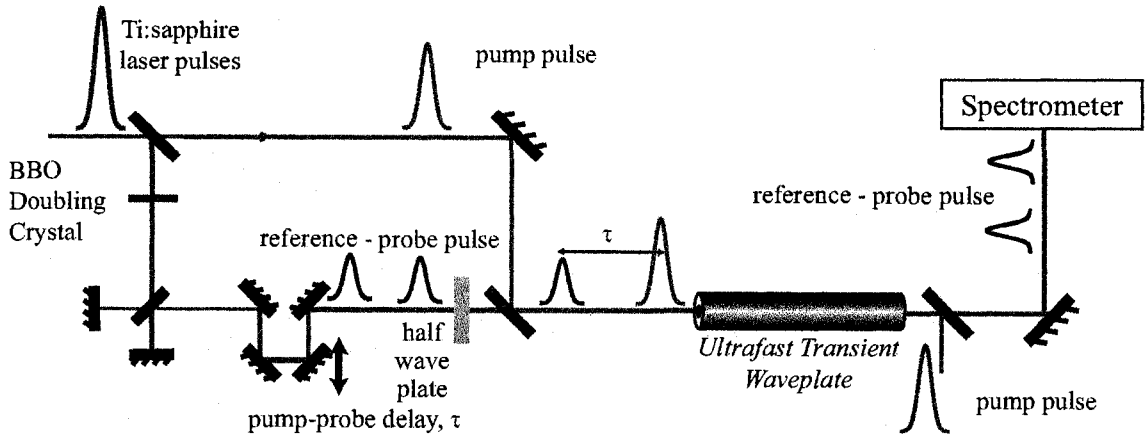


Figure 5.11: Pump - probe setup for observation of polarization splitting.

amplifier system[105]. Approximately 10% of the incident pulse energy is split off and frequency doubled with a 150- μm thick BBO crystal to form the weak probe pulse centered at 390 nm with a FWHM spectral width of $\Delta\lambda \approx 7$ nm. The probe pulse is delayed with respect to the pump pulse by τ_o . The remaining pulse energy constitutes the pump pulse. Both pulses are focused into a 15-cm long, 150 μm diameter hollow-core fiber filled with up to 620 Torr of CO_2 gas. The pump pulse creates a rotational wave packet at time-zero (i.e., $\tau_o = 0$) which exhibits full revivals with a ~ 42 ps period. Transient wave plates at the quarter ($\tau_o \equiv \tau_{1/4} = 10.7$ ps) and half ($\tau_o \equiv \tau_{1/2} = 21.4$ ps) revivals were studied. At the fiber output, the probe pulse is separated from the pump pulse with a dichroic beam splitter. After passing through an analyzing polarizer set at an angle η relative to \hat{z} , the probe spectrum is measured with a spectrometer.

5.4.2 Theory

The probe and pump pulses propagate through the transient wave plate along $-\hat{x}$, which is a principal direction of the TWP. Thus, the remaining eigenpolarization directions are along \hat{y} and \hat{z} . The linear polarization of the probe pulse is adjusted to be at an angle θ with respect to the pump pulse polarization direction, \hat{z} . The probe

pulse can be written as

$$\vec{\mathcal{E}}_{\text{in}}(\tau - \tau_o) = E_o(\tau - \tau_o)e^{i\omega_o(\tau - \tau_o)}\{\hat{y} \sin \theta + \hat{z} \cos \theta\},$$

where $E_o(\tau - \tau_o)$ is the slowly varying temporal envelope of the probe pulse in the rest frame of the pump pulse, delayed by τ_o , and ω_o is the central frequency. The TWP can then be treated as

$$\vec{\mathcal{E}}_{\text{out}}(\tau - \tau_o) = \mathbf{W}(\tau)\vec{\mathcal{E}}_{\text{in}}(\tau - \tau_o),$$

where $\mathbf{W}(\tau)$ is a diagonal matrix with the phase accumulated through propagation along each eigenpolarization direction.

The index of refraction for each principal direction is then given by

$$n_{ii}(\tau) \approx 1 - \chi_{ii}(\tau)/(2\epsilon_o),$$

where $i \in \{\hat{x}, \hat{y}, \hat{z}\}$ indicates a principal direction unit vector, $\chi_{ii}(\tau)$ is an element of the transient susceptibility tensor[106], and we have assumed a dilute, non-absorbing gas. A probe pulse with vacuum wavenumber $k_o = \omega_o/c$ propagating in a TWP of length L accumulates a temporal phase given by

$$\Phi_{ii}(\tau) = k_o n_{ii}(\tau)L.$$

In these experiments, the spectral envelope of the probe pulse is not significantly distorted which implies that the probe pulse duration is short enough that we may approximate the transient phase modulation to be linear during the probe pulse. Thus, we expand $\Phi_{ii}(\tau)$ about the probe pulse delay τ_o to first order, giving

$$\Phi_{ii}(\tau) \approx \Phi_{ii}(\tau_o) + \Phi'_{ii}(\tau_o)\tau,$$

where $\Phi'_{ii}(\tau_o)$ is the slope of the transient phase modulation at the pump-probe delay τ_o , and $\Delta\phi = \Phi'_{ii}(\tau_o)\tau_p$ is the phase accumulated across the pulse. In this approximation, the spectra are sheared by $\Phi'_{ii}(\tau_o)$ and can be written as

$$\vec{\mathcal{E}}_{\text{out}}(\Omega) = \hat{y} (\sin \theta e^{-i\Phi_{yy}(\tau_o)} E_o [\Omega + \Phi'_{yy}(\tau_o)]) + \hat{z} (\cos \theta e^{-i\Phi_{zz}(\tau_o)} E_o [\Omega + \Phi'_{zz}(\tau_o)]),$$

where $E_o(\Omega)$ is the input probe pulse spectrum with $\Omega = \omega - \omega_o$.

The measured probe spectrum after a polarization analyzer at angle η is then given by

$$S(\Omega) = \sin^2 \theta \sin^2 \eta S_y(\Omega) + \cos^2 \theta \cos^2 \eta S_z(\Omega) + \frac{1}{2} \sin 2\theta \sin 2\eta \sqrt{S_y(\Omega)S_z(\Omega)} \cos [\Delta\Phi_{zy}(\tau_o)],$$

with the \hat{y} -polarized and \hat{z} -polarized spectra written as

$$S_y(\Omega) = |E_o [\Omega + \Phi'_{yy}(\tau_o)]|^2$$

and

$$S_z(\Omega) = |E_o [\Omega + \Phi'_{zz}(\tau_o)]|^2,$$

respectively. The birefringence of the TWP at time-delay τ_o is given by $\Delta\Phi_{zy}(\tau_o) = \Phi_{zz}(\tau_o) - \Phi_{yy}(\tau_o)$.

The three different regimes of phase accumulation are illustrated in Fig. 5.12. When the phase modulation is weak, there is very little spectral shifting for the y and z -components of the field, and the resulting output spectrum is almost identical to the input spectrum. In this case, illustrated in Fig. 5.12(a), the polarization state of the pulse evolves just like it would during propagation in a birefringent medium. I.e., in this regime the gas acts precisely like a wave plate. Since the alignment is time dependent, the phase difference accumulated between the y - and z - components

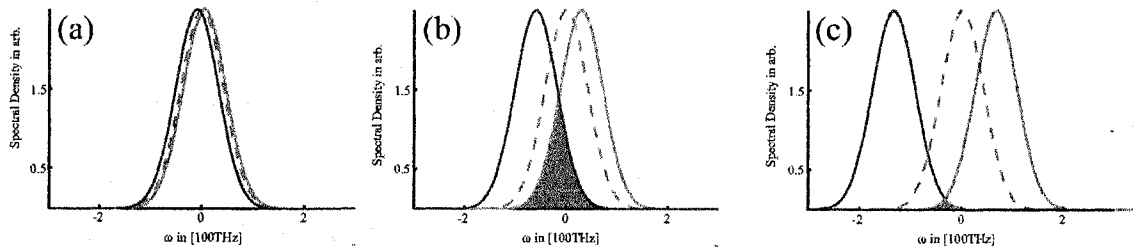


Figure 5.12: (a) Weak phase modulation, (b) moderate phase modulation (c) strong phase modulation

is a function of pump-probe delay. Hence, the action of the gas on a pulse can be described as that of a Transient Wave Plate.

For moderate phase modulation the spectral components along \hat{y} and \hat{z} are partially separated due to the spectral shift. The remaining overlapping part of the spectra continues to evolve in its polarization state, determined by the accumulated phase difference. The non-overlapping spectral components, however, are no longer affected by the phase difference between \hat{x} and \hat{z} since these components are no longer present along both \hat{x} and \hat{z} . In other words, the non-overlapping components of the spectra are linearly polarized along the eigenpolarization directions.

When the phase modulation is strong enough, the spectral components can be separated completely. In this case, the pulse has been split into two pulses with distinct spectral content which are orthogonally polarized along the eigenpolarization directions. The eigenpolarization directions are given in a straightforward manner in case of a single linearly polarized pump pulse. For a more complex excitation scheme, e.g., several arbitrarily polarized pump pulses, this may not be the case. The structure of the effective linear susceptibility tensor may not be immediately obvious. In that case, the observed pulse splitting along the eigenpolarization directions will prove useful for the determination of the eigenpolarization directions, and hence, provide some insight into the symmetry and structure of the tensor.

5.4.3 Weak phase modulation

As explained above, in the weak phase limit there is only negligible frequency shifting along the eigenpolarization directions. Therefore, the spectra of the pulses propagating along \hat{y} and \hat{z} may be considered identical, and the polarization state of the output pulse spectrum will evolve with $\Delta\Phi_{zy}(\tau_0)$. The phase accumulated along \hat{z} due to the wave packet is twice as much as that accumulated along \hat{y} and of opposite sign. This can be seen from the susceptibility tensor elements $\chi_{xx}(\tau)$ and $\chi_{zz}(\tau)$, which are given by

$$\chi_{xx}(\tau) = N \left(\alpha_{\perp} + \frac{1}{2} \Delta\alpha \right) - \frac{1}{2} N \Delta\alpha \langle \langle \cos^2 \theta(\tau) \rangle \rangle$$

and

$$\chi_{zz}(\tau) = N \alpha_{\perp} + N \Delta\alpha \langle \langle \cos^2 \theta(\tau) \rangle \rangle$$

for a single, linearly polarized pump pulse.

The phase accumulated due to the rotational wave packet along \hat{y} and \hat{z} has been measured, respectively, using spectral interferometry, as indicated in the experimental setup. The pump-probe delay is centered around $\tau_{1/4} = 10.6$ ps, which delays the probe and reference pulse-pair to coincide with the quarter revival of the rotational wave packet in CO_2 . The resulting phase, extracted from the interferogram, as a function of pump-probe delay is shown in Fig. 5.13(a). The dashed blue curve shows the relative phase accumulated along \hat{z} , while the solid green curve shows that along \hat{y} . The interaction length of the probe pulse with wave packet is $L = 15$ cm at a gas pressure of 57 Torr. The opposite sign and magnitudes of the phase accumulated due to the wave packet is clearly visible and also shows that the spectral shifting occurring due to $\Phi'_{yy}(\tau)$ and $\Phi'_{zz}(\tau)$ will be in opposite directions, as illustrated in Fig. 5.12. Also indicated in Fig. 5.13(a) is $\Delta\Phi$ at the center of the quarter revival, which is approximately equal to π . Therefore, the gas acts as a half wave plate at that delay.

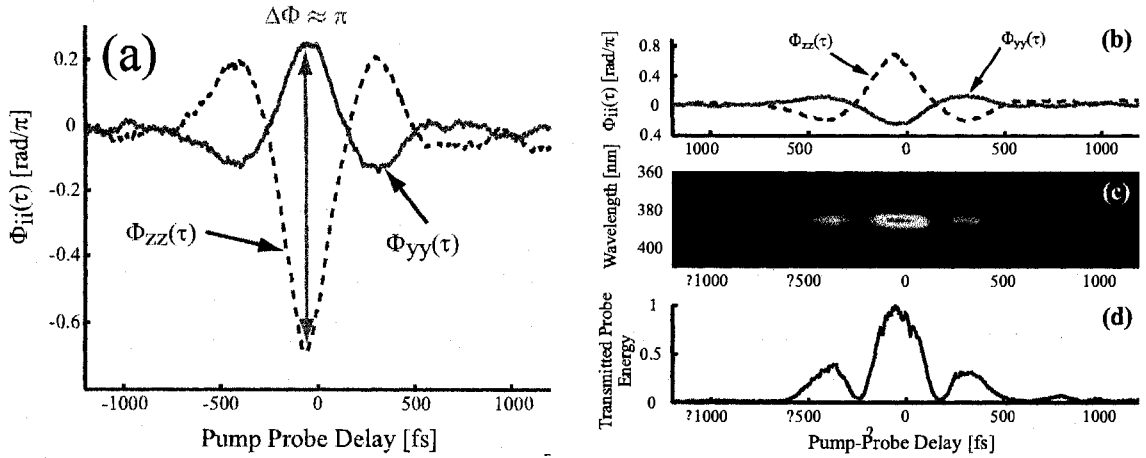


Figure 5.13: (a) Measured temporal phase modulation along \hat{y} (solid) and \hat{z} (dashed) of the TWP for a propagation direction of $-\hat{x}$ at the quarter revival of the wave packet at a pressure of 57 Torr. (b) Probe spectra recorded after a crossed analyzer. (c) Probe energy transmitted through the analyzer.

This effect has been confirmed by carrying out a pump-probe experiment with a single probe pulse at the same pressure and for the same interaction length. The probe pulse spectrum has been observed after a crossed analyzer. The result of this measurement is shown in Fig. 5.13(c), with the accumulated phase along \hat{y} and \hat{z} plotted in panel (a) in order to facilitate comparison. The transmitted energy through the analyzer is almost zero away from the revival. The phase difference accumulated during the revival leads to a change in the polarization state of the probe pulse, which consequently leads to some energy leaking through the polarizer. At the center of the revival, the energy leaking through the polarizer, plotted in Fig. 5.13(d) vs. pump-probe delay, is at a maximum. The TWP rotates the linear polarization of the probe pulse by $\approx 90^\circ$, acting as a half-wave plate.

5.4.4 Moderate phase accumulation

Increasing the gas pressure to 570 Torr moves the TWP into a regime of moderate temporal phase modulation, i.e., the spectral shear $\Phi'_{ii}(\tau_0)$ along \hat{y} and \hat{z} respectively is significant, however, not large enough to completely separate the spectra. Probe

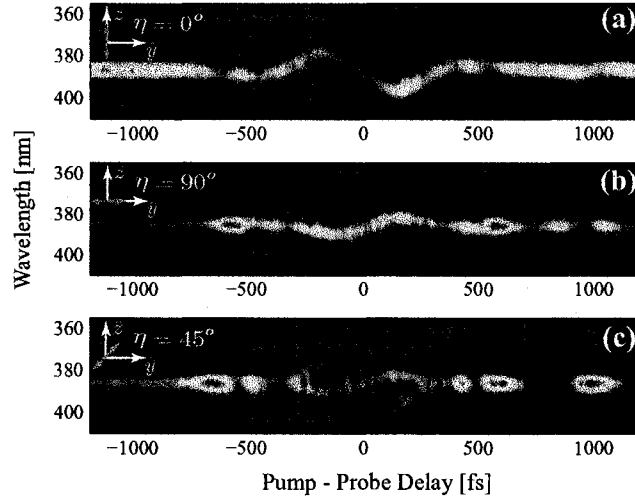


Figure 5.14: Probe spectra measured after an analyzing polarizer near the quarter revival at 570 Torr. The spectral shear along the eigenpolarization directions is shown in (a) for \hat{z} and in (b) for \hat{y} , respectively. (c) shows the modulation of the overlap spectra due to the birefringence for $\eta = 45^\circ$.

spectra recorded for $\theta = 45^\circ$ and various analyzer angles η with pump-probe delays ranging over $\tau_{1/4} \pm 1$ ps are shown in Fig. 5.14. The probe pulse spectra resolved along the eigenpolarization directions with the polarizer oriented at $\eta = 0^\circ$; (\hat{z}) and $\eta = 90^\circ$; (\hat{y}) are shown in Fig. 5.14(a) and Fig. 5.14(b), respectively. The spectra recorded for $\eta = 45^\circ$ can be seen in Fig. 5.14(c). In these data, we observe a modulation in the energy of the transmitted spectrum for those regions with residual spectral overlap between S_y and S_z . This is attributed to the change in their polarization state as a result of $\Delta\Phi_{zy}(\tau_o)$. However, those spectral components, which are *not* present along *both* eigenpolarization directions, emerge *linearly polarized along the respective eigenpolarization direction*. Hence, the transmission of those non-overlapping spectral components is determined solely by the projection onto the analyzer, as shown in Fig. 5.14(c).

5.4.5 Strong Phase Modulation

When the spectral shear is large enough so that the spectra of the pulses along each eigenpolarization direction have no overlap, the transient wave plate splits the probe pulse into two orthogonally polarized pulses. Measurements of this phenomenon of polarization pulse splitting at a half revival of CO₂ for a gas pressure of 620 Torr are shown in Fig. 5.15. The initial probe pulse spectrum is shown as (a) in the upper line of Fig. 5.15. The spectra of the pulses exiting the fiber are shown in the bottom line of Fig. 5.15, and are measured with the analyzer oriented parallel (b) and perpendicular (c) to the pump polarization. The output spectra are found to be linearly polarized and orthogonal — having adopted the eigenpolarization directions of the TWP. The output spectra have a mutual overlap of $f < 0.11$. The mutual overlap specifies the fraction of residual spectral overlap and is defined as $f = \int S_y(\Omega)S_z(\Omega)d\Omega / \sqrt{\int S_y^2(\Omega)d\Omega \int S_z^2(\Omega)d\Omega}$. These data demonstrate nearly complete splitting of the probe pulse into two orthogonally polarized pulses with negligible spectral overlap.

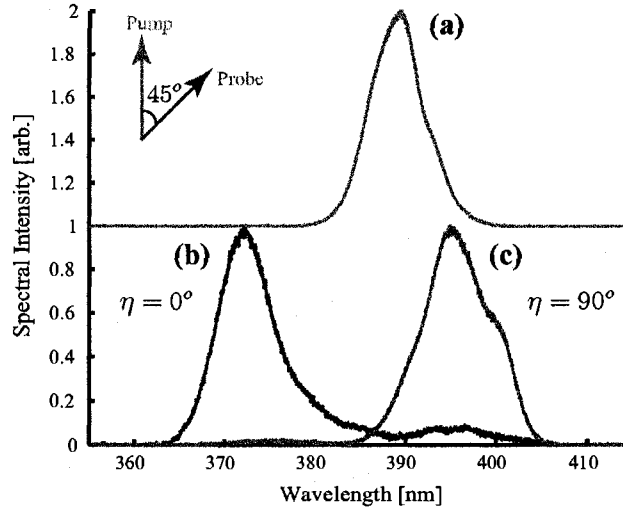


Figure 5.15: Measurement of pulse polarization splitting. (a) The reference spectrum is the probe spectrum incident on the TWP. The \hat{z} -pulse (b) and \hat{y} -pulse (c) output spectra are measured with an analyzer parallel and perpendicular to the pump polarization direction, respectively.

5.4.6 Summary

We have demonstrated a new pulse splitting effect that occurs when an ultrafast laser pulse propagates through a transient wave plate. When the pulse enters the wave plate with a polarization that is not coincident with an eigenpolarization direction of the medium, the probe pulse will be split into two distinct, orthogonally polarized laser pulses at the exit of the wave plate in the strong phase modulation limit. The directions of polarization of those two pulses are along the eigenpolarization directions of the transient medium for most molecular gases. The principal frames for the linear susceptibility tensor and alignment are commensurate[106], thus this technique is useful for measuring the principal frame of reference regarding the alignment of anisotropic molecules. Techniques for probing transient birefringent dynamics are important for studying molecular modulators and wave packet dynamics in systems where a large phase modulation is imparted on a probe pulse. Resolution of the eigenpolarization directions is critical for the study of transient wave plates excited by complex excitation schemes, where the direction of the eigenpolarizations of the resulting birefringent medium is not obvious. Moreover, this approach may be generalized to measure the nonlinear contributions of the wave packet to the time-varying susceptibility tensor with either transient birefringent[15] or quasi phase matching[18].

Chapter 6

Non-linear optical frequency conversion

Efficient, broad bandwidth nonlinear optical frequency conversion is of strong interest for producing ultrafast light sources, particularly at short wavelengths. Recently, interest has been rapidly growing in the area of nonlinear frequency conversion in the presence of coherent nuclear state dynamics. An adiabatically excited vibrational transition has been used for the generation of a frequency comb ranging from the mid IR to the UV[107], while impulsively excited rotational wave packets have been shown to modulate a highly non-linear frequency conversion process, namely high-order harmonic generation (HHG)[108, 109]. These HHG studies show a dependence between the re-collision dynamics of the electrons and the nuclear coherence excited by a pump pulse [14]. Coherent nonlinear frequency conversion in the presence of transient alignment produced by a rotational wave packet shows promise as a powerful spectroscopic tool.

Improving the efficiency of coherent non-linear frequency conversion is an important aspect of non-linear optics. Common phase matching configurations exploit crystal birefringence [72, 73], dispersion of resonances [110, 111], and waveguide dis-

persion [35, 84]. Efficient frequency conversion of intense, broad bandwidth ultrafast laser pulses presents a challenge for conventional phase matching techniques. The dispersion, transparency range, and damage threshold of bulk materials prevents efficient conversion to the UV for energetic ultrafast laser pulses. Difference frequency mixing in hollow waveguides demonstrated efficient conversion from frequency doubled 800-nm pulses, mixed with a weak IR pulse to generate short UV pulses [112]. Techniques for exploiting transiently induced birefringence in a molecular gas [15, 18] for efficient third harmonic generation (THG) have been presented. Recently, efficient third and fifth harmonic radiation generated by IR and UV fundamental ultrafast pulses propagating in filaments has been reported [113, 114].

In Sec. 6.1 we present third harmonic generation in the presence of coherent rotational as well as vibrational motion which manifests itself as a modulation in the conversion efficiency from the fundamental to the third harmonic. Rotational motion is detected with this technique in CO_2 and N_2O , while SF_6 is used to observe the effect of vibrational motion. Sec. 6.2 focusses on the observation of an enhanced conversion efficiency due to a laser-induced plasma at the focus of a relatively weak probe pulse. The enhancement is observed in a variety of molecular as well as atomic gases.

6.1 Third Harmonic Generation in the presence of a rotational wave packet

In this section, we study changes in coherent third harmonic generation (THG) induced by a rotational wave packet in a molecular gas. We observe a modulated third harmonic conversion efficiency and study its dependence on the molecular alignment, which produces perturbations to both the effective linear and third order susceptibility. We performed pump-probe experiments with an energetic pump pulse that excites

a broad rotational wave packet in a room-temperature molecular gas. The third harmonic radiation generated by a time-delayed probe pulse with a fraction of the pump energy is seen to be modulated as a function of pump-probe delay, τ , during revivals of the rotational wave packet. For off-resonance interactions, the macroscopic optical response in the presence of a rotational wave packet, linear as well as non-linear, can be described by means of an effective susceptibility[29]. The dependence of both the effective linear as well as third order susceptibility on the molecular alignment impacts the THG conversion efficiency. To understand the strength of the relevant contributions to the measured data, we developed a model of the nonlinear interaction and made detailed comparisons to our experimental data.

6.1.1 Theory of Third Harmonic Generation in the presence of a rotational wave packet

It has been shown that the third order non-linear response of an ensemble of molecules can be described as effectively time-varying and that there are only three independent non-zero elements of the second hyper-polarizability tensor for molecules of symmetry D_{∞} , e.g., linear molecules. In general, the non-linear interaction between a linearly polarized field and a molecule may result in the scatter of photons into different polarization states. The different possibilities are classified as Type I and Type II processes.

In thermal equilibrium, the optical response of a gas is of course isotropic so that only one Type I THG process exists. However, the alignment induced by a linearly polarized pump pulse breaks this symmetry. The resulting effective linear susceptibility tensor is diagonal in the laboratory frame, which is defined by the pump pulse polarization (\hat{z}) and its propagation direction (\hat{y})[17]. Assuming that the probe pulse propagates collinearly with the pump, the polarization of the probe and third harmonic pulses thus lie in the $\hat{x} - \hat{z}$ plane. For linear molecules aligned by a

Table I: Type I and Type II processes allowed for third order interaction between a linearly polarized field with polarization direction in the $\hat{x}\hat{z}$ -plane

Process	3ω	ω	ω	ω
Type I _x	\hat{x}	\hat{x}	\hat{x}	\hat{x}
Type I _z	\hat{z}	\hat{z}	\hat{z}	\hat{z}
Type II _α	\hat{z}	\hat{z}	\hat{x}	\hat{x}
Type II _α	\hat{z}	\hat{x}	\hat{x}	\hat{z}
Type II _α	\hat{z}	\hat{x}	\hat{z}	\hat{x}
Type II _β	\hat{x}	\hat{x}	\hat{z}	\hat{z}
Type II _β	\hat{x}	\hat{z}	\hat{z}	\hat{x}
Type II _β	\hat{x}	\hat{z}	\hat{x}	\hat{z}

linearly-polarized laser field, four THG processes are allowed: Type I_z and Type I_x, where both the fundamental probe (hereafter fundamental) and third harmonic fields are polarized along \hat{z} and \hat{x} , respectively, and two Type II (α, β) processes with a mix of \hat{z} and \hat{x} polarizations [15]. The detailed interactions are outlined in Table I.

Changes in the index of refraction with respect to the isotropic index \bar{n} due to the wave packet are written as $\delta n_z = N\Delta\alpha(\omega)Q/2\epsilon_o$ and $\delta n_x = \delta n_y = -N\Delta\alpha(\omega)Q/4\epsilon_o$, where $Q = \langle\langle\cos^2\theta(\tau)\rangle\rangle - \frac{1}{3}$ is the change in alignment relative to the isotropic distribution, $\Delta\alpha(\omega) = \alpha_{\parallel}(\omega) - \alpha_{\perp}(\omega)$, and $\bar{n}^2 - 1 = N\bar{\alpha}/\epsilon_o$ and $3\bar{\alpha} = \alpha_{\parallel}(\omega) + 2\alpha_{\perp}(\omega)$. As has been detailed previously, the change in the index of refraction along the principal axes differs by a sign and a factor of two in magnitude, hence, $\delta n_z \neq \delta n_x$, i.e., the gas is birefringent in the $\hat{x} - \hat{z}$ plane.

The non-zero transient effective third order susceptibilities are $\chi_{zzzz}^{(3)}(\tau)$, $\chi_{xxxx}^{(3)}(\tau)$, and $\chi_{aabb}^{(3)}(\tau)$, with permutations of the pairs $a, b \in \{x, z\}$ being equal. We may write the phase mismatch as $\Delta k_z = 3k_z^\omega - k_z^{3\omega}$ and $\Delta k_x = 3k_x^\omega - k_x^{3\omega}$ for the Type I processes.

Along these eigenpolarization directions the phase mismatch is given by

$$\Delta k_x = \frac{3\omega}{c} (\bar{n}(\omega) + \delta n_x(\omega)) - \frac{3\omega}{c} (\bar{n}(3\omega) + \delta n_x(3\omega))$$

which can be written in term of an isotropic phase mismatch $\Delta \bar{k}$ as

$$\Delta k_x = \Delta \bar{k} + \frac{3\omega}{c} (\delta n_x(\omega) - \delta n_x(3\omega))$$

with $\delta n_x(\omega)$ defined above. From this it can be seen that the phase mismatch for Type I interactions is unaffected by the molecular alignment for negligible dispersion in $\Delta \alpha(\omega)$ and is then simply the isotropic phase mismatch $\Delta \bar{k} = \Delta k_x = \Delta k_z$. Phase matching Type I interactions is therefore not possible with molecular alignment. The modulation of the third harmonic generated by the probe pulse polarized along \hat{x} or \hat{z} as a function of pump-probe delay is therefore dominated by $\chi^{(3)}(\tau)$. The phase mismatch for Type II $_{\alpha}$ is given by $\Delta k_{II\alpha} = 2k_x^{\omega} + k_z^{\omega} - k_z^{3\omega}$, and for Type II $_{\beta}$, $\Delta k_{II\beta} = 2k_z^{\omega} + k_x^{\omega} - k_x^{3\omega}$. Hence, Type II processes are modulated by molecular alignment both via $\chi^{(1)}(\tau)$ as well as $\chi^{(3)}(\tau)$.

It follows from the above analysis that the THG power conversion for Type I processes is proportional to the square of the effective third harmonic susceptibility given by $P_z^{3\omega}(\tau) \propto |\chi_{zzzz}^{(3)}(\tau)|^2$ and $P_x^{3\omega}(\tau) \propto |\chi_{xxxx}^{(3)}(\tau)|^2$ for $\eta = 0^\circ$ and 90° , respectively, where η is the angle between the pump and probe pulse polarizations. When the probe pulse is incident with $\eta = 45^\circ$, both Type I and Type II processes occur, and the modulation of the THG power is due to a combination of both $\Delta k(\tau)$ and $\chi^{(3)}(\tau)$. The strong modulation observed after a polarizer in this case is largely due to the presence of the birefringence, which changes the polarization state of the third harmonic radiation [34].

6.1.2 Experimental Setup

The experimental setup is depicted schematically in Fig. 6.1(c). The pump and probe pulses for the experiment are derived from a Ti:sapphire amplifier (KMLabs) which delivers 1.2-mJ pulses of 35 fs in duration, centered at 785 nm. A beam splitter separates the output into linearly polarized pump ($\approx 80\%$) and probe ($\approx 20\%$) pulses. The relative polarization angle is adjusted with a half waveplate in the pump arm. The pulses are focused with 50-cm focal length mirror into a gas cell filled with CO_2 gas at pressures from 200 - 700 Torr. Profiling the focusing beams with a knife-edge scan gives a crossing angle of 2° and an interaction length of 1-1.2 cm. The fundamental and third harmonic probe fields are separated with two dielectric mirrors coated for 266-nm (CVI). A calcite polarizer (Thorlabs) with a $\approx 10^5 : 1$ extinction ratio is adjusted to select the THG polarization direction to be recorded by the spectrometer (Ocean Optics USB4000).

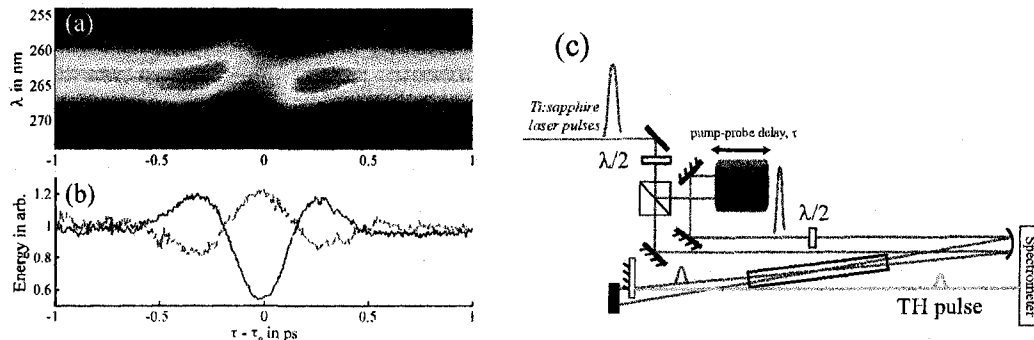


Figure 6.1: (a) Third harmonic spectra recorded for $\eta = 0^\circ$ with the polarizer oriented along the probe pulse polarization at the quarter revival of CO_2 at 600 Torr. (b) Modulation in energy vs. pump-probe delay for both $\eta = 0^\circ$ (blue) as well as $\eta = 90^\circ$ (green).

6.1.3 Results for the modulation of THG due to molecular alignment

To separate the modulation of the conversion efficiency due to variations in the non-linear susceptibility, $\chi^{(3)}(\tau)$ from those in $\chi^{(1)}(\tau)$, we adjusted the fundamental polarization to be either along \hat{z} or \hat{x} to select the two Type I processes. Fig. 6.1(a) shows spectra of the third harmonic generated by the probe pulse as a function of pump probe delay at the quarter revival ($\tau_o \approx 10.6$ ps) of CO_2 . The gas pressure was 600 Torr and $\eta = 0^\circ$. The modulation of energy conversion to the third harmonic is clearly visible, and as can be seen in Fig. 6.1(b) (blue, solid), it is proportional to $\langle\langle \cos^2 \theta(\tau) \rangle\rangle$. While $\chi^{(3)}(\tau)$ depends on both $\langle\langle \cos^2 \theta(\tau) \rangle\rangle$ and $\langle\langle \cos^4 \theta(\tau) \rangle\rangle$, the dependence on $\langle\langle \cos^4 \theta(\tau) \rangle\rangle$ is about one order of magnitude weaker compared to that of $\langle\langle \cos^2 \theta(\tau) \rangle\rangle$. Hence, the modulation for the third harmonic signal at a revival for Type I processes is expected to be dominated by $\langle\langle \cos^2 \theta(\tau) \rangle\rangle$ for these experimental conditions. These data therefore directly show the dependence of Type I THG processes on molecular alignment. This has also been verified for the case of $\eta = 90^\circ$, for which only the modulation in third harmonic energy as a function of pump-probe delay is shown in Fig. 6.1(b) (red, dashed).

More complicated modulation is observed for arbitrary angle between the pump and probe pulses. The case of $\eta = 45^\circ$ has been chosen and is illustrated in Fig. 6.2 for a variety of cases at a gas pressure of 600 Torr. The third harmonic spectra transmitted through the polarizer when it is oriented along the probe pulse polarization are shown in Fig. 6.2(a) at the quarter revival of CO_2 . The modulation observed in this case, as in the ones that follow, is due to the dependence of the linear, as well as the non-linear, susceptibilities of the gas. I.e., both Type I and Type II processes are present. Fig. 6.2 (b) shows the THG energy as a function of pump-probe delay when the polarizer is oriented along (blue, solid) and perpendicular (red, dashed) to the probe pulse polarization in arbitrary units. The same data are shown at the half-

revival of CO₂ in (c) and (d), as well as the half-revival of N₂O in (e) and (f). The energy transmitted through the polarizer as a function of pump-probe delay clearly differs from that observed at the quarter revival, which may be expected since the modulation of $\chi^{(1)}(\tau)$ as well as $\chi^{(3)}(\tau)$ due to the molecular alignment is different. A significant difference between the modulation in CO₂ and that in N₂O is that the spectral components transmitted through the polarized are much more heavily modulated with pump-probe delay. Regarding the detection of the spectra it should be noted that since the grating efficiency of the spectrometer used is not independent of the polarization direction, the signal recorded when the polarizer is oriented orthogonally to the probe pulse polarization is lower than when the polarizer is oriented parallel.

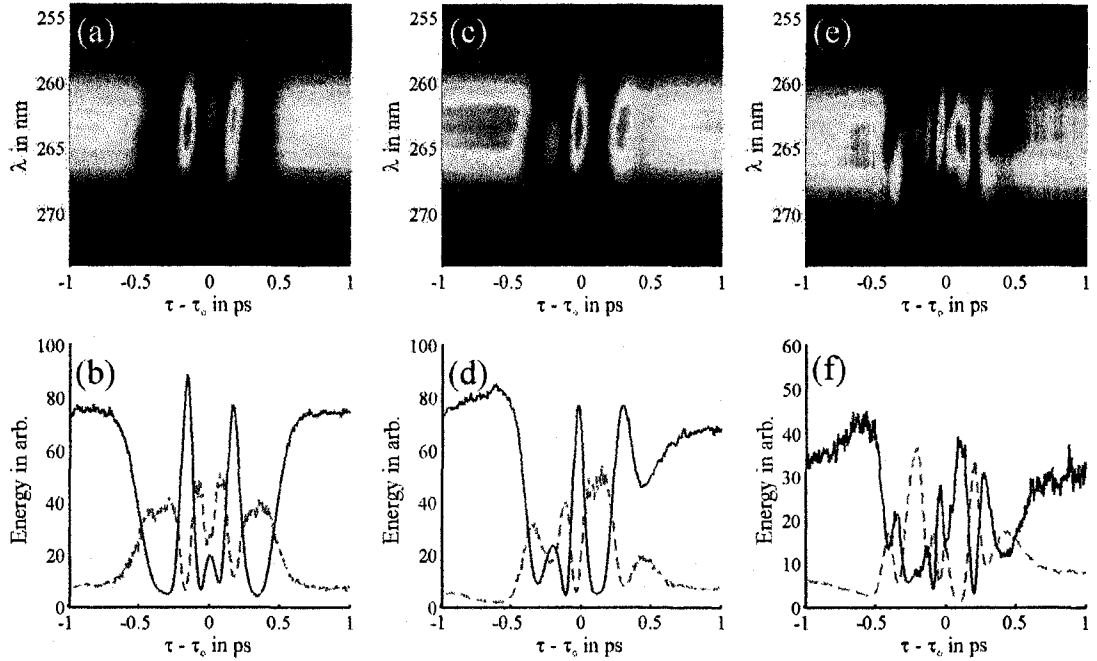


Figure 6.2: Third harmonic spectra recorded for $\eta = 45^\circ$ with the polarizer oriented along the probe pulse polarization at the quarter revival of CO₂ (a), the half revival of CO₂ (c), and the half revival of N₂ (d), all at 600 Torr. (b), (d), and (f) Modulation in energy vs. pump-probe delay for the polarizer oriented along (blue, solid) and orthogonally (red, dashed) to the probe pulse polarization for each case, respectively.

In order to illustrate the different strength of the modulation of the optical re-

sponse of CO₂ and N₂O, Fig. 6.3 compares the modulation observed in CO₂ at the half revival at a gas pressure of 600 Torr to that observed in N₂O at 300 Torr, which are essentially identical. I.e., while the modulation as a function of pump-probe delay at the half-revival is the same for both gases, it is much stronger in N₂O.

This observation may be explained by that fact that the wave packet excitation in N₂O is much more efficient than in CO₂. As a reminder, the interaction Hamiltonian for the excitation of a rotational wave packet by a linearly polarized pulse is given as

$$H_{\text{int}}(\tau) = -\frac{\Delta\alpha}{4}\mathcal{E}^2(\tau)\cos^2\theta,$$

i.e., it is directly proportional to the polarizability anisotropy $\Delta\alpha$. Experimental determination of $\Delta\alpha$ is difficult, and the results vary widely. Here we quote numbers from well-cited sources, which have also been used in the modeling of this experiment. The polarizability anisotropy of N₂O is taken to be [115]

$$\Delta\alpha_{N_2O} = 19.6$$

for N₂O, and [116]

$$\Delta\alpha_{CO_2} = 14.3$$

for CO₂. From these numbers it is immediately obvious that the off-resonance Raman interaction of the pulse with N₂O is roughly one and a half times stronger than with CO₂. The experimental data seems to indicate that the difference in the wave packet strength is about a factor of two between the gases. Given the wide range of numbers available for either polarizability anisotropy, the agreement simply based on the proportionality of the interaction strength between the strength of the phase modulation and the difference in the anisotropies is very good.

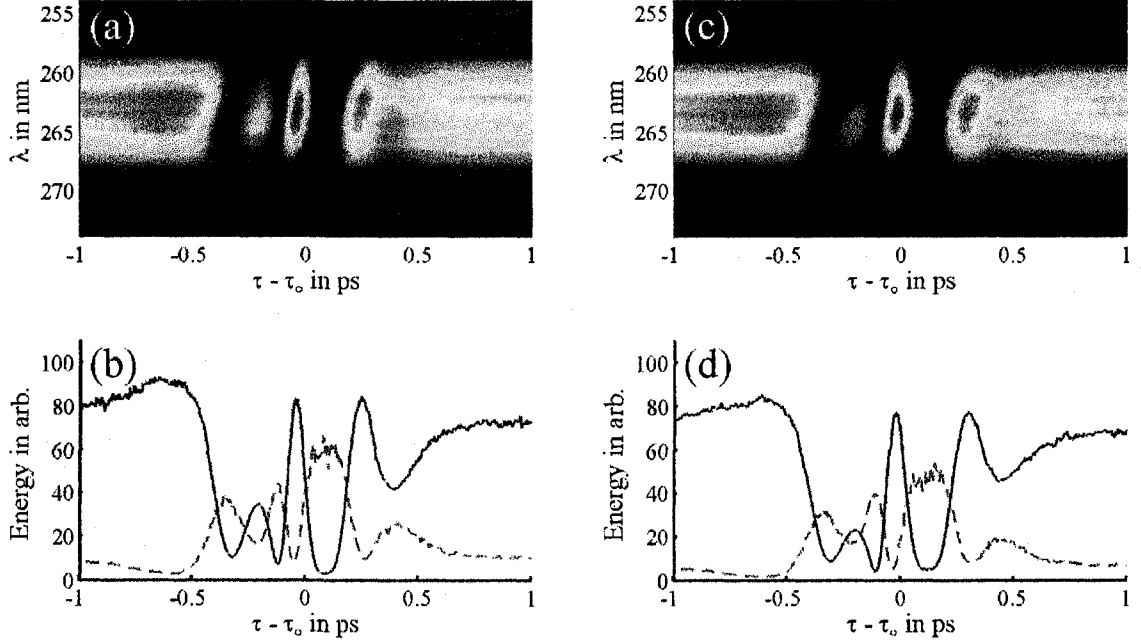


Figure 6.3: (a) Third harmonic spectra recorded for $\eta = 45^\circ$ with the polarizer oriented along the probe pulse polarization at the half revival of N_2O at 300 Torr and (c) TH spectra at the half revival of CO_2 at 600 Torr. (b) and (d) Modulation in energy vs. pump-probe delay for the polarizer oriented along (blue, solid) and orthogonally (red, dashed) to the probe pulse polarization for each case, respectively.

6.1.4 Modeling of the experiment

The experiment has been modeled using a set of coupled equations for the fundamental probe and the third harmonic generated by the probe pulse. In general, the complete field is comprised of the fundamental and third harmonic fields with components along \hat{z} and \hat{x} , given by

$$\vec{\mathbf{E}}(\vec{\mathbf{r}}, t) = \vec{\mathbf{A}}_o(y, t)e^{i(k_o y - \omega_o t)} + \vec{\mathbf{A}}_3(y, t)e^{i(k_3 y - \omega_3 t)},$$

where $\vec{\mathbf{A}}_i(y, t)$ is the complex, slowly varying envelope, k_i is the \hat{y} -component of the wave vector, and ω_i is the central frequency for the fundamental and third harmonic, respectively. The slowly varying envelope for both the fundamental and third harmonic after propagation in a transiently aligned medium can be found by solving a

set of four coupled equations, one for each component of each field. In the slowly varying envelope approximation, the propagation equation for each field component is given by

$$2ik_i \frac{\partial \vec{A}_i(y, t)}{\partial y} + \tilde{D} \vec{A}_i(y, t) = -\mu_o \omega_i^2 \vec{p}_i(y, t),$$

where $\vec{p}_i(y, t)$ is the induced dipole moment density at either the fundamental or third harmonic frequency, including various terms describing SPM, XPM, THG, as well as backconversion from the third harmonic to the fundamental. \tilde{D} is the dispersion operator in the time domain[33]. The propagation equation in the plane-wave limit was solved with a Runge-Kutta-Fehlberg algorithm using a split step approach, where the dispersion was applied in the frequency domain, while the non-linear terms were taken into account for in the time domain.

For the model, the spatial intensity variation along the propagation direction was found assuming a focusing Gaussian beam for both the pump and probe fields with a beam waist of 80 μm at the focus. The peak intensity of the pump pulse at the focal spot was $6 \times 10^{13} \text{W/cm}^2$, that of the probe pulse was $3 \times 10^{13} \text{W/cm}^2$. The duration for both pulses was 35 fs with an interaction length for the probe pulse with the wave packet of 1.2 cm. The CO_2 pressure was 600 Torr and the rotational temperature was 300 K. The rotational wave packet was calculated using an analytic model for the solution of the Schrödinger equation [17] at several locations throughout the interaction length in order to model the varying strength of the wave packet in the focal volume. The result of the calculation for $\eta = 45^\circ$ is shown in Fig. 6.4, where (a) shows the calculated third harmonic spectra and (b) shows the energy in the third harmonic vs. pump-probe delay after a polarizer oriented parallel (solid) and orthogonally (dashed) to the probe pulse polarization. Based on the model, the dependence of $\Delta k(\tau)$ on the molecular alignment dominates the modulation of the conversion efficiency over $\chi^{(3)}(\tau)$ for the Type II processes. The dependence of the conversion efficiency vs. pump-probe delay on the dispersion of $\Delta\alpha$, taken from Ref.

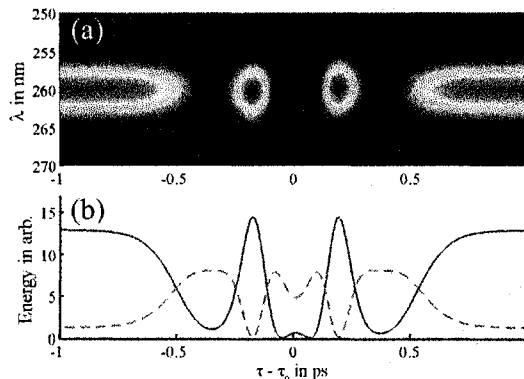


Figure 6.4: (color online) (a) Third harmonic spectra calculated for $\eta = 45^\circ$ at the quarter revival of CO_2 at 600 Torr with a polarizer oriented along the probe pulse polarization. (b) Modulation of the energy vs. pump-probe delay for a polarizer oriented along (blue, solid) and orthogonally (red, dashed) to the probe pulse polarization.

[117], is very weak, and can be neglected for the given experimental accuracy.

6.1.5 Modulation of THG due to coherent vibrational motion

A modulation of the conversion efficiency of THG can also be observed for coherent *vibrational* motion. The analysis follows that described in the previous section. The dependence of $\chi^{(3)}(\tau)$ and $\chi^{(1)}(\tau)$ is, of course, no longer determined by $\langle\langle \cos^2 \theta(\tau) \rangle\rangle$. Instead, the vibrational wave packet resulting from off-resonant impulsive, stimulated Raman scattering determines the time dependence of the polarizability. The induced dipole moment density relevant to the modulation of THG, to first order in perturbation due to the electric field, can be expressed as

$$P_i^{(5)}(t) = -\frac{1}{\hbar} E_j(t) E_k(t) E_l(t) \sum_q P(q) \sum_n \langle q | \gamma_{ijkl} | n \rangle \langle n | \alpha_{mn} | q \rangle \int_0^\infty d\tau \sin(\omega_{qn}\tau) E_m(t-\tau) E_n(t-\tau)$$

This shows that the interaction under investigation may be viewed as a scattering

process effectively of fifth order in the field, however it is not a direct fifth order process. The interaction may be viewed as a stimulated Raman scattering event followed by second hyper-Raman scattering, where the two processes are well separated in time. This point of view is equivalent to the approach taken earlier when describing the modulation of THG due to a rotational wave packet, i.e., utilizing an effective third order susceptibility which is time dependent due to the wave packet present. This effective third order susceptibility for a vibrational coherence is then given by

$$\chi_{ijkl}^{\text{vib}}(t) = -\frac{N}{\epsilon_0 \hbar} \sum_q P(q) \sum_n \langle q | \gamma_{ijkl} | n \rangle \langle n | \alpha_{mn} | q \rangle \int_0^\infty d\tau \sin(\omega_{qn}\tau) E_m(t - \tau) E_n(t - \tau)$$

so that the induced dipole moment density can be formally written as

$$P_i^{(3)} = \epsilon_0 \chi_{ijkl}^{(3)}(t) E_j(t) E_k(t) E_l(t)$$

in the Born-Oppenheimer approximation. With that, the modulation of THG due to coherent nuclear motion is equivalent for vibrational and rotational motion.

6.1.5.1 Modulation of THG in SF₆

In order to confirm this experimentally, the experiment described above has been repeated using SF₆. SF₆ has a fully symmetric vibrational mode at about $\nu = 23.56$ THz, which corresponds to a vibrational period of $\tau_\nu \approx 42$ fs. With 40 fs the pulse duration of the pump pulse is close to this period, however, the interaction is strong enough to result in a coherent excitation of this transition and an observable modulation of the THG. With the experimental parameters being very similar to those described in the previous section, the third harmonic spectra have been recorded with a spectrometer and are shown in Fig. 6.5(a). A sinusoidal modulation of the energy in the third harmonic is clearly observable, and is shown in Fig. 6.5(b). A Fourier transform of the energy modulation is shown in panel (c), and clearly shows

a sideband located at around 23 THz, which indicates that the modulation observed is indeed due to the fully-symmetric Raman mode of SF₆.

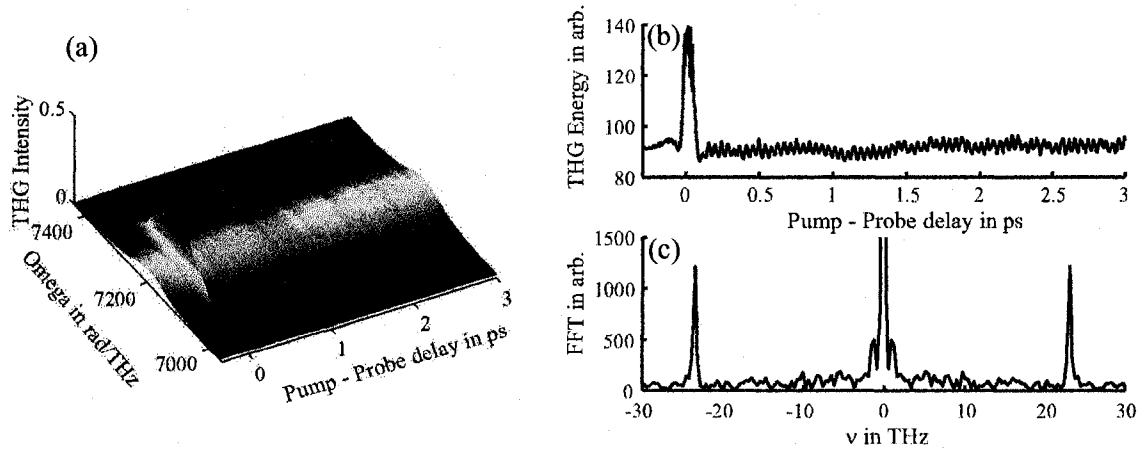


Figure 6.5: SF₆ at 600 Torr, pump power 780 mW, probe power 180 mW

6.1.6 Concurrent detection of effective linear and nonlinear susceptibility contribution

Using the co-linear setup used in Sec. 5.4 with some slight variations allows us to measure both the relative phase accumulated by the probe pulse due to the effective linear susceptibility, as well as the modulation of the third harmonic conversion efficiency. First, we replace the capillary with a gas cell filled with CO₂ at 150 Torr. Secondly, we insert a 10% beam splitter at normal incidence in the probe arm. The beam splitter is placed closely to the highly reflective mirror, so that the path difference between the surface facing the polarizing beam cube and the mirror amounts to a delay of about 1.8 ps. This will generate a train of weak pulses due to the reflections off of the beam splitter, the first pulse of the train spaced by 1.8 ps from the probe pulse. The weak pulse train is not strong enough to generate any third harmonic. It is, however, possible to detect interference between the weak pulses immediately preceding and following the probe pulse and the probe pulse itself. The third harmonic generated by the probe pulse is separated from the fundamental by a mirror which is highly

reflective around 266 nm and detected using an Ocean Optics USB4000 spectrometer, while the fundamental is detected using an Ocean Optics USB2000 spectrometer at the same time. The intensity variation in the third harmonic is clearly visible, and the relative phase between the probe and reference pulses can be extracted from the interferograms recorded as a function of pump-probe delay.

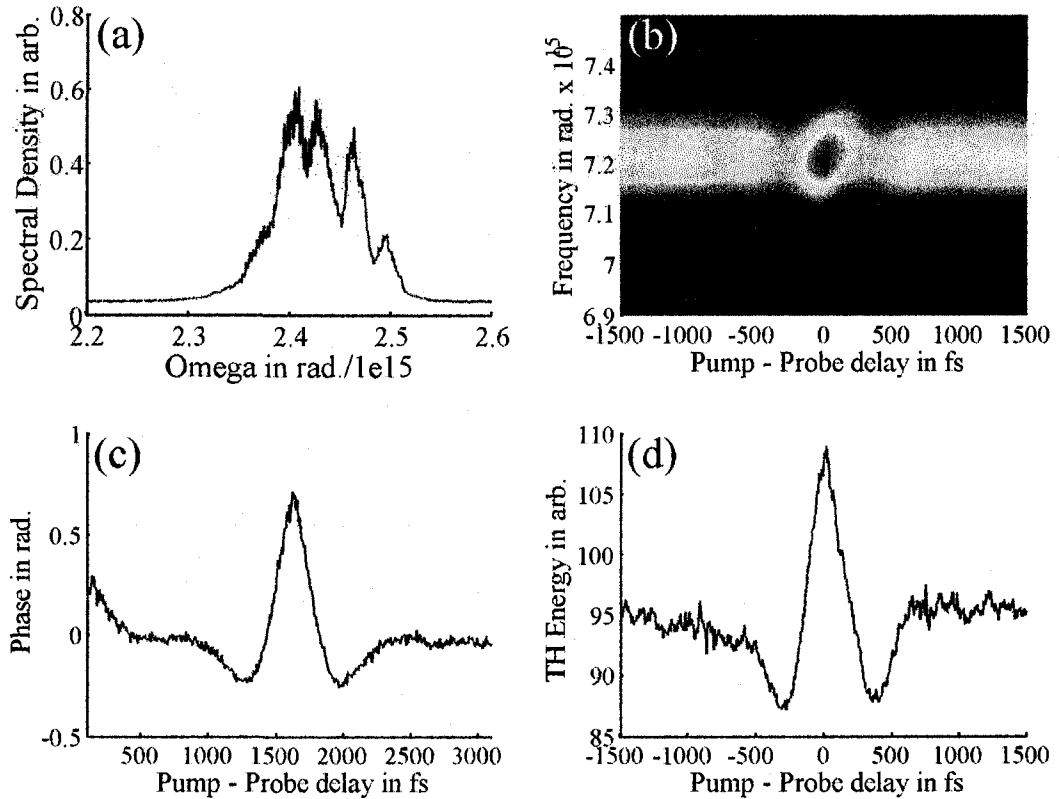


Figure 6.6: (a) Interferogram between strong probe and weak adjacent pulse. (b) Third harmonic spectra due to strong probe pulse, centered around the quarter revival. (c) Extracted relative phase between strong probe pulse and following weak pulse. (d) Modulation of third harmonic energy during the quarter revival.

The resulting interferogram between the weak pulse train and the probe pulse is shown in Fig. 6.6(a). Due to the significant difference in intensity, the fringe depth is not very high. It is, however, good enough to allow for the extraction of the relative phase between the probe pulse and the weak adjacent pulse. The resulting phase is shown in Fig. 6.6(c). It shows the alignment dynamic during the quarter revival

of the wave packet. At the same time, the third harmonic spectra were measured. These are shown in Fig. 6.6(b), and the energy in the third harmonic as a function of pump-probe delay in (d). The modulation in the third harmonic energy is clearly visible.

6.1.7 Summary

We have shown that the non-linear optical response of a medium is modulated at the revivals of a rotational wave packet. We can distinguish between Type I and Type II processes, where the modulation of the third harmonic generated via a Type I process is solely due to the dependence of the third non-linear susceptibility on the molecular alignment. An increase in conversion efficiency by 20% has been observed. Type II processes are influenced by both $\chi^{(3)}(\tau)$ as well as the change of the phase mismatch with τ , $\Delta k(\tau)$. Based on the model, the modulation of the conversion efficiency for Type II processes is dominated by the change in $\Delta k(\tau)$ with the molecular alignment, while the contribution of $\chi^{(3)}(\tau)$ was seen to be weaker. A parameter study with the model indicates with stronger alignment at lower temperature, it might be possible to phase match the Type II process, and with a longer interaction length, significant enhancements in THG conversion efficiency is predicted. This is particularly useful for third and higher harmonic conversion, since many crystals are absorbing in those regions and typically have a lower damage threshold than gases. Finally, we show briefly how a slight modification to a traditional Michelson interferometer allows for the concurrent detection of the wave packet contributions to the effective linear and nonlinear susceptibilities.

6.2 Enhanced efficiency for Third Harmonic Generation in the gas phase

In this section, we discuss a strongly enhanced conversion efficiency to the third-harmonic from a relatively weak IR probe pulse. The enhancement is attributed to a plasma near the focal region of the probe pulse which is induced by a strong pump pulse preceding the probe. Increasing the conversion efficiency for optical frequency conversion in the gas phase is beneficial for a variety of reasons. Most importantly, the dispersion of a gas is typically much lower than that of a crystal, and the transparency window is wider, as implied by the Kramers-Kronig relationship between the dispersive and absorptive contributions to the linear response of a medium[24]. Hence, broad-band frequency conversion is attainable, which might allow for the development of a source in the UV/EUV yielding short, and possibly even single-cycle pulses utilizing filamentation effects[118]. In addition to that, the damage threshold of gases is much higher than that of crystals, allowing for more intense and energetic fundamental pulses for an increased conversion efficiency. Here, however, we focus on an enhanced conversion efficiency for a relatively weak probe pulse, which is delayed and propagates non-collinearly with respect to a more energetic pump pulse. Since the probe pulse is weak, a rough estimate of the absolute conversion efficiency shows it is on the order of $10^{-6} - 10^{-7}$ in the absence of any plasma. This is very low conversion, considering conversion efficiencies of up to 0.02 % for third and 0.01% for fifth harmonic generation have been reported[114]. However, the enhancement for THG with a plasma present is up to about two orders of magnitude and will hopefully be extended to more energetic probe pulses, yielding a much improved absolute conversion efficiency. Since both pump and probe are off-resonant, ionization only occurs through multi-photon and tunnel ionization, and is therefore considered negligible for the weak probe. The propagation of the probe pulse is perturbed by the plasma in

the focal region due to both changes in the phase mismatch between the fundamental and third harmonic probe fields as well as plasma de-focussing. The spatial mode of the THG radiation generated by the probe beam is substantially improved when the pump pulse-induced plasma is present. This "beam clean-up" effect, also observed in filamentation, under vastly different propagation conditions, however, is preliminarily attributed to the transverse dependence of the plasma density and the resulting spatial filtering of the probe beam.

Under these conditions, we observe an increase in THG energy by more than two orders of magnitude over the THG energy without the pump-pulse induced ionization. We have investigated the laser-induced plasma enhancement in THG energy conversion for a variety of gases, both atomic and molecular, for different pump and probe energies, focal lengths, and gas pressures. In order to obtain a better understanding of the underlying mechanisms contributing to the enhancement, the propagation of the probe pulse has been modeled using Equ's. 2.15 and 2.16.

6.2.1 Experimental setup

The experimental setup used for the following experiments is identical to that utilized to measure the modulation of THG in the presence of a rotational wave packet, except in addition to recording the THG spectra, a photo diode was used to measure the power of the third harmonic. Briefly, the experimental parameters and the setup is listed here for completeness: In the experiments, ~ 1 -mJ pulses, 35-fs pulses centered at 785 nm from a Ti:sapphire amplifier (KMLabs Dragon, Boulder, CO) are split into pump and probe pulses with adjustable relative power with a half wave plate and a thin film polarizer. An additional half wave plate and polarizer placed in the probe arm are used to adjust the probe energy. Pulse energies used are $\sim 800 \mu\text{J}$ in the pump arm, and 85 to 140 μJ in the orthogonally-polarized probe. The pump and probe beams are collinearly focused into a gas cell with a spherical mirror (focal length

$f = 30$ and 50 cm) filled with Neon, Argon, SF_6 , CO_2 , and N_2O gases at pressures ranging from 20 to 800 Torr. We profile the spatial mode of the pump and probe pulses through the focal region using knife-edge scans. These measurements indicate that the crossing angle between the pulses is between 2 and 4 degrees, depending on the focal length, and the interaction length ranges between 0.6 and 1.2 cm. The third harmonic field is separated from the fundamental probe field with three dichroic mirrors centered at 266 nm. The third harmonic spectra are recorded with an Ocean Optics USB4000 spectrometer. The relative THG pulse energy is recorded by integrating the signal from a GaP photodiode (Thor Labs) with a boxcar integrator set to average over 1000 samples and gain adjusted based on the signal level.

6.2.2 Observations of enhanced THG

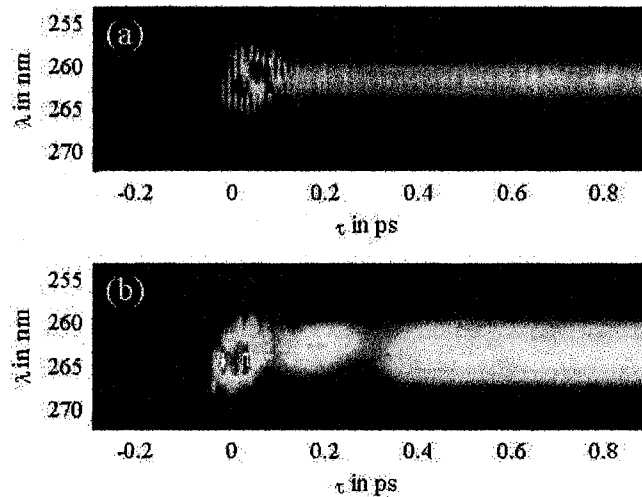


Figure 6.7: Recorded third harmonic spectra across the pump-probe time zero in (a) Argon and (b) CO_2 , both at 600 Torr.

The enhancement of the THG energy generated by the probe pulse is illustrated in Fig. 6.7. Figure 6.7(a) shows third harmonic spectra recorded through a scan of the pump-probe delay for a $85 \mu\text{J}$ probe pulse through time zero. A drastic change in conversion efficiency that persists after the pump pulse induced ionization is evident

in the THG spectra recorded for Argon gas at 600 Torr. The dynamic range of the spectrometer is not sufficient to simultaneously detect the signal before time zero within the same scan. Similar enhancements are observed in molecular gases, an example of which is shown in Fig 6.7(b) where an increase in THG energy is observed after time zero for CO₂ at 600 Torr with an 85 μ J probe pulse. Note that near time-zero, the CO₂ data exhibit time-dependent modulation of THG conversion due to alignment arising from a rotational wave packet excited by the pump pulse[?]. A few hundred femtoseconds after time-zero, the THG spectra in Fig 6.7(b) no longer vary with time since the initial rotational wave packet has dephased. To separate the effects of the rotational molecular response from the enhancement attributed to the plasma, the THG data that follow are gathered at a pump-probe delay of 2-ps.

In addition to a large increase in conversion efficiency, a clear improvement in the third harmonic beam quality of the probe pulse is observed in the presence of the pump-pulse induced plasma. This enhanced beam quality is analogous to behavior observed in filament propagation[31]. The beam improvement observed in our experiments suggests that propagation effects in the pump pulse induced plasma similar to filamentation behavior may play a role in the THG enhancement. Recently, efficient THG by a pulse propagating in a filament has been observed with low fluctuation in the signal strength and very good spatial beam properties for the third harmonic[113]. Moreover, since the THG mode changes may affect coupling into the spectrometer, the changes in the THG energy were recorded by focusing the THG beam onto a GaP photodiode so that the spot size was smaller than the active area of the photodiode. With these precautions, changes in the spatial mode of the THG beam will not lead to erroneous measurements of the relative THG pulse energy.

While the enhancements for THG conversion efficiency across time-zero based on the pump-pulse induced plasma shown in Fig 6.7 are readily observable, the precise enhancement will depend on the parameters of the experiment. Clearly, the third

harmonic generation conversion efficiency will be strongly influenced by the changes in dispersion due to the plasma, i.e., changes in phase mismatch. However, the impact of the phase mismatch change depends on the focusing conditions of both pulses and the pressure of the gas. In addition, the interaction length of the probe pulse with the plasma as well as the probe pulse energy will strongly influence the resulting energy in the third harmonic.

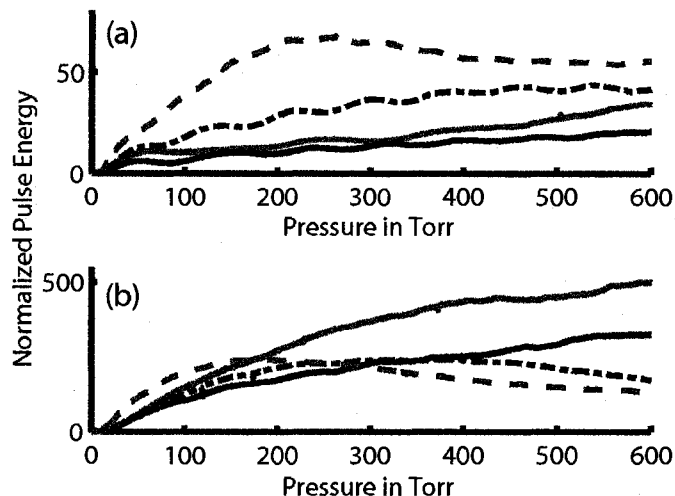


Figure 6.8: Photodiode signal measuring relative THG average power in Ar (red), SF₆ (black), CO₂ (blue, dot-dash), and N₂O (red, dashed) with a focal length of 30 cm and and probe and pump pulse energy of 140 and 790 μ J, respectively. The relative THG over a range of pressure is shown both without (a) and with (b) the pump pulse.

In order to systematically study the observed THG enhancement on these parameters, we have investigated changes in THG conversion energy for a range of parameters. For each focal length and set of pump and probe energies, the relative THG energy is recorded with and without the pump pulse present over a range of gas pressure. Relative THG energy data as a function of pressure for a set of gases for probe and pump pulse energies of 140 and 790 μ J, respectively, for a focal length of 30 cm are shown in Fig. 6.8(a) with the pump pulse blocked and in Fig. 6.8(b) with the pump pulse present. Note that the scale on Fig. 6.8(b) is an order of magnitude larger than for Fig. 6.8(a). With the non-collinear geometry, we carefully verified that no THG generated by the pump pulse leaked into our photodiode signal. The THG

energy generated with Ne is an order of magnitude weaker and has consequently been omitted from this figure. Clearly, the THG conversion efficiency is much stronger when the pump pulse induced plasma is present. Without the pump pulse present, the THG energy exhibits modulations with increasing pressure due to the a decrease in coherence length as the pressure rises. With the presence of the pump pulse induced ionization, the ripples are substantially reduced, due in part to a change in the dispersion from the plasma.

The enhancement ratio obtained from the pressure scans from those gases for the experimental conditions of Fig. 6.8 is shown in Fig. 6.9(a). Here, we see peak enhancements in the conversion efficiency ranging from 8 to 45. Experimental data were collected for a 50-cm focal length in addition to the 30-cm data. With an increased interaction length, the peak intensity is reduced so that the absolute THG conversion efficiency by the probe pulse as well as ionization by the pump pulse are reduced. In this case, we observed enhancements in THG conversion efficiency by more than two orders of magnitude. The enhancement data collected for this focal length with Ar gas is shown in Fig. 6.9(b). Note that near 150 Torr, when the noise spike is discounted, an enhancement in THG conversion efficiency of 300 is observed.

The observed enhancements for the range of gases are presented in Table II. In the first column of this table, we list the gas species studied in these experiments, while in the second column we list the ionization potentials of these gas species obtained from Ref. [119]. The remaining columns report the maximum enhancement of THG conversion efficiency for each gas species. Since the only dominant change in an atomic gas induced by the pump pulse that persists at a 2-ps delay is the presence of the pump-induced plasma, one might expect the enhancement to increase with decreasing ionization potential. Surprisingly, inspection of Table II indicates that for these experimental conditions, the enhancement is strongest for the gas species hardest to ionize. For the 30-cm focal length, this is Ne with an enhancement of 45

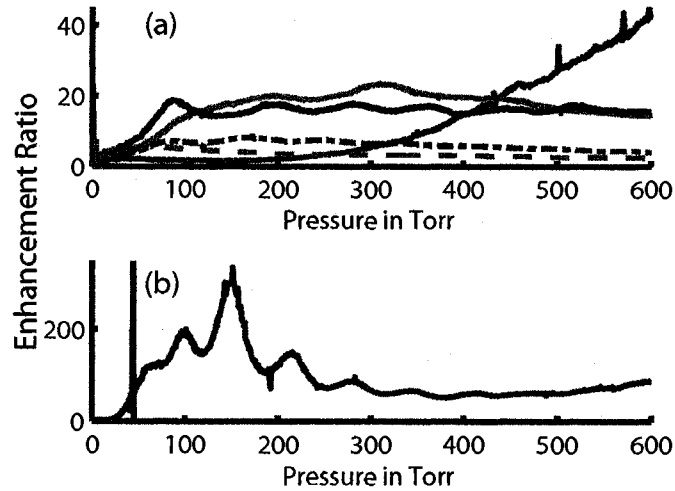


Figure 6.9: (a) THG conversion enhancement for Ne (blue), Ar (red), SF₆ (black), CO₂ (blue, dot-dash), and N₂O (red, dashed) with 30 cm focal mirror and probe and pump pulse energy of 140 and 790 μ J, respectively. (b) Maximum enhancement observed for Argon with a focal length of 50 cm and the pulse energies given for (a).

and for the 50-cm focal length Ar yields the strongest enhancement since the effect was not observed in under these conditions in Ne due to low signal intensities.

The enhancements and conversion efficiencies were studied as a function of probe pulse intensity for a fixed pump pulse energy of 820 μ J and a focal length of 30-cm. The pressure scans for pulse energies of 160 and 120 μ J giving a probe intensity ratio of 4:3 were recorded in a number of gases. All of the gases exhibited an increase in total THG energy for the higher probe pulse energy. The maximum THG signal with the plasma present increases by 20%, 42%, and 29% when the probe pulse energy is increased from 120 to 160 μ J for Ar, SF₆, and CO₂, respectively.

6.2.3 Summary

In summary, we have shown that the third harmonic generated by a relatively weak probe pulse can be enhanced by more than two orders of magnitude when the probe pulse propagates through a plasma generated by a moderately intense pump pulse at its focus. This effect has been observed for atomic as well as molecular gases. The

Table II: Gases used in the experiment with their respective ionization potential in eV. The enhancement quoted is the peak enhancement found in the pressure scans with a 30 cm and 50 cm focal length mirror and 140 mW probe power.

Gas	I_p in eV	30 cm	50 cm
Neon	21.56	45	N/A
Argon	15.76	25	300
SF ₆	15.32	14	175
CO ₂	13.77	9	45
N ₂ O	12.89	8	10

spatial mode of the third harmonic is vastly improved for all cases in the presence of the pump. The results of this experiment indicate complex dynamics due to a laser-induced plasma with effects on dispersion, nonlinear frequency conversion, and propagation for THG conversion. Enhancements in conversion efficiency to the third harmonic as high as 300 for a weak probe pulse have been observed. This experimental arrangement should prove useful for strong-field experiments that require energetic and broad bandwidth UV pulses. We are currently investigating this effect using an analytic as well as numeric model. While the analytic model seems to result in an overly simplified approach, the numeric model, while still preliminary, appears to predict enhancements for THG that are in quantitative agreement with what has been observed experimentally. Further experimental studies in conjunction with theoretical developments will enable a better understanding of the underlying physics.

Chapter 7

Conclusions

In conclusion, we have shown in detail, theoretically as well as experimentally, the propagation effects on a relatively weak, ultrashort laser pulse due to coherent nuclear motion. Both rotational and vibrational motion have been discussed, although a heavier focus lies on coherent rotational motion. The effect of CNM, excited via impulsive stimulated Raman scattering, is expressed in terms of an effective susceptibility, where we separate effects due to an effective linear susceptibility from that of an effective third-order susceptibility. We derive the NLSE with some modifications to describe pulse propagation in conjunction with the effective susceptibilities modeling the CNM where we extend the traditional NLSE to include current densities induced by the weak probe pulse due to the presence of a laser-induced plasma. The delayed Raman response of the medium can be modeled in a variety of manners. We have outlined the traditional approach utilizing the Born-Oppenheimer approximation. In addition to that, for the rotational response of an ensemble of molecules we have described an analytic model which is not limited to a perturbative interaction between a strong ultrashort pulse and a molecule and compared its accuracy to a full numerical solution of the Schrödinger equation to confirm its validity for high pulse intensities. This model may be extended to describe the excitation of a wave

packet by two or more pump pulses, each arbitrarily polarized. This may allow for further insights into the formation of rotational wave packets, as well as for further optimization of the excitation process. This might help with the realization of new applications to rotational wave packets. The resulting time dependence of the effective third-order susceptibility has been shown to potentially yield a new method of quasi-phase matching, and thus, enhance the conversion efficiency for non-linear optical frequency conversion in the gas phase.

The temporal phase modulation due to coherent rotational motion has been measured using standard scanning interferometry, where we show that transiently aligned molecules in a gas phase can act like a wave plate, with the additional feature of separating a single, linearly polarized probe pulse into two distinct pulses under conditions of strong phase modulation and significant spectral modification. The adaptation of chirped spectral interferometry to provide a way of measuring the phase modulation during a wave packet revival in a single shot for an arbitrarily polarized pump pulse extends standard polarization gating measurements since the direct measurement of the phase modulation does not require the medium to be birefringent in the polarization plane of the pump pulse. The last propagation effect due to the effective linear susceptibility investigated is the modification of the pulse's group velocity due to the molecular alignment. This effect is predicted by theory and confirmed experimentally, however, the functional dependence of the group velocity modification in the experiment is different from what is expected based on the theory. This discrepancy has not been resolved thus far. Finally, we investigate the effective non-linear susceptibility and its ramifications for pulse propagation and frequency conversion. Most notably, the conversion efficiency to the third harmonic becomes a function of pump-probe delay during CNM. This dependence, utilized in the novel approach to quasi-phase matching, has been observed experimentally in CO_2 and N_2O for coherent rotational motion, as well as SF_6 for vibrations. The modulation in the conversion efficiency

is significant and allows for very sensitive detection of CNM. Furthermore, the modulation of the conversion efficiency to the third harmonic may also be viewed as a higher-order Raman process, i.e., second-hyper Raman scattering. It has been theorized that there are modes which are not accessible through Raman scattering, but require a higher-order Raman process. Further investigation of second-hyper Raman scattering may therefore yield new insights into intramolecular dynamics, especially if a direct excitation and subsequent detection of a second-hyper Raman mode can be achieved.

Separately from CNM, we investigated a more than 300 fold enhancement of THG in the presence of a laser-induced plasma at the focus of a relatively weak probe pulse. The enhancement has been observed in a variety of gases, both molecular as well as atomic, and is thus clearly separate from CNM. In all cases, the spatial mode of the third harmonic is vastly improved compared to the mode resulting in the absence of a plasma. The exact nature of the physics involved in the enhancement is at this point not entirely clear. However, filament-like propagation, as well as the dispersive effect of the plasma likely play a role. We are currently working on extensive simulations aimed at shedding light on this process. In conjunction with that, we are hoping to achieve this level of enhancement with highly energetic pulses, thus obtaining an efficient UV source with broad bandwidth.

Bibliography

- [1] B. Friedrich and D. Herschbach, "Alignment and trapping of molecules in intense laser fields," *Phys. Rev. Lett.* **74**(23), 4623–4626 (1995).
- [2] C. Lin, J. Heritage, and T. Gustafson, "Susceptibility echos in linear molecular gases," *Appl. Phys. Lett.* **19**, 397–& (1971).
- [3] C. Lin, J. Heritage, T. Gustafson, R. Chiao, and J. McTague, "Birefringence arising from reorientation of polarizability anisotropy of molecules in collisionless gases," *Phys. Rev. A* **13**, 813–829 (1976).
- [4] T. Seideman and E. Hamilton, "Nonadiabatic alignment by intense pulses. Concepts, theory, and directions," (2005).
- [5] H. Stapelfeldt and T. Seideman, "Colloquium: Aligning molecules with strong laser pulses," *Rev Mod Phys* **75**, 543–557 (2003).
- [6] T. Seideman, "Rotational excitation and molecular alignment in intense laser fields," *J. Chem. Phys.* **103**(18), 7887–7896 (1995).
- [7] M. Renard, E. Hertz, S. Guerin, H. R. Jauslin, B. Lavorel, and O. Faucher, "Control of field-free molecular alignment by phase-shaped laser pulses," *Phys. Rev. A* **72**(2), 025,401 (2005).
- [8] D. Daems, S. Guérin, E. Hertz, H. R. Jauslin, B. Lavorel, and O. Faucher, "Field-Free Two-Direction Alignment Alternation of Linear Molecules by Elliptic Laser Pulses," *Phys. Rev. Lett.* **95**(6), 4 (2005).
- [9] J. Larsen, K. Hald, N. Bjerre, H. Stapelfeldt, and T. Seideman, "Three dimensional alignment of molecules using elliptically polarized laser fields," *Phys Rev Lett* **85**, 2470–2473 (2000).
- [10] K. F. Lee, D. M. Villeneuve, P. B. Corkum, A. Stolow, and J. G. Underwood, "Field-free three-dimensional alignment of polyatomic molecules," *Phys. Rev. Lett.* **97**(17), 173,001 (2006).
- [11] S. S. Viftrup, V. Kumarappan, S. Trippel, H. Stapelfeldt, E. Hamilton, and T. Seideman, "Holding and spinning molecules in space," *Phys. Rev. Lett.* **99**(14), 143,602 (2007).

- [12] P. M. Felker, "Rotational coherence spectroscopy - Studies of the geometries of large gas-phase species by picosecond time-domain methods," *J. Phys. Chem.* **96**(20), 7844–7857 (1992).
- [13] R. Bartels, T. Weinacht, N. Wagner, M. Baertschy, C. Greene, M. Murnane, and H. Kapteyn, "Phase modulation of ultrashort light pulses using molecular rotational wave packets," *Phys Rev Lett* **88**, 013,903 (2002).
- [14] S. Ramakrishna and T. Seideman, "Information Content of High Harmonics Generated from Aligned Molecules," *Phys. Rev. Lett.* **99**(11), 4 (2007).
- [15] R. A. Bartels, N. L. Wagner, M. D. Baertschy, J. Wyss, M. M. Murnane, and H. C. Kapteyn, "Phase-matching conditions for nonlinear frequency conversion by use of aligned molecular gases," *Opt. Lett.* **28**(5), 346–348 (2003).
- [16] S. Fleischer, I. S. Averbukh, and Y. Prior, "Selective alignment of molecular spin isomers," *Phys. Rev. Lett.* **99**(9), 093,002 (2007).
- [17] K. Hartinger and R. A. Bartels, "Analytical model of the effective transient optical response of symmetric-top molecules in the presence of a rotational coherence," *J Opt Soc Am* **25**(3), 407–413 (2008).
- [18] K. Hartinger, S. Nirmalgandhi, J. Wilson, and R. Bartels, "Efficient nonlinear frequency conversion with a dynamically structured nonlinearity," *Opt Express* **13**, 6919–6930 (2005).
- [19] K. Hartinger and R. A. Bartels, "Single-shot measurement of ultrafast time-varying phase modulation induced by femtosecond laser pulses with arbitrary polarization," *Appl Phys Lett* **92**, 021,126 (2008).
- [20] Y. R. Shen, *The Principles of Nonlinear Optics* (John Wiley and Sons Inc., Hoboken, New Jersey, 2002).
- [21] G. S. Agarwal, *Nonlinear Fiber Optics* (Academic Press, 2001).
- [22] T. Brabec and F. Krausz, "Nonlinear optical pulse propagation in the single-cycle regime," *Phys. Rev. Lett.* **78**(17), 3282–3285 (1997).
- [23] M. Kolesik, J. V. Moloney, and M. Mlejnek, "Unidirectional Optical Pulse Propagation Equation," *Physical Review Letters* **89**(28) (2002). URL <http://link.aps.org/abstract/PRL/v89/e283902>.
- [24] D. Jackson, *Classical Electrodynamics*, 3rd ed. (Wiley, 1998).
- [25] E. J. Fonseca, S. B. Cavalcanti, and J. M. Hickmann, "Space-time break-up in the self-focusing of ultrashort pulses," *Opt Commun* **169**(1-6), 199–205 (1999).
- [26] H. Leblond, S. V. Sazonov, I. V. Mel'nikov, D. Mihalache, and F. Sanchez, "Few-cycle nonlinear optics of multicomponent media," *Phys. Rev. A* **74**(6), 063,815 (2006).

- [27] M. Kolesik and J. Moloney, "Nonlinear optical pulse propagation simulation: From Maxwell's to unidirectional equations," *Phys Rev E* **70**, 036,604 (2004).
- [28] G. B. A. H. J. Weber, *Mathematical Methods for Physicists* (Academic Press, 2005).
- [29] S. Mukamel, "Principles of Nonlinear Optical Spectroscopy," p. 576 (1999).
- [30] R. A. Fisher and W. Bischel, "The role of linear dispersion in plane-wave self-phase modulation," *Applied Physics Letters* **23**(12), 661–663 (1973). URL <http://link.aip.org/link/?APL/23/661/1>.
- [31] S. Chin, S. Hosseini, W. Liu, Q. Luo, F. Théberge, N. Aközbek, A. Becker, V. Kandidov, O. Kosareva, and H. Schroeder, "The propagation of powerful femtosecond laser pulses in optical media: physics, applications, and new challenges," *Can. J. Phys.* **83**(9), 863–905 (2005).
- [32] M. Ammosov, N. Delone, and V. P. Krainov, "Tunnel ionization of complex atoms and of atomic ions in an alternating electromagnetic field," *Journal of Experimental and Theoretical Physics* **64**(6), 1191–1194 (1986).
- [33] R. Boyd, *Nonlinear Optics* (Academic Press, 2003).
- [34] K. Hartinger and R. A. Bartels, "Pulse polarization splitting in a transient wave plate," *Opt Lett* **31**, 3526–3528 (2006).
- [35] A. Nazarkin, G. Korn, M. Wittmann, and T. Elsaesser, "Group-velocity-matched interactions in hollow waveguides: Enhanced high-order Raman scattering by impulsively excited molecular vibrations," *Phys. Rev. A* **65**(4), 041,802 (2002).
- [36] M. Born and R. Oppenheimer, "Quantum theory of molecules," *Annalen der Physik* **84**(20), 0457–0484 (1927).
- [37] N. Ji and Y.-R. Shen, "A novel spectroscopic probe for molecular chirality," *Chirality* **18**(3), 146–158 (2006).
- [38] R. W. Hellwarth, "Third order susceptibilities of liquids and solids," *Prog. Quant. Elec.* **5**, 1–68 (1977).
- [39] T. A. Carlson, "Angular dependence of vibrational structure in the photoelectron spectra of N-2 and O-2," *Chem Phys Lett* **9**(1), 23–26 (1971).
- [40] B. Hellsing, A. Eiguren, E. Chulkov, and P. M. Echenique, "Electron-phonon coupling and lifetimes of excited surface states," *Surface Science* **593**(1-3), 12–18 (2005).
- [41] D. C. Paul N. Butcher, *The Elements of Nonlinear Optics* (Cambridge University Press, 1991).

- [42] T. Steffen, J. T. Fourkas, and K. Duppen, "Time resolved four- and six-wave mixing in liquids .1. Theory," *J. Chem. Phys.* **105**(17), 7364–7382 (1996).
- [43] K. Kubarych, C. Milne, S. Lin, and R. Miller, "Diffractive optics implementation of time- and frequency-domain heterodyne-detected six-wave mixing," *Applied Physics B: Lasers and Optics* **74**(9), s107–s112 (2002).
- [44] R. Torre, ed., *Time-Resolved Spectroscopy in Complex liquids - An Experimental Perspective* (Springer, 2008).
- [45] J. Heritage, T. Gustafson, and C. Lin, "Observation of coherent transient birefringence in CS₂ vapor," *Phys Rev Lett* **34**, 1299–1302 (1975).
- [46] F. Noack, O. Steinkellner, P. Tzankov, H. H. Ritze, J. Herrmann, and Y. Kida, "Generation of sub-30 fs ultraviolet pulses by Raman induced phase modulation in nitrogen," *Opt Express* **13**(7), 2467–2474 (2005).
- [47] V. Renard, O. Faucher, and B. Lavorel, "Measurement of laser-induced alignment of molecules by cross defocusing," *Opt. Lett.* **30**(1), 70–72 (2005).
- [48] J. Itatani, J. Levesque, D. Zeidler, H. Niikura, H. Pepin, J. C. Kieffer, P. B. Corkum, and D. M. Villeneuve, "Tomographic imaging of molecular orbitals," *Nature* **432**(7019), 867–871 (2004).
- [49] F. H. M. Faisal, A. Abdurrouf, K. Miyazaki, and G. Miyaji, "Origin of anomalous spectra of dynamic alignments observed in N-2 and O-2," *Phys. Rev. Lett.* **98**(14), 143,001 (2007).
- [50] Y. Suzuki and T. Seideman, "Mapping rotational coherences onto time-resolved photoelectron imaging observables," *J. Chem. Phys.* **122**(23), 234,302 (2005).
- [51] D. Zeidler, A. B. Bardon, A. Staudte, D. M. Villeneuve, R. Dorner, and P. B. Corkum, "Alignment independence of the instantaneous ionization rate for nitrogen molecules," *J. Phys. B: At. Mol. Opt. Phys.* **39**(7), L159–L166 (2006).
- [52] P. A. Block, E. J. Bohac, and R. E. Miller, "Spectroscopy of pendular states - The use of molecular-complexes in achieving orientation," *Phys. Rev. Lett.* **68**(9), 1303–1306 (1992).
- [53] M. F. Gelin, C. Riehn, V. V. Matylitsky, and B. Brutschy, "Rotational recurrences in thermal ensembles of nonrigid molecules," *Chemical Physics* **290**(2-3), 307–318 (2003).
- [54] V. Aquilanti, M. Bartolomei, F. Pirani, D. Cappelletti, F. Vecchiocattivi, Y. Shimizu, and T. Kasai, "Orienting and aligning molecules for stereochemistry and photodynamics," *Phys. Chem. Chem. Phys.* **7**(2), 291–300 (2005).
- [55] S. Ramakrishna and T. Seideman, "Dissipative dynamics of laser induced nonadiabatic molecular alignment," *J. Chem. Phys.* **124**(3), 034,101 (2006).

- [56] R. Santra, "Imaging molecular orbitals using photoionization," *Chem. Phys.* **329**(1-3), 357-364 (2006).
- [57] M. Leibscher, I. S. Averbukh, and H. Rabitz, "Enhanced molecular alignment by short laser pulses," *Phys. Rev. A* **69**(1), 10 (2004).
- [58] E. Peronne, M. Poulsen, C. Bisgaard, H. Stapelfeldt, and T. Seideman, "Nonadiabatic alignment of asymmetric top molecules: Field-free alignment of iodobenzene," *Phys Rev Lett* **91**, 043,003 (2003).
- [59] E. Hamilton, T. Seideman, C. Z. Bisgaard, S. S. Viftrup, and H. Stapelfeldt, "Alignment of symmetric top molecules by short laser pulses," *Phys. Rev. A* **72**(4), 12 (2005).
- [60] V. V. Matylitsky, W. Jarzeba, C. Riehn, and B. Brutschy, "Femtosecond degenerate four-wave mixing study of benzene in the gas phase," *J. Raman Spectrosc.* **33**(11-12), 877-883 (2002).
- [61] R. N. Zare, *Angular Momentum: Understanding Spatial Aspects in Chemistry and Physics* (John Wiley and Sons Inc., 1988).
- [62] *Table of Integrals, Series, and Products*, 6th ed. (Academic Press, 2000).
- [63] Z. Majcherova, P. Macko, D. Romanini, V. Perevalov, S. Tashkun, J. Teffo, and A. Campargue, "High-sensitivity CW-cavity ringdown spectroscopy of CO near 1.5 μ m," *Journal of Molecular Spectroscopy* **230**(1), 1-21 (2005).
- [64] F. Ito, "Methyl iodide clusters observed in gas phase by infrared cavity ringdown spectroscopy: The CH₃ bending mode at 8 μ m," *J. Chem. Phys.* **124**(5), 054,309 (2006).
- [65] G. Herzberg, *Molecular Spectra and Molecular Structure*, vol. 2 (Krieger Pub Co, 1991).
- [66] A. J. Gray and R. J. Butcher, "High-resolution laser-radiofrequency double-resonance molecular-spectroscopy," *Proc. Roy. Soc. A - Mathematical physical and engineering sciences* **445**(1925), 543-560 (1994).
- [67] E. B. Wilson, "The statistical weights of the rotational levels of polyatomic molecules, including methane, ammonia, benzene, cyclopropane and ethylene," *J. Chem. Phys.* **3**(5), 276-285 (1935).
- [68] S. Zamith, Z. Ansari, F. Lepine, and M. Vrakking, "Single-shot measurement of revival structures in femtosecond laser-induced alignment of molecules," *Opt Lett* **30**, 2326-2328 (2005).
- [69] G. Lesaux, F. Salin, P. Georges, G. Roger, and A. Brun, "Single shot measurement of the optical Kerr effect kinetics," *Appl Optics* **27**, 777-779 (1988).

- [70] K. Hartinger and R. A. Bartels, "Single-shot measurement of ultrafast time-varying phase modulation induced by femtosecond laser pulses with arbitrary polarization," *Appl. Phys. Lett.* **92**(2), 021,126 (2008).
- [71] K. Hartinger and R. A. Bartels, "Modulation of third-harmonic generation conversion in the presence of a rotational wave packet," *Opt. Lett.* **33**(11), 1162–1164 (2008).
- [72] J. Armstrong, N. Bloembergen, J. Ducuing, and P. Pershan, "Interactions between light waves in a nonlinear dielectric," *Phys Rev* **127**, 1918–& (1962).
- [73] S. Somekh and A. Yariv, "Phase matching by periodic modulation of the nonlinear optical properties," *Optics Communications* (1972).
- [74] J. D. McMullen, "Optical parametric interactions in isotropic materials using a phase-corrected stack of nonlinear dielectric plates," *J. Appl. Phys.* **46**(7), 3076 (1975).
- [75] A. H. A. Szilagyı and H. Schlossberg, "A quasi-phase-matching technique for efficient optical mixing and frequency doubling," *J. Appl. Phys.* **47**, 2025 (1976).
- [76] D. E. Thompson, J. D. McMullen, and D. B. Anderson, "2nd-harmonic generation in GaAs stack of plates using high-power CO₂-laser radiation," *Appl Phys Lett* **29**(2), 113–115 (1976).
- [77] C. F. Dewey and L. O. Hocker, "Enhanced nonlinear optical effects in rotationally twinned crystals," *Appl Phys Lett* **26**(8), 442–444 (1975).
- [78] D. Feng, N. B. Ming, J. F. Hong, Y. S. Yang, J. S. Zhu, Z. Yang, and Y. N. Wang, "Enhancement of 2nd-harmonic generation in LINBO₃ crystals with periodic laminar ferroelectric domains," *Appl. Phys. Lett.* **37**(7), 607–609 (1980).
- [79] A. Feisst and P. Koidl, "Current induced periodic ferroelectric domain-structures in LINBO₃ applied for efficient nonlinear optical frequency mixing," *Appl Phys Lett* **47**(11), 1125–1127 (1985).
- [80] K. D. Singer, J. E. Sohn, and S. J. Lalama, "2nd harmonic-generation in poled polymer-films," *Appl. Phys. Lett.* **49**(5), 248–250 (1986).
- [81] D. L. Williams, D. P. West, and T. A. King, "Quasi-phase matched third harmonic generation," *Opt Commun* **148**(1-3), 208–214 (1998).
- [82] J. F. Ward and G. H. C. New, "Optical third harmonic generation in gases by a focused laser beam," *Phys Rev* **185**(1), 57–72 (1969).
- [83] A. J. Merriam, S. J. Sharpe, M. Shverdin, D. Manuszak, G. Y. Yin, and S. E. Harris, "Efficient nonlinear frequency conversion in an all-resonant double-Lambda system," *Phys. Rev. Lett.* **84**(23), 5308–5311 (2000).

- [84] C. G. Durfee, A. R. Rundquist, S. Backus, C. Herne, M. M. Murnane, and H. C. Kapteyn, "Phase matching of high-order harmonics in hollow waveguides," *Phys. Rev. Lett.* **83**(11), 2187–2190 (1999).
- [85] A. Rundquist, C. G. Durfee, Z. H. Chang, C. Herne, S. Backus, M. M. Murnane, and H. C. Kapteyn, "Phase-matched generation of coherent soft X-rays," *Science* **280**(5368), 1412–1415 (1998).
- [86] R. A. Bartels, A. Paul, H. Green, H. C. Kapteyn, M. M. Murnane, S. Backus, I. P. Christov, Y. W. Liu, D. Attwood, and C. Jacobsen, "Generation of spatially coherent light at extreme ultraviolet wavelengths," *Science* **297**(5580), 376–378 (2002).
- [87] B. F. Levine, C. G. Bethea, and R. A. Logan, "Phase-matched second-harmonic generation in a liquid-filled waveguide," *Appl. Phys. Lett.* **26**(7), 375–377 (1975).
- [88] A. Paul, R. A. Bartels, R. Tobey, H. Green, S. Weiman, I. P. Christov, M. M. Murnane, H. C. Kapteyn, and S. Backus, "Quasi-phase-matched generation of coherent extreme-ultraviolet light," *Nature* **421**(6918), 51–54 (2003).
- [89] Z. Bor and B. Racz, "Group-velocity dispersion in prisms and its application to pulse-compression and traveling-wave excitation," *Opt Commun* **54**(3), 165–170 (1985).
- [90] A. Rizzo and N. Rahman, "The linear and nonlinear susceptibilities of acetylene relevant for high order harmonic generation," *Laser Physics* **9**(1), 416–421 (1999).
- [91] M. Leibscher, I. S. Averbukh, and H. Rabitz, "Molecular alignment by trains of short laser pulses," *Phys. Rev. Lett.* **90**(21), 213,001 (2003).
- [92] P. Schlup, J. Wilson, K. Hartinger, and R. A. Bartels, "Dispersion balancing of variable-delay monolithic pulse splitters," *Appl Optics* **46**, 5967–5973 (2007).
- [93] G. R. Fleming and A. E. Siegman, "Ultrafast Phenomena V: Proceedings of the Fifth OSA Topical Meeting ..." (1986).
- [94] Z. Jiang and X. Zhang, "Single-shot measurement of a Terahertz pulse," *Appl Optics* **37**, 8145–8146 (1998).
- [95] I. Shkrob, D. Oulianov, R. Crowell, and S. Pommeret, "Frequency-domain "single-shot" ultrafast transient absorption spectroscopy using chirped laser pulses," *J Appl Phys* **96**, 25–33 (2004).
- [96] E. Tokunaga, A. Terasaki, and T. Kobayashi, "Induced phase modulation of chirped continuum pulses studied with a femtosecond frequency-domain interferometer," *Opt Lett* **18**, 370–372 (1993).

- [97] A. Benuzzi-Mounaix, M. Koenig, J. Boudenne, T. Hall, D. Batani, F. Scianitti, A. Masini, and D. D. Santo, "Chirped pulse reflectivity and frequency domain interferometry in laser driven shock experiments," *Phys Rev E* **60**, R2488–R2491 (1999).
- [98] C. Chien, B. L. Fontaine, A. Desparois, Z. Jiang, T. Johnston, J. Kieffer, H. Pepin, F. Vidal, and H. Mercure, "Single-shot chirped-pulse spectral interferometry used to measure the femtosecond ionization dynamics of air," *Opt Lett* **25**, 578–580 (2000).
- [99] K. Kim, I. Alexeev, and H. Milchberg, "Single-shot supercontinuum spectral interferometry," *Appl. Phys. Lett.* **81**, 4124–4126 (2002).
- [100] A. L. Smirl, X. Chen, and O. Buccafusca, "Ultrafast time-resolved quantum beats in the polarization state of coherent emission from quantum wells," *Opt. Lett.* **23**(14), 1120–1122 (1998).
- [101] N. Zhavoronkov and G. Korn, "Generation of single intense short optical pulses by ultrafast molecular phase modulation," *Phys Rev Lett* **88**, 203,901 (2002).
- [102] H. Rabitz, R. de Vivie-Riedle, M. Motzkus, and K. Kompa, "Chemistry - Whither the future of controlling quantum phenomena?" *Science* **288**(5467), 824–828 (2000).
- [103] A. Assion, T. Baumert, M. Geisler, V. Seyfried, and G. Gerber, "Mapping of vibrational wave-packet motion by femtosecond time-resolved kinetic energy time-of-flight mass spectroscopy," *European Physical Journal D* **4**(2), 145–149 (1998).
- [104] R. Bartels, S. Backus, E. Zeek, L. Misoguti, G. Vdovin, I. P. Christov, M. M. Murnane, and H. C. Kapteyn, "Shaped-pulse optimization of coherent emission of high-harmonic soft X-rays," *Nature* **406**(6792), 164–166 (2000).
- [105] S. Backus, R. Bartels, S. Thompson, R. Dollinger, H. C. Kapteyn, and M. M. Murnane, "Sigh-efficiency, single-stage 7-kHz high-average-power ultrafast laser system," *Opt. Lett.* **26**(7), 465–467 (2001).
- [106] O. Masihzadeh, M. Baertschy, and R. A. Bartels, "Optimal single-pulse excitation of rotational impulsive molecular phase modulation," *Opt Express* **14**(6), 2520–2532 (2006).
- [107] S. E. Harris, A. V. Sokolov, M. Y. Shverdin, D. R. Walker, D. D. Yavuz, A. M. Burzo, and G. Y. Yin, "Generation and control of femtosecond pulses by molecular modulation," *Journal of Modern Optics* **52**(2-3), 285–304 (2005).
- [108] R. Velotta, N. Hay, M. B. Mason, M. Castillejo, and J. P. Marangos, "High-Order Harmonic Generation in Aligned Molecules," *Physics Review Letters* **87**(18), 183,901 (2001).

- [109] M. Lein, N. Hay, R. Velotta, J. P. Marangos, and P. L. Knight, "Role of the Intramolecular Phase in High-Harmonic Generation," *Physics Review Letters* **88**(18), 183,903 (2002).
- [110] M. Y. Shverdin, D. R. Walker, D. D. Yavuz, G. Y. Yin, and S. E. Harris, "Generation of a Single-Cycle Optical Pulse," *Phys. Rev. Lett.* **94**(3), 033,904 (2005).
- [111] A. Sokolov, D. Yavuz, D. Walker, G. Yin, and S. Harris, "Light modulation at molecular frequencies," *Phys Rev A* **63**, art. no.-051,801 (2001).
- [112] C. G. Durfee, L. Misoguti, S. Backus, H. C. Kapteyn, and M. M. Murnane, "Phase matching in cascaded third-order processes," *J Opt Soc Am - B Optical Physics* **19**(4), 822-831 (2002).
- [113] S. Chin, F. Théberge, and W. Liu, "Filamentation nonlinear optics," *Appl. Phys. B* **86**(3), 477-483 (2007).
- [114] N. Kortsalioudakis, M. Tatarakis, N. Vakakis, S. D. Moustazis, M. Franco, B. Prade, A. Mysyrowicz, N. A. Papadogiannis, A. Couairon, and S. Tzortzakis, "Enhanced harmonic conversion efficiency in the self-guided propagation of femtosecond ultraviolet laser pulses in argon," *Appl Phys B-Lasers O* **80**(2), 211-214 (2005).
- [115] U. Hohm, "Dispersion of polarizability anisotropy of H-2, O-2, N2O, CO2, NH3, C2H6, and Cyclo-C3H6 and evaluation of isotropic and anisotropic dispersion-interaction energy coefficients," *Chem. Phys.* **179**(3), 533-541 (1994).
- [116] G. Maroulis and A. J. Thakkar, "Polarizabilities and hyperpolarizabilities of carbon-dioxide," *J. Chem. Phys.* **93**(6), 4164-4171 (1990).
- [117] A. Chrissanthopoulos, U. Hohm, and U. Wachsmuth, "Frequency-dependence of the polarizability anisotropy of CO2 revisited," *Journal of Molecular Structure* **526**, 323-328 (2000).
- [118] L. Berge and S. Skupin, "Sub-2 fs pulses generated by self-channeling in the deep ultraviolet," *Opt. Lett.* **33**(7), 750-752 (2008).
- [119] D. R. Lide, *Handbook of Chemistry and Physics*, 88th ed. (CRC Press, 2007).